SLAC-R-553
UC-414

Properties of Time Profiles of Gamma-Ray Bursts Using Pulse Decomposition Analysis*

Andrew Lee

Stanford Linear Accelerator Center
Stanford University
Stanford, CA 94309

SLAC-Report-553
February 2000

Prepared for the Department of Energy
under contract number DE-AC03-76SF00515

Printed in the United States of America. Available from the National Technical Information Service, U.S. Department of Commerce, 5285 Port Royal Road, Springfield, VA 22161.

---

*Ph.D. thesis, Stanford University, Stanford, CA 94305.

PROPERTIES OF TIME PROFILES OF GAMMA-RAY BURSTS USING PULSE DECOMPOSITION ANALYSIS

A DISSERTATION
SUBMITTED TO THE DEPARTMENT OF PHYSICS
AND THE COMMITTEE ON GRADUATE STUDIES
OF STANFORD UNIVERSITY
IN PARTIAL FULFILLMENT OF THE REQUIREMENTS
FOR THE DEGREE OF
DOCTOR OF PHILOSOPHY

Andrew Lee
February 2000

Abstract

The time profiles of many gamma-ray bursts consist of distinct pulses, which offers the possibility of characterizing the temporal structure of these bursts using a relatively small set of pulse shape parameters. This pulse decomposition analysis has previously been performed on a small sample of bright long bursts using binned data from BATSE, which comes in several data types, and on a sample of short bursts using the BATSE Time-Tagged Event (TTE) data type. I have developed an interactive pulse-fitting program written in IDL using the phenomenological pulse model of Norris, *et al.*, a maximum-likelihood fitting routine, and a semi-automatic routine to determine initial guesses for the fitting routine from time profiles smoothed by a wavelet de-noising algorithm. I have used this program to analyze the Time-to-Spill (TTS) data for all bursts observed by BATSE up through trigger number 2000, in all energy channels for which TTS data is available.

I present statistical information on the attributes of pulses comprising these bursts, including relations between pulse characteristics in different energy channels, and the evolution of pulse characteristics through the course of a burst. I carry out simulations to determine the biases that our procedures may introduce. Among the results are that pulses tend to have shorter rise times than decay times, and tend to be narrower and peak earlier at higher energies. I also examine correlations between brightness measures and timescale measures which may result from cosmological time dilation of bursts, or from intrinsic properties of burst sources or from selection effects. The correlations between these parameters among pulses within individual bursts give a measure of the intrinsic effects while the correlations among bursts could result both from intrinsic and cosmological effects. I find that timescales tend to be shorter in bursts with higher peak fluxes, but tend to be longer in bursts with higher total fluences. I also find that peak fluxes and total fluences of bursts are uncorrelated, indicating that they cannot both be good distance indicators for bursts.

Acknowledgments

I could not have done my thesis work without the assistance of many people. First and foremost, my thesis advisor, Elliott Bloom, has given me a great deal of help and support in many areas. Jeffrey Scargle of the NASA / Ames Research Center has given me invaluable assistance in many areas, including several aspects of gamma-ray bursts, wavelets, and statistical methods. Vahé Petrosian provided a great deal of useful feedback on my thesis, helped with several statistical issues, and contributed greatly to the two papers submitted to the Astrophysical Journal based on the work presented here.

Jay Norris of the NASA / Goddard Space Flight Center first suggested that I examine the BATSE TTS data, was largely responsible for developing the pulse model that I used to analyze gamma-ray burst time profiles, and informed me of many developments in gamma-ray burst observations. Gary Godfrey and Christopher Chaput helped with many questions concerning data analysis techniques. Han Wen taught me many essential aspects of IDL. Nicole Lloyd informed me of a number of relevant theories of gamma-ray burst sources. On the BATSE instrument team, Charles Meegan of the NASA / Marshall Space Flight Center and Robert Preece of the University of Alabama at Huntsville, helped me understand some of the details of the BATSE burst data, without which I would never have been able to find and properly handle the gaps that are present in the data.

Lynn Cominsky of Sonoma State University taught me about many aspects of astrophysics and informed me of several developments in gamma-ray burst observations. William Atwood gave me useful feedback when I was planning my research.

Ray Cowan of MIT helped with almost every aspect of TeX, LaTeX, and Postscript, without which I couldn't have actually written this thesis. Paul Kunz assisted me with using FrameMaker for preparing transparencies for my thesis defense. In the SLAC Technical Publications Department, Sylvia MacBride and Terry Anderson helped me prepare posters

for conferences, and Shirley Boozer helped me prepare a paper for the proceedings of the Third Huntsville Gamma-Ray Burst Symposium.

Daniel Engovatov took over running our research group's computers from me, which gave me more time to work on my thesis. Gayane Shabad learned to create Web pages, which meant that I didn't have to maintain our group's Web pages. Linda Lee Evans and Andy Reid kept everything running in our group, and Andy made all of the arrangements for my thesis defense. Marcia Keating and Dawn Hyde helped me take care of all of the procedures and paperwork that the Physics Department and Stanford University required.

Contents

List of Tables

List of Figures

Chapter 1

Introduction

1.1 General Characteristics and Brief History of Gamma-Ray Bursts

In the early 1960's, the U.S. Air Force began launching the Vela series of satellites to develop technology for monitoring nuclear weapons tests.[1] The satellites carried a variety of radiation detectors, including gamma-ray detectors, and later satellites in the series had improved capabilities. In 1969, the satellites began to detect bursts of gamma-rays that were shown not to be coming from the Sun or the Earth using differences in arrival times from different satellites. These *gamma-ray bursts* (GRBs) coming from space attracted much interest after their discovery was published in 1973. Gamma-ray bursts have since been observed by many space-based instruments, and range in duration from milliseconds to several minutes. The vast majority have been observed at photon energies of tens of keV to above 1 MeV, with some observed at higher gamma-ray energies. Until February 1997, no counterparts had been found for GRBs at lower energies, and the distances to the burst sources could not be measured. Over 100 models have been advanced to explain the origin of GRBs, placing the sources at distances ranging from the vicinity of the solar system to cosmological distances.[2, 3, 4, 5] Transient radio and optical counterparts have since been observed for a number of gamma-ray bursts, allowing redshift measurements that established that these bursts, and probably nearly all other gamma-ray bursts, were produced at cosmological distances. However, the physical mechanisms that produce GRBs are still not known, although a few classes of models are strongly favored.

Individual bursts are commonly identified by a six-digit number giving the date (Universal Time) on which it was detected; for example, a burst observed on February 28, 1997 would be identified as GRB 970228. If multiple bursts are observed on one day, the brightest burst observed that day is identified by the date, and other bursts observed that day are identified by the date with a single-letter suffix appended, “B” for the second brightest burst, “C” for the third brightest, etc. There may also be a prefix identifying the instrument that observed the burst, or the particular burst catalog, *e.g.*, bursts in the fourth BATSE burst catalog, the 4B Catalog, have the prefix “4B” attached to their catalog numbers. It is unclear how bursts will be identified in 2069, when the designations of new bursts will begin to conflict with the first bursts observed by the Vela satellites.

1.2 Isotropic Distribution

It was originally believed that GRBs originated from neutron stars within our galaxy. The *BATSE* instrument on board the Compton Gamma-Ray Observatory (CGRO) found that GRBs are distributed isotropically in the sky, with no correlation between the distribution of bursts and the galactic bulge, the galactic plane, or the Andromeda galaxy M31, and no evidence of any dipole or quadrupole moments, after correcting for BATSE’s nonuniform sky exposure.[6] This eliminated the galactic neutron star hypothesis, and any other models in which GRBs are concentrated in the visible parts of our galaxy. Figure 1.1 shows a map of the first 2000 bursts observed by BATSE, in galactic coordinates using the equal-area Aitoff-Hammer projection.

After this discovery, the remaining possibilities were that bursts are produced in the vicinity of the solar system, such as in the Oort cloud, or in an extended galactic halo, or are at cosmological distances. The models that place bursts in the vicinity of the solar system use mechanisms for producing gamma-rays that are widely considered to be extremely implausible, such as collisions between comets composed of antimatter and normal matter in the Oort cloud.

The extended galactic halo models require that such a halo be large enough so that the Sun’s location away from the center of the galaxy wouldn’t cause any visible anisotropy in the burst distribution, but not so large that we would expect to see an increased concentration in the direction of the Andromeda galaxy coming from its halo. Over time, as the BATSE instrument gathered more data, and improved the statistical significance of the

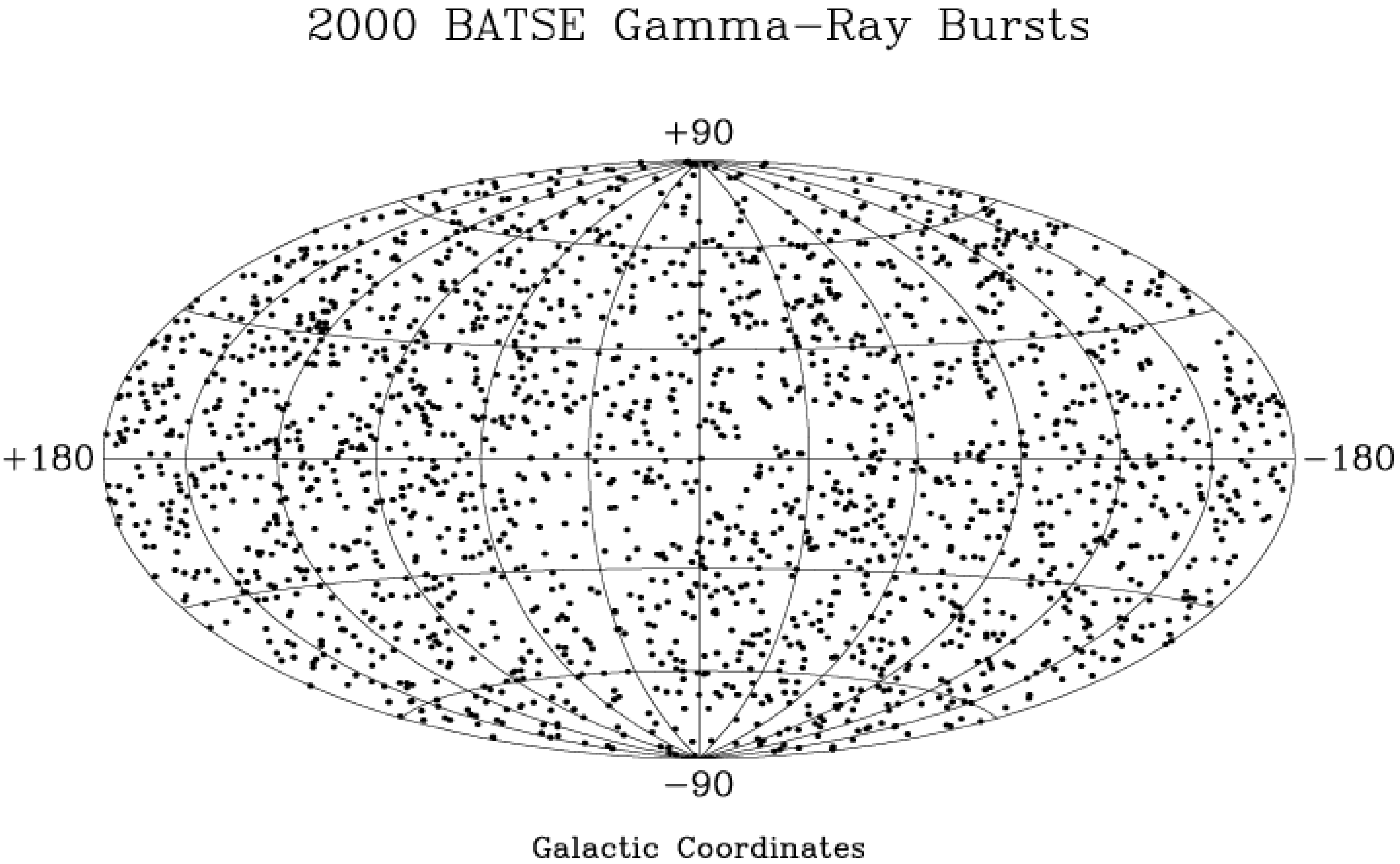

Figure 1.1: Map of gamma-ray bursts observed by BATSE from April 19, 1991 through December 12, 1997, with BATSE trigger numbers 105 through 6531. From `http://cossc.gsfc.nasa.gov/cossc/batse/images/batse2k.gif`.

isotropic distribution of bursts, the minimum possible size for an extended halo increased while the maximum size decreased, greatly constraining such models, although the isotropy measurements alone have not completely excluded these models.

Models in which burst *sources*, sometimes referred to as *bursters*, are located at cosmological distances from the Earth became strongly favored over other models because of the isotropic spatial distribution. Such models typically have sources with luminosities of 10^{51} ergs/second, and produce this through cataclysmic mechanisms such as coalescence of neutron stars or other massive compact objects,[7] because it is difficult for non-cataclysmic mechanisms to yield so much power. The intrinsic luminosities of these sources is lower if the emission is beamed, rather than isotropic. These cataclysmic models don't usually allow for the possibility of a repeating source that produces multiple gamma-ray bursts, since the source is destroyed in the process.

1.3 Repetition

If some bursters repeat on timescales of a few years or less, this might show up as clustering in burst locations. Statistical studies of BATSE burst locations have found no clear evidence of clustering, suggesting that any repeating bursters are rare, or that the repetition timescales are longer than BATSE has been in operation.[8, 9] These searches are limited by the poor angular resolution of BATSE burst locations. Some early studies using two-point correlations of burst locations have found excesses of pairs of bursts with separations near 0° and near 180°.[10, 11] Since it is impossible to produce antipodally related bursts, it is generally believed that both excesses are spurious, and result from some statistical problem. Later studies have found no evidence of significant numbers of repeating bursts.[12, 13]

In October, 1996, BATSE observed four consecutive triggers, 5646–5649, over two days from the same region of the sky.[14] These events may be the first known case of a gamma-ray burst source producing multiple bursts, or may be a single gamma-ray burst with extremely long periods of quiescence. They may also be three separate bursts, one with a long period of quiescence, that happened to occur in the same part of the sky as viewed from the Earth.[15]

1.4 Inhomogeneous Distribution

The distribution of bursts observed by BATSE doesn't appear to be homogeneous; it seems to fall off at large distances. This result assumes that space is Euclidean, and ignores effects due to cosmological evolution and the possible evolution of GRB sources. One way to measure this inhomogeneity is the V/V_{max} test, where V is the volume of the sphere of space whose radius is the distance between the Earth and the burst, and V_{max} is the volume of the sphere whose radius is the maximum distance at which a burst could trigger BATSE.[16] Although neither V nor V_{max} can be known individually without knowing the intrinsic luminosity of a burst, the ratio is simply $V/V_{\text{max}} = (R/R_{\text{max}})^3$, where R and R_{max} are the corresponding radii of the spheres. The distance ratio is usually calculated by using the peak flux of a burst as a measure of its intensity, so that $C_{\text{max}}/C_{\text{min}} = (R/R_{\text{max}})^2$, where C_{max} is the peak count rate observed for a burst, and C_{min} is the threshold for generating a burst trigger, the minimum peak count rate at which the burst could have been detected. If bursts are homogeneously distributed, then $V/V_{\text{max}} = (C_{\text{max}}/C_{\text{min}})^{-3/2}$ would be expected to be uniformly distributed between 0 and 1, with a mean of 0.5.

The BATSE 3B burst catalog data yields the result $\langle V/V_{\text{max}} \rangle = 0.33 \pm 0.01$, and the distribution of $C_{\text{max}}/C_{\text{min}}$ shows a deficit of faint bursts from the 3/2 power law expected for homogeneity.[8] In models that place GRBs near the solar system or in an extended galactic halo, this result would be consistent with observing the outer edges of the burst distribution. In models that place bursts at cosmological distances, this result corresponds to a deficit of bursts at large redshifts, and could be caused by the expansion of the universe, or by the non-existance of burst sources in the early universe.

1.5 Temporal Characteristics

The temporal structure of bursts show a wide range of morphologies, but so far, only one clear division has been found: The durations of bursts observed by BATSE, measured by the length of the intervals in which 90% of the total photon counts arrive (the T_{90} intervals), show a bimodal distribution when histogrammed with logarithmically spaced bins, with peaks around 0.5 and 30 seconds, and a deficit around 2 seconds.[17, 8] (See Figure 1.2.) A similar effect appears with the T_{50} intervals, the intervals in which 50% of the total photon counts arrive. (See Figure 1.3.) No differences between the spatial distributions of the long

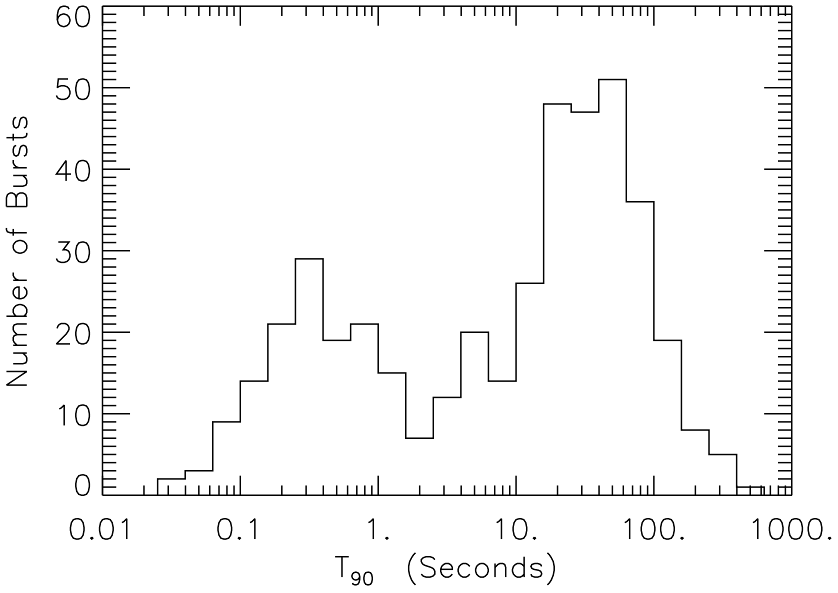

Figure 1.2: The T_{90} distribution of bursts from the BATSE 3B Catalog. From Meegan *et al.* [21], figure available at `http://www.batse.msfc.nasa.gov/publications/abstracts/preprints/meegan/meegan960222_3bfig11b.ps`.

and short bursts have been found.[18] The long bursts appear to be complex bursts where the lengths of the durations largely come from long intervals between major pulses, while the short bursts appear to be simple pulses where the durations contain mainly the shorter pulse widths.[19, 20]

Many burst time profiles appear to be composed of a series of discrete, often overlapping, pulses, often with a *fast rise, exponential decay* (FRED) shape.[22]

The time profile of one burst, BATSE trigger number 1453, contains a sharp spike with sub-millisecond rise and decay times.[23, 24, 25] The time profile of another burst, BATSE trigger number 1577, contains a spike with duration shorter than 1 ms. The data with the finest time resolution, the time-tagged event (TTE) data, end long before the spike occurs, so we are limited by the temporal resolution of the data with the next-finest time resolution, the Time-to-Spill (TTS) data. The portion of the TTS data containing the spike is shown in Figure 1.4. Other bursts that have been observed by BATSE also have temporal structure on millisecond timescales.[26] Large intensity variations on one millisecond timescales must be emitted from regions smaller than about 300 km, in order to satisfy causality.

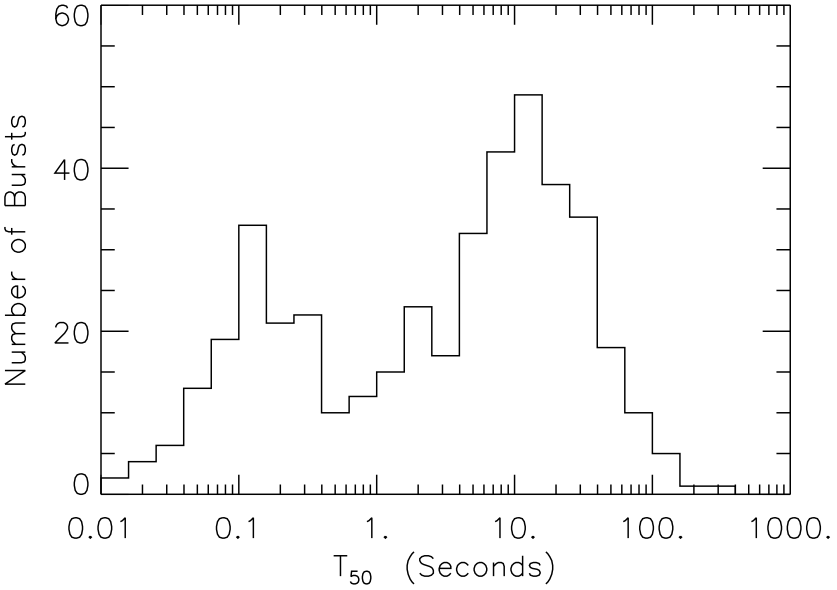

Figure 1.3: The T_{50} distribution of bursts from the BATSE 3B Catalog. From Meegan *et al.* [21], figure available at `http://www.batse.msfc.nasa.gov/publications/abstracts/preprints/meegan/meegan960222_3bfig11a.ps`.

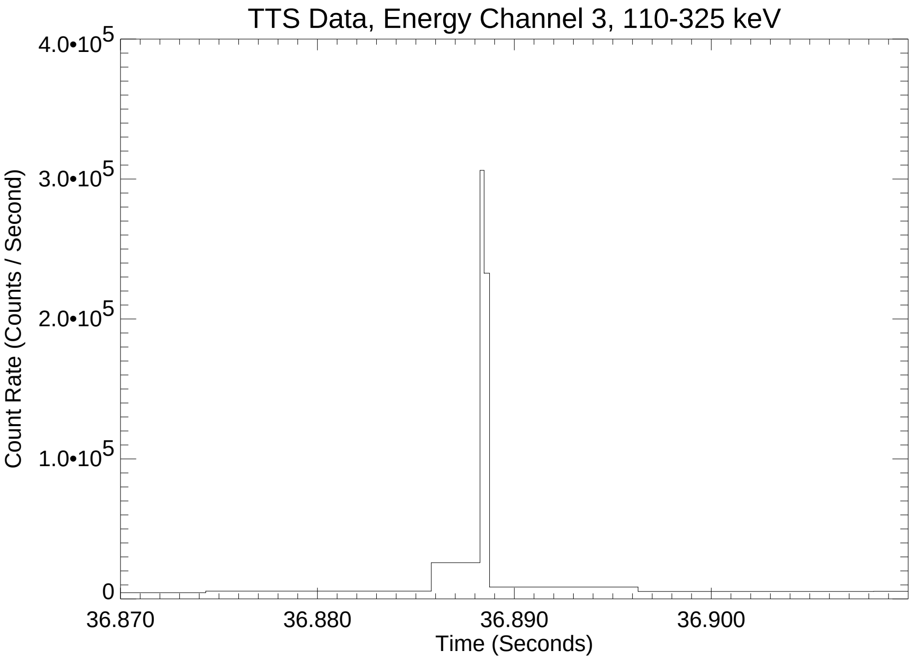

Figure 1.4: BATSE Trigger Number 1577.

1.6 Spectra

The continuum spectra of bursts have been found to be fit well over the range of energies observed by BATSE and similar instruments by the four parameter model

$$N(E) = \begin{cases} AE^{\alpha}e^{-E/E_0}, E \leq E_b, \\ A'E^{\beta}, E \geq E_b, \end{cases} \tag{1.1}$$

where $E_b = (\alpha - \beta)E_0$ and A' is chosen to make the function differentiable at $E = E_b$.[27] The parameters are different between bursts, and vary with time within individual bursts.

Bursts generally show a hard-to-soft spectral evolution, and individual spikes within bursts also frequently show a hard-to-soft spectral evolution.

There have been reports of spectral lines in burst spectra corresponding to cyclotron lines, in burst spectra, but these have not been confirmed.

1.7 Counterparts

It has been widely believed for many years that observations of gamma-ray bursts in other energy ranges would contribute greatly to understanding what produces them. A number of bursts have been observed at energies higher than the BATSE range by various gamma-ray telescopes, including the other instruments on board the Compton Gamma-Ray Observatory: EGRET, which covers an energy range of 20 MeV to 30 GeV, COMPTEL, which is typically used to observe bursts from 750 keV to 30 MeV, and OSSE, which covers 50 keV to 10 MeV. Some bursts have been observed by X-ray telescopes at energies of a few keV. Figure 1.5 shows observations of GRB 940217 (BATSE trigger number 2831) by BATSE, EGRET, and *Ulysses*, an interplanetary probe carrying a small gamma-ray burst monitor.[28] EGRET observed an 18 GeV photon from this burst 90 minutes after the BATSE trigger.

There are now several efforts underway to observe bursts detected by BATSE at optical and radio wavelengths. The BATSE Coordinate Distribution Network (BACODINE) was created to send the locations of bursts observed by BATSE to these groups as quickly as possible after the bursts are detected, since it wasn't known when transient events at other wavelengths would begin relative to the BATSE detection, or how long they would persist, if they existed at all.[29] One difficulty with such efforts are that the error boxes associated

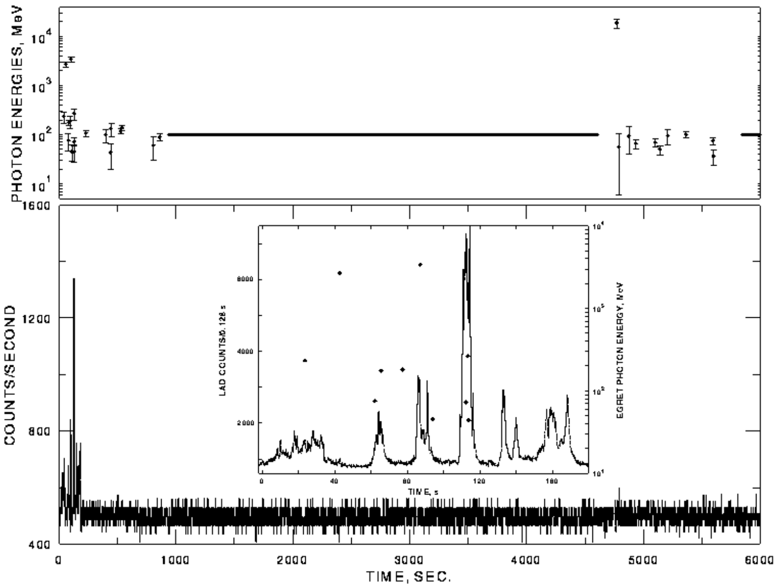

Figure 1.5: Observations of GRB 940217 by BATSE, EGRET, and *Ulysses.* From Hurley *et al.* [28], figure available at `http://cossc.gsfc.nasa.gov/cossc/images/all/burst1.gif`.

with BATSE burst locations are very much larger than the field of view of most other instruments. To date, there has been no conclusive evidence for observations at energies lower than X-rays of bursts for which only BATSE locations are known. BACODINE has been replaced by the GRB Coordinates Network (GCN), which distributes burst locations from a number of other instruments, in addition to BATSE.[30]

Recently, optical counterparts have been discovered for some gamma-ray bursts. The BeppoSAX satellite has observed several gamma-ray bursts since it began observations on June 24, 1996, and it has determined their positions to within a few arcminutes using its Wide Field Camera, which detects X-rays of 2–30 keV. Other instruments on board BeppoSAX have observed fading X-ray afterglows for a number of these bursts. For one of these bursts, GRB 970228, an optical counterpart was observed and appears to be associated with a faint galaxy.[31] Optical [32] and radio [33, 34] counterparts were observed for another burst, GRB 970508. The optical counterpart showed absorption lines corresponding to a redshift of $z = 0.835$, implying that the source of the burst is at least that distant, and the absence of Lyman-α absorption features imply that the source is at $z < 2.3$.[35]

Another burst, GRB 971214, has been identified with an optical galaxy at a redshift of $z = 3.4$.[36, 37, 38] This burst was also observed by BATSE, and the total energy fluence detected by BATSE requires a total gamma-ray energy output in excess of 10^{53} ergs if the emission was isotropic. It is difficult for non-cataclysmic models, and many cataclysmic models, to produce this much energy in such a short time.

GRB 980425 has been identified with SN 1998bw, a type Ib or Ic supernova observed at optical [39] and radio [40] wavelengths which appears to lie in a galaxy at a redshift of $z = 0.0083$. This requires the burst to be far less energetic, with a total gamma-ray energy output below 10^{48} ergs, than the bursts observed by BeppoSAX at much larger redshifts. The association with a supernova favors “hypernova” models for the mechanism producing this particular burst.[41] Since the vast majority of gamma-ray bursts are not associated with supernovae, this suggests that GRB 980425 is a representative of a small class of supernova-GRBs, or S-GRBs.[42] However, a study of gamma-ray bursts with similar temporal and spectral properties at gamma-ray energies to GRB 980425 found no concentration near the Supergalactic Plane, where the type Ib and Ic supernovae are known to concentrate, suggesting that if there is a class of S-GRBs, they may not be distinguishable from other GRBs using gamma-ray observations.[43]

It is quite possible that gamma-ray bursts produce other forms of radiation in addition to electromagnetic. A number of ground-based experiments have looked for excess neutrinos, antineutrinos, and muons above normal background levels that are coincident with observed bursts, but have failed to find any. These could be produced by the bursters, or by interactions in the atmosphere or in the case of muons, by neutrinos interacting with the Earth.[44] The cataclysmic models involving coalescing compact objects would also be strong sources of gravitational radiation, and these are exactly the kind of phenomena that upcoming gravity wave detectors such as LIGO and VIRGO are designed to detect.

1.8 Soft Gamma-Ray Repeaters

Soft gamma-ray repeaters are a small class of objects that were originally included with the *classical* gamma-ray bursts, but which have since been found to have distinct properties that distinguish them from the classical GRBs. There are now four known soft gamma-ray repeaters, designated as SGR 0526-22, SGR 1900+14, SGR 1806-20 and SGR 1627-41, and another possible soft gamma-ray repeater, SGR 1815-13. The bursts that they produce have a soft spectrum with photon energies only in the tens of keV, similar to thermal bremsstrahlung with temperatures of around 30 keV, and have short durations, averaging ~ 0.1 s, sometimes as short as 5 ms. As their name suggests, the three sources have produced multiple bursts. SGR 0526-22 has an eight second periodicity, and SGR 1806-20, which has produced over 100 bursts since August 1978, has a 7.5 second periodicity. SGR 0256-22 has been identified with the supernova remnant N49 in the Large Magellanic Cloud, and SGR 1806-20 has been identified with the supernova remnant G10.0-0.3 and with the X-ray source AX1805.7-2025 on the basis of simultaneous bursts seen in gamma-rays by BATSE, and in hard X-rays seen by the Japanese ASCA satellite. SGR 1627-41 was discovered by BATSE in June, 1998, and has been identified with the supernova remnant G337.0-0.1. The possible soft gamma-ray repeater SGR 1815-13 was discovered by BATSE in June, 1997. It is conceivable that there could be yet another class of gamma-ray bursts with distinct properties that could be produced by a different mechanism from other bursts, or have different spatial distributions from other bursts. If such a class of bursts was produced within the galaxy, it would have to be a small class so that the total distribution of bursts could fit the observed isotropy.

Chapter 2

The BATSE Instrument

2.1 Instrument Description

The Burst and Transient Source Experiment (BATSE) is one of four instruments on board the Compton Gamma-Ray Observatory (CGRO), and is one of the most important sources of gamma-ray burst data. It is an all-sky monitor designed primarily to observe transient gamma-ray sources in the 20–600 keV energy range, including gamma-ray bursts (GRBs), soft gamma-ray repeaters (SGRs), solar flares, and terrestrial gamma-ray flashes (TGFs). BATSE consists of eight detector modules mounted at the corners of the CGRO spacecraft, with each module consisting of a pair of NaI(Tl) crystal scintillation detectors, a *large-area detector* (LAD) and a *spectroscopy detector* (SD). Figure 2.1 shows the CGRO, and Figure 2.2 shows a single BATSE detector module.

The LADs are circular discs, each 50.8 cm in diameter (2025 cm^2 in area) and 1.27 cm thick, facing outward parallel to the faces of a hypothetical regular octahedron. Since the thickness of a LAD is so small compared to its diameter, the cross section of each LAD for an incoming gamma-ray is approximately proportional to the cosine of the angle between the direction of the photon and the normal line to the plane of the LAD, making the angular response curve of each LAD roughly a cosine function. A plastic scintillation detector is mounted in front of each LAD to detect charged particles, which can be used in anticoincidence or coincidence to eliminate or detect only charged particle events. [45] Each LAD has a light collector housing bringing the scintillation photons to three photomultiplier tubes (PMTs), whose signals are summed in the detector, and each light collector housing

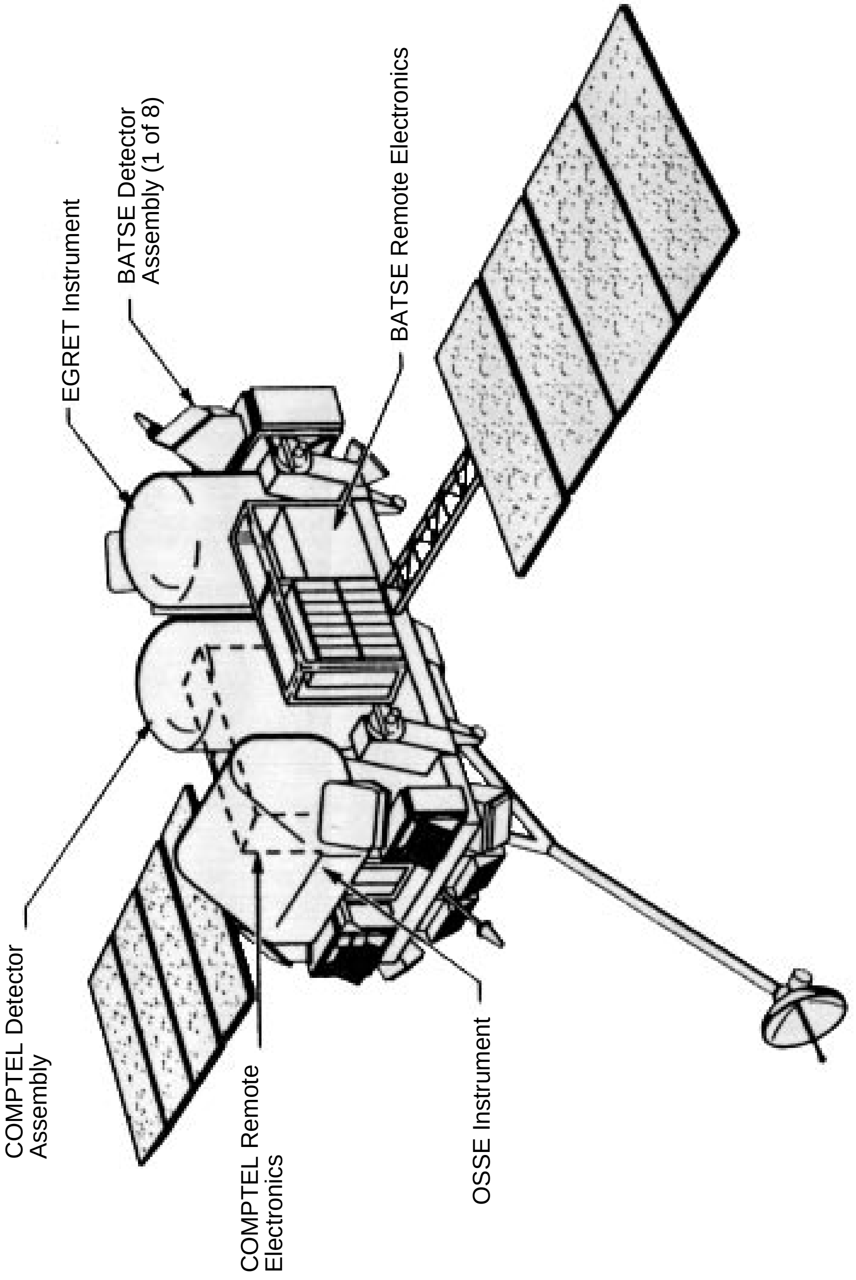

Figure 2.1: The Compton Gamma-Ray Observatory. From `http://www.batse.msfc.nasa.gov/batse/instrument/cgro.ps.gz`.

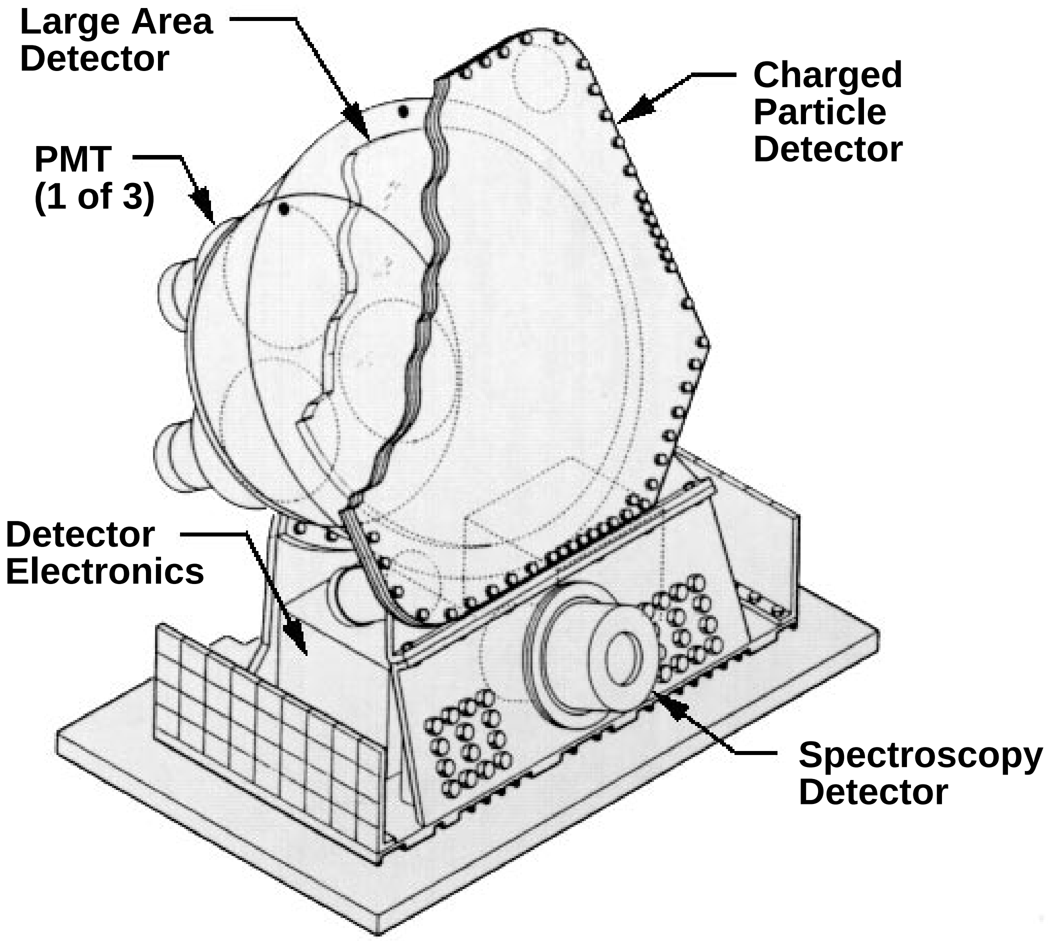

Figure 2.2: A single BATSE detector module. From `http://www.batse.msfc.nasa.gov/batse/instrument/module.ps.gz`.

has a thin lead and tin shield to reduce the rate of gamma-rays entering the LAD from the back side. Each photon event is sent to a fast four-channel discriminator and a slower 128 channel pulse height analyzer. The discriminators operate only in anticoincidence mode to detect only gamma-rays. The four discriminator energy channels are roughly 20–60 keV, 60–110 keV, 110–325 keV, and >325 keV, and the discriminators have a 130 ns dead time. The pulse height analyzers have energy resolution ranging from 5 keV at lower energies to 40 keV at higher energies, and they have a dead time that increases linearly with photon energy, ranging from 3.75 to 27.75 μs. The 128 channels are also summed according to a programmable look-up table to produce sixteen channel data.

The SDs are circular discs, 12.7 cm in diameter (127 cm^2 in area) and 7.62 cm thick, and do not have any strong directional sensitivity. They have no anticoincidence shields, allowing detection of gamma-rays with energies as low as 15 keV. Each SD has a directly coupled PMT attached, and each PMT has a lead and tin shield on its housing. Each photon event is sent to a fast four channel discriminator and a slower 256 channel pulse height analyzer. The four discriminator energy channels are roughly >7 keV, >14 keV, >20 MeV, and >40 MeV, and the discriminators have a 130 ns dead time. The pulse height analyzers have energy resolution ranging from 4 keV at lower energies to 128 keV at higher energies, and they have a dead time that increases linearly with photon energy, ranging from 3.5 to 175.5 μs.

2.2 Data Collection and Transient Event Triggering

The BATSE data types are described in detail in Appendix A. A few data types, with various combinations of time and energy resolution, are collected at all times. Background rates are fit at regular time intervals, now set to 17.4 seconds, for each detector in each discriminator energy channel. When a transient event is detected, according to programmable triggering criteria, BATSE enters a special data collection and telemetry mode and stores several more data types, with higher time or energy resolution, for a fixed accumulation period that was originally 242 seconds, but was changed to 573 seconds on December 17, 1992, primarily for observing solar flares. Discriminator counts are continuously binned at three timescales, 64, 256, and 1024 ms. A transient event trigger is generated when the count rate rises above a threshold defined relative to the background in at least two LADs on the same timescale, in the sum of a fixed combination of discriminator energy channels.

This threshold is nominally 5.5 standard deviations above the background at any of the three timescales in discriminator energy channels 2 and 3 combined. However, the number of standard deviations above threshold can vary by timescale, or triggering can ignore any of the three timescales, and triggering can also depend on the sum of any possible combination of discriminator energy channels. These parameters have been changed several times during the mission to selectively monitor different kinds of transient events, although the energy channels used for the trigger were 2 and 3 through the end of the period covered by the BATSE 3B catalog, which is described later in this chapter. All triggered events are consecutively numbered, regardless of their source, and these *trigger numbers* are commonly used to refer to specific GRBs observed by BATSE, instead of the date-based catalog numbers. Transient event triggers are also sent to the other instruments on board the CGRO.

During the accumulation period, further triggers are disabled. After the data accumulation period for a transient event has ended, the data is then transmitted, which takes from 80 minutes for weak bursts to 105 minutes for strong bursts. During this period, the trigger thresholds on the 64 ms timescale are set to the peak count rates observed in the transient event, and triggers on the 256 ms and 1024 ms timescales are disabled, so only transient events with higher count rates on the 64 ms timescale can generate a new trigger. If this happens, the untransmitted data from the first transient event is overwritten and lost, though LAD discriminator counts binned to 64 ms (the DISCSC data type) is always transmitted.

The detectors where the count rates exceed threshold at the trigger time are the *burst selected* or *on-burst* detectors. If the count rates exceed threshold in more than four detectors, then the four detectors with the highest count rates are the burst selected detectors. The transient event data types store data only for these detectors, or for the four detectors with the highest count rates, whether they exceeded threshold or not. There are also ring buffers that continuously store until a trigger is generated, so that they contain data from before the trigger when read out.

BATSE can also observe non-transient gamma-ray sources using earth occultation, and can perform on-board time-folding of 16-channel SD data for pulsar observations. This 16-channel SD data is generated by compressing 256-channel SD counts in the same way that 128-channel LAD counts are compressed to produce the 16-channel MER data.

2.3 Transient Event Locations and Classification

The locations of transient events are calculated using the relative count rates above background in the different LADs, and the directional response of the LADs. The BATSE flight software calculates whether a trigger comes from the direction of the sun using only ratios of counts in different LADs, in order to send a solar flare indication to OSSE, another instrument on board the CGRO. Aside from this, initial positions are determined on the ground from the rates in the three LADs with the highest count rates, and improved using count rates from the four or six LADs with the highest count rates, after correcting for atmospheric scattering. [46] Background rates are determined by fitting linear or quadratic curves to a long interval. The directional response varies with photon energy, and it extends beyond 90 degrees, because some gamma-rays do enter the LADs from behind.

Transient events are initially classified on the ground based on their locations and their spectral characteristics. Events coming from the sun are solar flares; those coming from the earth are TGFs, and the rest are GRBs, SGRs, or other sources outside the solar system. For GRBs, final locations are calculated using only discriminator channels 2 and 3, which cover 60 to 325 keV, because bursts produce the highest count rates in those channels, giving a better signal to background ratio.

Some GRBs are also observed by the Compton Telescope (COMPTEL), another instrument aboard the CGRO, which can determine locations more precisely. A few bright bursts are observed by small gamma-ray detectors aboard interplanetary probes, which together with BATSE comprise the Interplanetary Network (IPN). Locations of bursts observed by the IPN can be calculated very precisely by triangulation from the times at which each spacecraft observes the burst.

The chi-squared minimization routine used to calculate event locations also gives the statistical error on these locations. The RMS systematic errors have been estimated to be less than 2 degrees, by comparing BATSE locations with those located by COMPTEL or the IPN.

2.4 Mission History and Gamma-Ray Burst Catalogs

The CGRO was placed in orbit by the Space Shuttle on April 5, 1991, and BATSE transient event triggering was enabled on April 19, 1991. It was originally expected that BATSE

Table 2.1: BATSE Gamma-Ray Burst Catalogs

Catalog	Ending Date	Last Trigger No.	Total Bursts	New Bursts
1B	3/5/92	1466	260	260
2B	3/9/93	2230	585	323
3B	9/19/94	3174	1122	536
4B	8/29/96	5586	1636	514

would show that gamma-ray bursts are concentrated in the plane of the galaxy, supporting the prevalent expectation that they originated from galactic neutron stars. It soon showed instead that gamma-ray bursts are nearly isotropically distributed in the sky, excluding models where bursts are produced in the visible part of the galaxy. BATSE also discovered the soft gamma-ray repeater SGR 1627-41, the possible soft gamma-ray repeater SGR 1815-13, as well as terrestrial gamma-ray flashes, which appear to come from high-altitude lightning in the earth's atmosphere.

The tape recorders on the CGRO began developing problems after March 1992, and eventually, they completely failed, requiring that data be transmitted directly from the BATSE memory. This resulted in many data gaps, either from losses from the tapes, or later from telemetry gaps when burst readouts were transmitted directly from the BATSE memory. On December 17, 1992, the accumulation time for triggered events was increased from 242 to 573 seconds, and the flight software was modified to suspend transmission during telemetry gaps. The readout time was also changed from a fixed 90 minutes per trigger to a variable length so that BATSE could return to normal triggering sooner after weak events. These and other changes to the CGRO and BATSE flight software significantly reduced the amount of data lost after March, 1993.

The first GRB observed by BATSE was trigger number 105, on April 21, 1991. Four catalogs of gamma-ray bursts observed by BATSE have been released, (see Table 2.1) each one cumulative, beginning with trigger number 105. The first catalog released was the 1B catalog [47] and the second was the 2B catalog, with some triggers reclassified.[48] The 3B catalog had improved locations for the bursts from the 2B catalog and one trigger reclassified from the 2B catalog.[21, 8] The 4B catalog is the latest catalog released, and has some burst positions improved from the 3B catalog, but no triggers reclassified.[49]

Each catalog contains five tables of summary information about the bursts derived from the LAD data, all indexed by BATSE trigger number. The Basic Information Table contains the trigger number, trigger date and time, a BATSE catalog name derived from the trigger date, the calculated position, the angle between the burst direction and the geocenter (center of the earth) as seen by BATSE, and whether the burst was overwritten by a brighter triggering event, or overwrote the previous triggering event. The Comments Table contains the trigger number and free-form comments about the burst. The $C_{\mathrm{Max}}/C_{\mathrm{Min}}$ table contains the trigger number, the trigger thresholds on each of the three triggering timescales (C_{Min}), and the maximum count rate in the second most brightly lit detector at each timescale divided by the trigger threshold at that timescale ($C_{\mathrm{Max}}/C_{\mathrm{Min}}$), i.e., the factor by which the count rate exceeded the triggering criteria. The Duration Table contains the trigger number, the length of the time intervals during which the middle 50% and 90% of the counts recorded for each burst were recorded (T_{50} and T_{90}, respectively), the uncertainties in T_{50} and T_{90}, and the start time of the T_{50} and T_{90} intervals relative to the burst trigger, i.e., the times when 25% and 5% of the counts had been recorded for each burst, respectively. The Flux Table contains the trigger number, the peak fluxes on the 64, 256, and 1024 ms timescales in discriminator energy channels 2 and 3 and measured in photons/cm^2/sec, and the total energy fluences, or energy deposited, in each discriminator energy channel during the entire span of the burst, measured in ergs/cm^2. The peak fluxes and fluences are calculated using the count rates, as well as the detector response matrices, which give the detector efficiencies in terms of energy, detector orientation relative to the source and to the geocenter, etc., so they are described in terms of *photons* rather than *counts*, which is used to refer to the actual, unadjusted number of counts recorded by the detectors. Only the Basic Information Table contains information about all of the bursts in the catalog, because overwrites and telemetry gaps make it impossible to calculate the information in the other tables for some bursts. Table 2.2 gives the number of bursts in each of the tables in all of the BATSE burst catalogs that have been released.

The 2B and 4B Catalogs also contains tables of trigger efficiencies as a function of peak flux, and tables of the sky exposure of BATSE as a function of burst declination. BATSE's sky exposure is not uniform due to earth occultation, the orbit of the CGRO, and outages when passing through the South Atlantic Anomaly. The 4B catalog also contains a table of all of the changes to the trigger criteria that have been made since the start of the mission,

Table 2.2: Sizes of Tables in the BATSE Burst Catalogs

Table	2B	3B	4B
Basic Information	585	1122	1636
$C_{\mathrm{Max}}/C_{\mathrm{Min}}$	411	657	912
Duration	433	834	1234
Flux	459	867	1292

the dates and times of these changes, and the first trigger number after each change. Several months before the release of the 4B catalog, a preliminary catalog of all bursts observed by BATSE to date was first made available on the World-Wide Web. This preliminary catalog contains all of the data tables, but not the Comments table, with the Basic Table and the Flux Table are updated every 1-2 weeks, and the other tables updated less frequently. As of September 1998, BATSE has observed over 2200 gamma-ray bursts.

The summary information given in these tables has been the basis of many studies of gamma-ray burst properties. However, they contain very little information about the temporal or spectral characteristics of bursts, so it is necessary to use the actual data collected by BATSE to study these. The various BATSE data types and their file formats are described in Appendix A. The data used in this investigation are the Time-to-Spill (TTS) data.

2.5 The BATSE Time-to-Spill Data

The BATSE Time-to-Spill (TTS) burst data record the time intervals to accumulate a fixed number of counts, usually 64, in each of four energy channels. These time intervals give the reciprocals of the average count rates during the spill intervals, whose times can be easily calculated. There has been almost no analysis done using the TTS data because it is less convenient to use with standard algorithms than the time-tagged event (TTE) data or the various forms of binned data. The TTS data use the limited memory on board the CGRO more efficiently than do the binned data types because at lower count rates, it stores spills less frequently, with each spill having the same constant fractional statistical error. On the other hand, the binned data types always store binned counts at the same intervals,

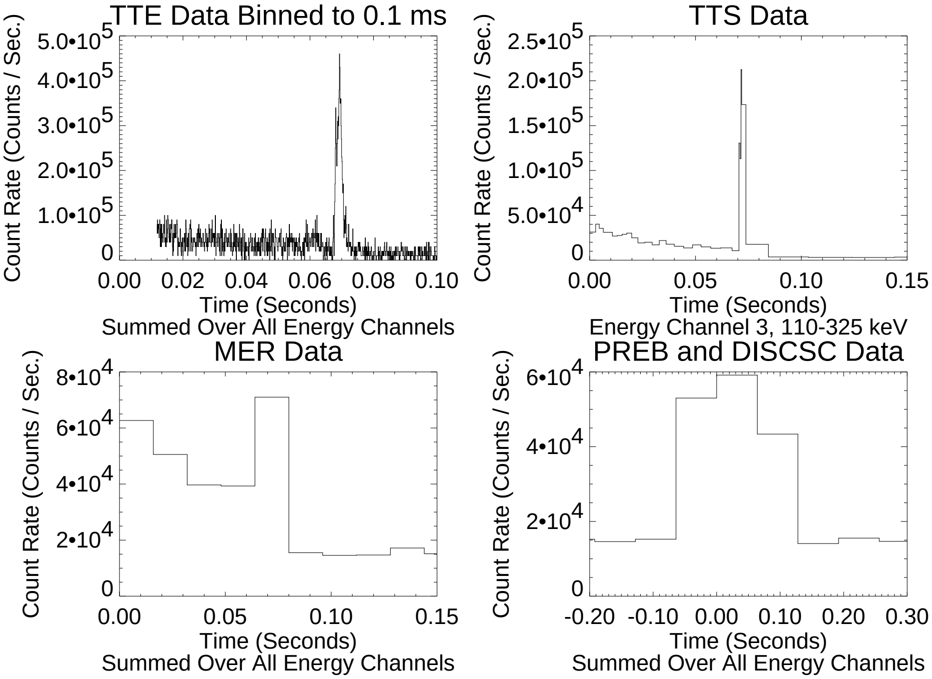

Figure 2.3: BATSE Trigger Number 1453.

so that at low count rates the binned counts have a large fractional statistical error. The variable time resolution of the TTS data ranges from under 50 ms at low background rates to under 0.1 ms in the peaks of the brightest bursts. In contrast, the finest time resolution available for binned data is 16 ms for the medium energy resolution (MER) data, and then only for the first 33 seconds after the burst trigger. The TTS data can store up to 16,384 spill events (over 10^6 counts) for each energy channel, and this is almost always sufficient to record the complete time profiles of bright, long bursts. This is unlike the TTE data, which are limited to 32,768 counts in all four energy channels combined. For short bursts, the TTE data has the advantages of finer time resolution than the TTS data, with arrival times of individual counts given with 2 μs resolution, and of containing data from before the burst trigger time. Furthermore, some of the shortest bursts are nearly over by the time burst trigger conditions have been met, so the TTS and MER data aren't very useful for these bursts.

Figure 2.3 illustrates the possible benefits of the finer time resolution of the TTE and TTS data types. It shows the portions of the data that exhibit activity for BATSE trigger number 1453, a short burst with a very sharp spike about 0.07 seconds after the burst trigger.

This spike is one of the shortest timescale features that has been identified in any burst observed by BATSE.[23, 24, 25, 50] The TTE data have been binned in 100 microsecond bins for plotting, and the spike clearly shows structure. Unfortunately, for this burst, the TTE data have two data gaps after the burst trigger, and the spike occurs between these two data gaps, so it isn't possible to determine the time when the spike occurs. The actual time is later than the time labeled on the axis by a fixed, but unknown offset (the length of the first data gap), and only data after the first data gap is shown. The TTS data have good time resolution during the spike, and also shows some of its structure. Only energy channel 3 is shown since the different energy channels cannot be combined because the spill times don't coincide for different energy channels. The binned data types use equal time bins which begin and end at the same times in all energy channels, so they can be summed over all energy channels, and the TTE data are normally plotted after being binned in equal time bins, so they can also be summed over energy channels. The 16 ms binning of the MER data is too coarse to show any structure in the spike, and is longer than the duration of the spike, so that the height of the spike shown is far lower than the peak count rate. The MER data also uses counts from the pulse-height analyzer, which has finer energy resolution but longer dead time than the discriminator, so it loses more counts due to dead time than the other data types shown here. The combined PREB and DISCSC data contain data from before the burst trigger, as do the TTE data, but the time resolution is poorer than for the MER data. The 64 ms bins used in the PREB and DISCSC data are almost as long as the time between the burst trigger and the peak of the spike.

Figure 2.4 shows an example of the longer time coverage of the TTS and the binned data. It shows all of the data for BATSE trigger number 1288, a long and complex burst. The TTE data have been binned in 5 ms bins for plotting, and end less than 2.3 seconds after the burst trigger, too soon to show any significant structure in the time profile. The TTS contain the complete time profile of the burst after the burst trigger. The MER data end 166 seconds after the burst trigger, and we can see from the TTS data that there is some activity that occurs after the end of the MER data. The transition from 64 ms to 16 ms binning at 33 seconds after the burst trigger is also visible in the MER data. The combined PREB and DISCSC data also contain the complete time profile of the burst after the burst trigger, as well as the 2 seconds before the burst trigger. The differences in time resolution between the TTS, MER, and PREB/DISCSC data don't appear to be important

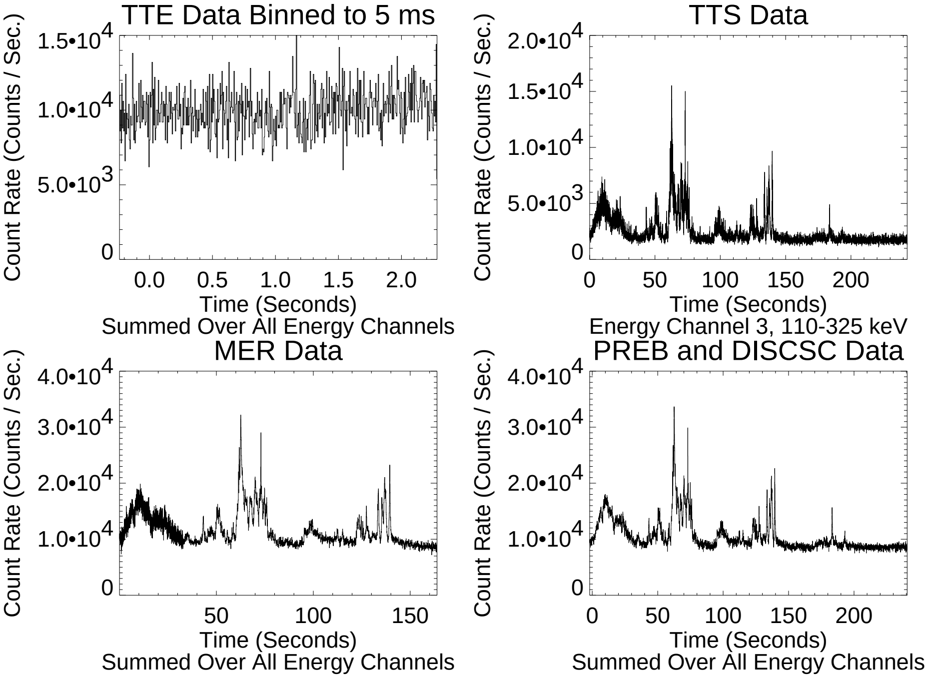

Figure 2.4: BATSE Trigger Number 1288.

for this burst, because most of the temporal variation is on longer timescales.

Figure 2.5 shows an example of a burst where the fine time resolution of the TTE and TTS data is useful, and where the pre-trigger coverage of the TTE data and of the combined PREB and DISCSC data is also useful. It shows all of the TTE data for BATSE trigger number 551, a short burst, and the other data types for the same times that the TTE data covers. The TTE data have been binned in 1 ms bins for plotting, and covers the entire burst. The TTS data have good time resolution, showing the small spike near 0.05 seconds after the burst trigger, but doesn't contain pre-trigger data, including the large spike before the burst trigger. The MER data also contain only post-trigger data and also has noticeably poorer time resolution; the small spike near 0.05 seconds is not visible using this data. The combined PREB and DISCSC data have even poorer time resolution than the MER data, but does contain pre-trigger data. It actually extends to 2.048 seconds before the burst trigger, but this burst shows no activity above background before the start of the TTE data.

The individual event times in the TTE data and the binned counts in the various binned data types follow the familiar exponential and the Poisson distributions, respectively. The

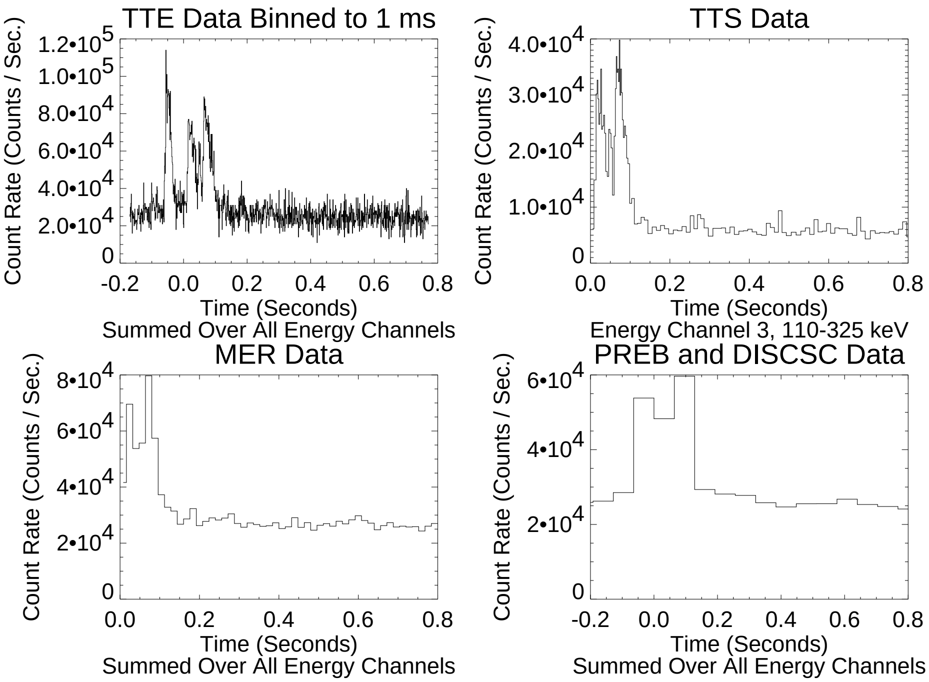

Figure 2.5: BATSE Trigger Number 551.

spill times recorded in the TTS data follow the *gamma distribution*, which is the distribution of times needed to accumulate a fixed number of independent (Poisson) events occurring at a given rate. The probability of observing a spill time t is

$$P(t) \; = \; \frac{t^{N-1} R^N e^{-Rt}}{\Gamma(N)} \; , \tag{2.1}$$

where N is the number of events per spill and R is the rate of individual events. This probability distribution is closely related to the Poisson distribution, which gives the number of events occurring within fixed time intervals for the same process of independent individual events, such as photon arrivals.

Figure 2.6 shows gamma distributions for 16 and 64 events per spill, as well as Gaussian (normal) distributions with the same mean and standard deviation. The TTS data normally collects counts of 64 counts per spill, though 16 and 256 counts per spill are also allowed by the BATSE flight software. The gamma distribution for 256 events per spill is visually indistinguishable from a normal distribution. The mean spill time $\bar{t}$ is simply $\bar{t} = N/R$, the number of events per spill multiplied by the mean time between individual events. The standard deviation of this distribution is $\sigma_t = \bar{t}/\sqrt{N} = \sqrt{N}/R$. Thus, if we have a sequence

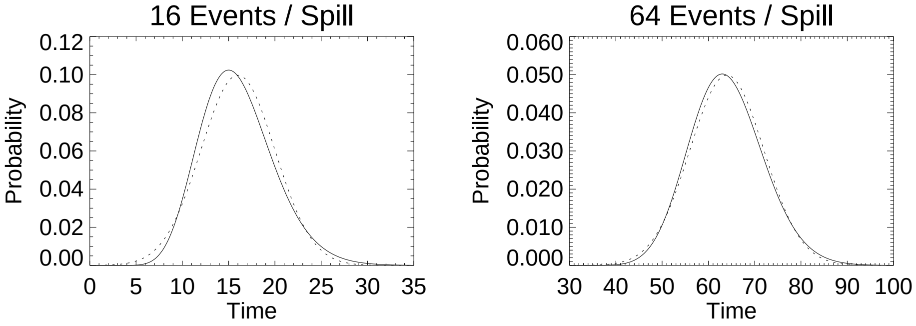

Figure 2.6: Gamma (solid line) and Gaussian (dashed line) distributions.

of spill times t_i with N events per spill, the statistical uncertainty associated with each spill interval t_i is $t_i/\sqrt{N}$, a constant *fractional* error of $1/\sqrt{N}$ times each spill time. Note that the logarithms of the spill times, $\log t_i$, will have a constant statistical uncertainty of $\simeq 1/\sqrt{N}$. In contrast, while data binned with equal time intervals may have finer time resolution at low count rates, the associated statistical uncertainties will be large compared to the count rates, making the finer time resolution less useful.

The gamma distribution is asymmetric, with $P(t) = 0$ for $t \leq 0$, *i.e.*, all spill times must be positive, and a peak at $t_{\max} = (N-1)/R < \bar{t}$. For large N, the gamma distribution approaches a normal (Gaussian) distribution with the same mean and standard deviation, while for $N = 1$, it is just the exponential distribution for individual time-tagged events.

It is useful to interpret the spill times that comprise the TTS data in terms of more commonly used physical quantities, such as count rates. This is straightforward, since the spill time t is given in terms of the average count rate R during the spill interval and the number of counts per spill N by $t = \frac{N}{R}$. It is also straightforward to calculate when the spill occurred relative to the burst trigger from the spill times that these spills correspond to. We then have count rates for a continuous sequence of time intervals of varying durations. The constant relative statistical errors of the spill times then become constant relative statistical errors of the count rates in the corresponding time intervals. However, with the BATSE TTS data, the calculated time intervals still contain the variable discretization error resulting from the spill time encoding.

The time resolution of the BATSE TTS data at a count rate R is simply the length of a spill interval at that count rate. The TTS data have finer time resolution than the PREB and DISCSC data when the count rate is above 1000 counts/second, and has finer time resolution than the MER data when the count rate is above 4000 counts/second.

The TTS data have several characteristics that make it difficult to analyze using many common mathematical and statistical methods. The spills cannot be easily binned into equal time intervals, so that FFT, time-domain wavelet transforms, and other algorithms that require equal time intervals cannot be used. One simple method for binning TTS data into equal time intervals is to place all of the counts represented by a spill into the time bin at the end of the spill interval. FFT power spectra tend to show too much power at short timescales when this method is used. Another method is to distribute the counts uniformly in time into the time bins that overlap with the spill interval. FFT power spectra tend to show too little power at short timescales when this method is used. The periodogram for unevenly sampled data developed by Scargle [51] and Lomb [52, 53] can be applied directly to TTS data, without binning it into equal time intervals, but the resulting power spectra tend to show spurious oscillations in frequency space. It is also impossible to sum count rates from different energy channels, since the spill times don't coincide between energy channels.

Another procedure that cannot be directly applied to TTS data is the algorithm used by Norris *et al.* [54] to equalize signal-to-noise ratios between different bursts. This algorithm involves reducing the "signal" portion of bursts with high signal-to-noise, and increasing their background levels. Since the spills in the TTS data represent a fixed number of counts, applying this procedure would change the beginning and end of the spill intervals themselves, which cannot be done without knowledge of the arrival times of the individual counts.

It is also more complicated to generate simulated TTS data than to generate simulated binned data with equal time bins. When generating simulated TTS data that has a given underlying time profile, it is necessary to generate all of the individual counts in order to determine the spill intervals. When generating simulated binned data with equal time bins, the time intervals are predetermined, so the counts in the individual bins can be generated as Poisson deviates from the underlying time profile.

Chapter 3

The Pulse Model and Pulse Fitting

3.1 The Pulse Model

Gamma-ray burst time profiles, like any other counting data from photon or other particle events, are composed of large numbers of data points, whether binned counts, individual event times, or spill times, that mostly describe random noise arising from Poisson statistics. The underlying physical process generally produces photons at rates that vary only on timescales much longer than the resolution limit of the data. Even if this is not the case, and there is actual power on shorter timescales, it will be obscured by the Poisson noise. For this reason, it is useful to be able to describe time profiles in terms of relatively smooth functions that can be characterized by a small number of parameters (compared to the number of data points). When the sources being observed produce events at constant or very-slowly varying rates, or at rates that vary periodically, the methods for doing this are well understood.

This is not the case for gamma-ray bursts. Burst time profiles vary widely in their characteristics, so much that there is a saying that, "If you've seen one burst, you've seen *one* burst." Some exhibit count rates that rise to a maximum and decay away, while others rise and fall many times. One approach to analyzing burst time profiles is to decompose them into sums of a small number of functions that can be characterized by a few parameters. For example, applying a wavelet denoising procedure to the time profile will describe it as the sum of a small number of wavelets, each of which is characterized by a few wavelet coefficients, and a residual that should be largely statistical noise.[55] Unfortunately, the wavelet coefficients don't correspond to physical quantities that can be compared with models.

Instead of a using a generic basis of complete, orthogonal functions such as a family of wavelets, it may be useful to use functions with parameters that have a clear physical interpretation. Since these functions don't form a complete, orthogonal basis, the decomposition isn't guaranteed to be unique, nor does such a decomposition have to exist. On the other hand, since burst time profiles necessarily contain statistical noise that is generally uninteresting, we don't need to completely decompose them into the sum of these functions; we just need to decompose them into the sum of these functions plus a residual that contains the noise.

To explain the observed time profiles, it seems likely that the mechanism that produces bursts causes gamma-ray emission in discrete pulses, which could, for example, come from different spatial volumes in or near the burst source. Therefore, it may be useful to decompose burst time profiles in terms of individual pulses, each of which rises from background to a maximum and then decays back to background levels. The pulse parameters should include the times at which the pulses occur, the amplitudes of the pulses, and their rise and decay times measured in some way, as well as parameters that further characterize the shapes of the pulses. This gives at least four parameters per pulse, though the number could conceivably be reduced if, for example, all pulses within an individual burst have the same rise time to decay time ratio (which is not the case). It may be desirable to have pulses that approach or reach zero far from the pulse peaks, rather than to use a function, such as a polynomial, that would have to be cut off at the point where they take a zero value. Examination of burst time profiles reveals other properties that would be desirable in these pulses. One is that they should be able to have a discontinuous first derivative, or cusp, at the peak.

One such pulse model is the phenomenological pulse model of Norris *et al.* [19, 22] In this model (see Figure 3.1), each pulse is described by five parameters, with the functional form

$$I(t) = A \exp\left(-\left|\frac{t - t_{\max}}{\sigma_{r,d}}\right|^{\nu}\right), \tag{3.1}$$

where $t_{\max}$ is the time at which the pulse attains its maximum, σ_r and σ_d are the rise and decay times, respectively, A is the pulse amplitude, and ν (the "peakedness") gives the sharpness or smoothness of the pulse at its peak. As ν increases, the peak of the pulse

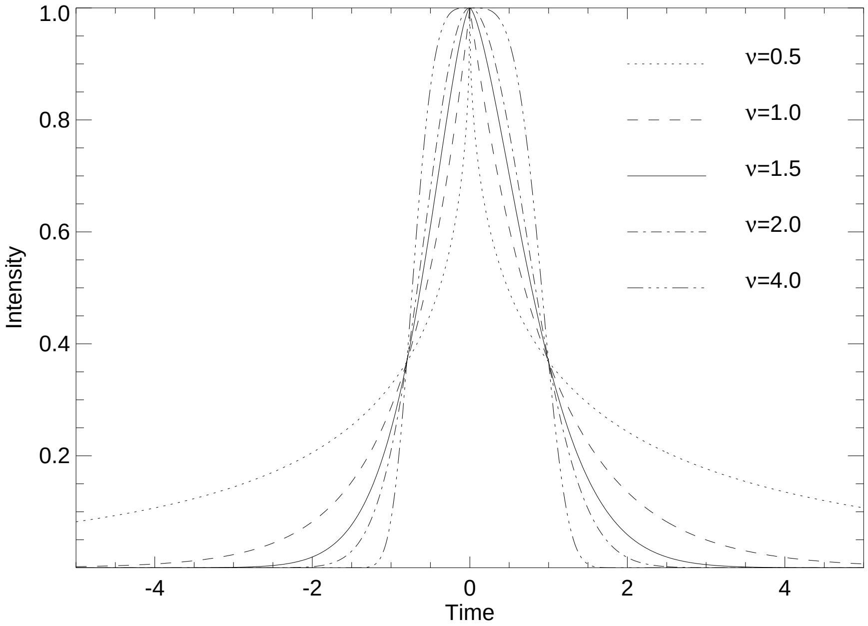

Figure 3.1: Sample pulses, $A = 1$, $t_{\max} = 0$, $\sigma_r = 0.8$, $\sigma_d = 1.0$.

becomes more rounded, and as ν becomes very large, the pulse approaches a square pulse. As ν decreases, the peak of the pulse becomes sharper, and as ν approaches 0, the pulse becomes a sharp, narrow spike. For $\nu = 1$, the rise and decay are both simple exponentials, and for $\nu = 2$, the rise and decay are Gaussian. Pulses can, and frequently do, overlap. Stern, *et al.* [56] have used the same functional form to fit averaged time profiles (ATPs) of entire bursts.

Since a pulse reaches zero height only infinitely far in the past and future, the width, or duration, of a pulse must be measured by the length of the time interval where the pulse is above a specified fraction f of its maximum height. This width is

$$T_f = A(\sigma_r + \sigma_d)(-\ln f)^{\frac{1}{\nu}}. \tag{3.2}$$

The simplest case is $f = 1/e$, for which $t_{1/e} = \sigma_r + \sigma_d$. A commonly used measure for widths of pulses (not specific to this model, or to gamma-ray burst time profiles) is the full width at half maximum (FWHM), which is the width at $f = 1/2$, and for this pulse model is given by

$$T_{\mathrm{FWHM}} = (\sigma_r + \sigma_d)(\ln 2)^{\frac{1}{\nu}}. \tag{3.3}$$

It is useful to calculate the total number of counts in a pulse, which is a measure of the *fluence*. This differs from the fluences published in the BATSE burst catalogs, which give the total energy deposited in the detectors during a burst by correcting for the energy acceptances of the detectors and fitting spectra to the count rates in different energy channels.

It is also useful to calculate the time at the centroid of a pulse. This time will differ from the peak time of a pulse, the $t_{\max}$ parameter, whenever the pulse is asymmetric ($\sigma_r \neq \sigma_d$). For a very flat-topped pulse, where the parameter ν is large, the peak time may be ambiguous, but the time at the centroid should be well-defined, since the pulse shape approaches a rectangle for large ν. For a very sharp pulse, where ν is small, the peak time is unambiguous, but the pulse will have very long tails which may make the time at the centroid very different from the peak time.

To calculate the fluence of counts of a pulse, or the time at the centroid, it is necessary to calculate the time moments of a pulse, $\int I(t)t^n dt$. Applying the substitution $t = (\sigma u)^{1/\nu}$ gives

$$\int_a^b \exp\left[-\left(\frac{t}{\sigma}\right)^\nu\right] t^n dt = \frac{\sigma^{n+1}}{\nu} \int_{(a/\sigma)^\nu}^{(b/\sigma)^\nu} u^{\frac{n+1}{\nu}-1} e^{-u} du, \tag{3.4}$$

which can be expressed in terms of the incomplete gamma function. If we truncate the integral at a fraction f of the height of a pulse, then $a = \sigma_r \ln f^{\frac{1}{\nu}}$ and $b = 0$ for the rising slope and $a = 0$ and $b = -\sigma_d \ln f^{\frac{1}{\nu}}$ for the decaying slope. For $f = 0$, the total number of counts in a pulse is given in terms of the (complete) gamma function by

$$\int_{-\infty}^{\infty} I(t) dt = \frac{\sigma_r + \sigma_d}{\nu} \Gamma\left(\frac{1}{\nu}\right) \tag{3.5}$$

and the time at the centroid of a pulse is given by

$$t_{\text{centroid}} = t_{\max} + (\sigma_d - \sigma_r) \frac{\Gamma(2/\nu)}{\Gamma(1/\nu)}. \tag{3.6}$$

3.2 The Pulse Fitting Procedure

I have developed an interactive pulse-fitting program written in IDL version 4 [57, 58, 59] using the model of Norris *et al.* [22] Unfortunately, the program doesn't display properly with the present version of IDL, version 5, because of changes to the widget libraries used to interface to X Windows and other graphics systems. The user begins by selecting a

TTS data file by the BATSE trigger number, and selects the energy channel to fit. The program can then attempt to calculate an initial guess for the fitting routine automatically, as follows: The program calculates the logarithms of the individual spill times to obtain transformed data with statistical errors of constant magnitude. It performs wavelet denoising, as described in Section B.1, on the transformed spill times using the Haar wavelet (Equation B.1) to produce a smoothed transformed time profile, and exponentiates this to obtain a smoothed time profile. The wavelet denoising is not performed in the time domain, but in the spill number domain, or equivalently, the count domain. The resulting smoothed time profile is composed of a sequence of step functions of various amplitudes, and is constant between these steps. The program graphically displays both the time profile and the wavelet-denoised time profile in a main window, and a residual time profile and residual wavelet-denoised time profile in a residuals window. The residual time profile is initially set equal to the normal time profile, because the initial fit is zero.

The program can use the longest constant interval to determine a constant background rate, which is subtracted from the smoothed time profile to produce a residual. The user can also manually set an initial background rate with a constant slope by selecting two points to determine slope and intercept of the corresponding line. The background line is displayed in the primary window, and subtracted from the residual time profiles displayed in the residuals window.

The program can then automatically search for the single largest amplitude pulse it can find, and subtract this pulse to produce a residual time profile. It does this by finding the interval with the highest count rate, and determining the peak time $t_{\max}$ and amplitude A of the pulse from this. It finds a local minimum occurring before this maximum, and fits the rise time σ_r and a peakedness parameter ν_r for the rising slope using one data point from each constant interval between the maximum and the local minimum. It uses the same procedure to find the decay time σ_d and a peakedness parameter ν_d for the decaying slope, and calculates an averaged peakedness parameter for the entire pulse, $\nu = (\nu_r + \nu_d)/2$. If there aren't enough data points (different constant intervals) in either the rising or decaying slope to fit the two parameters for that slope, then the peakedness parameter is fixed to that calculated for the other slope, and only the rise or decay is fit for that slope. If neither slope has enough data points to fit two parameters for each slope, then the procedure fails and no pulse is added.

The program can also iterate this search, each time finding the largest amplitude pulse in the residual time profile and subtracting it to produce a new residual, and stopping when the search fails as described above. The user can manually select a location (time) in either the main or residuals window to search for a pulse, and the program will determine whether the location falls on a rising or decaying slope, and follow the slope upwards to find the nearest local maximum, after which it applies the procedure described above. However, if there aren't enough data points to determine the two parameters for each of the rising or decaying slopes, the program uses a fixed peakedness parameter $\nu = 1.5$, which is close to the median value of ν for all pulses, and fits the rise and decay times.

The user can also manually add a pulse by selecting, in either window, the peak, and one point on each of the rising and decaying slopes, and the program will add a pulse by fixing the peakedness parameter at $\nu = 1.5$, calculating the peak time and amplitude and fitting the rise and decay times. In addition, the user can select any pulse to delete in either window. After adding or deleting pulses, the user can have the program search again for one or more pulses. As pulses are added or deleted, the main and residuals windows are updated accordingly.

The user can then have the program fit the pulse parameters to the actual time profile. The fitting routine uses a version of the standard IDL routine `CURVEFIT`,[60] modified to perform a maximum-likelihood fit for the gamma distribution (Equation 2.1) that the TTS spill times follow, rather than the usual χ^2 fit appropriate for data that follow a normal distribution. The algorithm used by this routine is the Levenberg-Marquardt gradient-expansion method, which is described in Appendix C. After the fitting routine stops, either because the fit has converged, or because the fit has failed to converge at all, the user can manually add or delete pulses, or have the program search for more pulses, and refit. Figures 3.2 and 3.3 show the time profiles and fits for two bursts in energy channel 3.

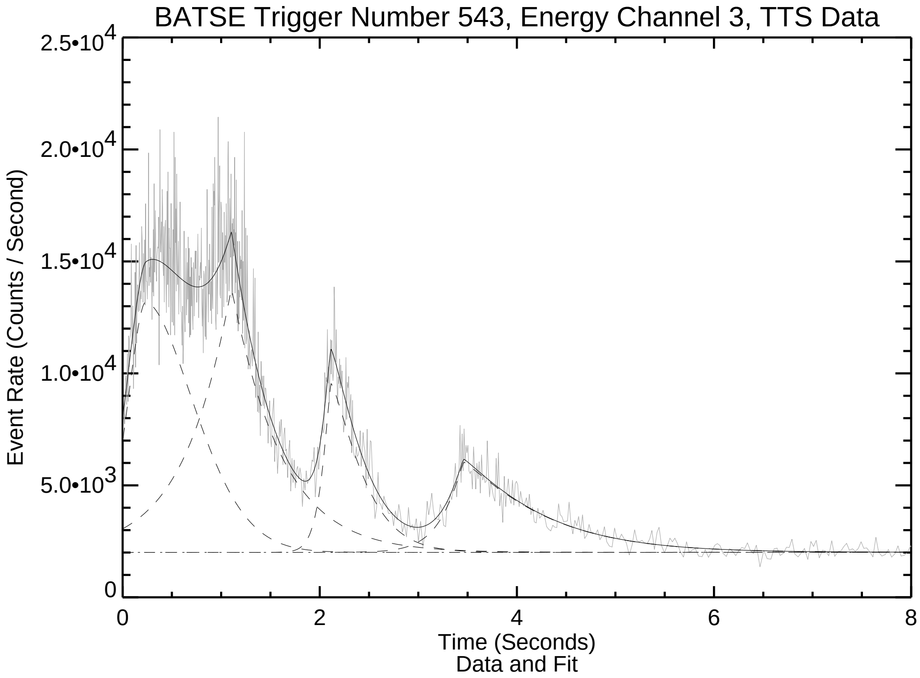

Figure 3.2: Time profile and fitted pulses for BATSE Trigger Number 543. Gray is TTS data, dash-dotted line is fitted background, dashed lines are fitted pulses, solid line is total fit.

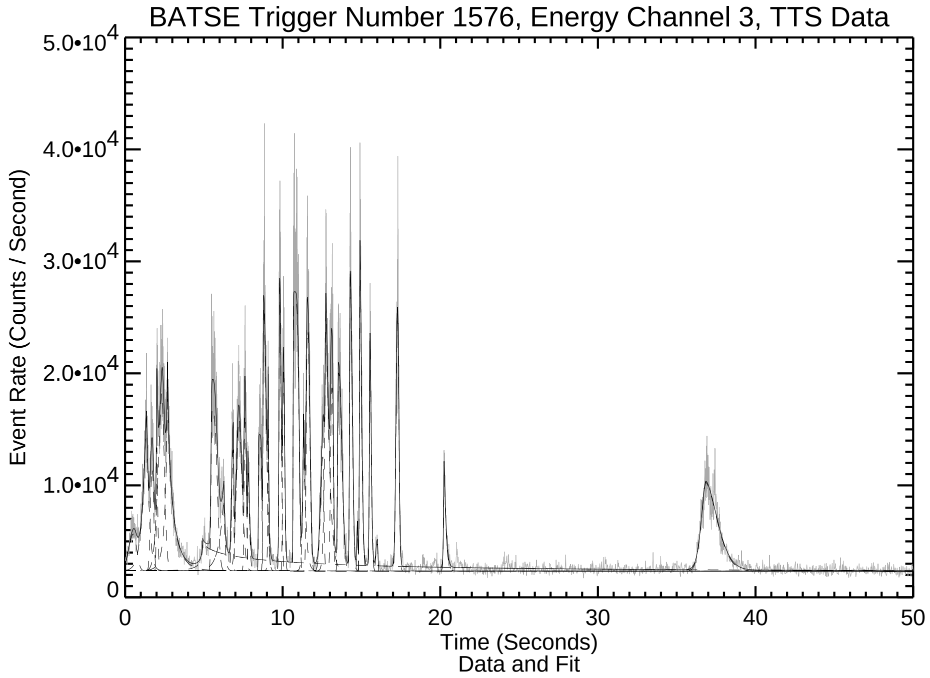

Figure 3.3: Time profile and fitted pulses for BATSE Trigger Number 1576. Gray is TTS data, dash-dotted line is fitted background, dashed lines are fitted pulses, solid line is total fit.

Chapter 4

General Characteristics of Fitted Pulses

The first part of this chapter will describe the statistical properties of the various pulse characteristics obtained from applying the pulse-fitting procedure to BATSE GRB time profiles. Of these pulse characteristics, the two brightness measures, the amplitude of the highest pulse and the total count fluence of a burst, depend on the distances from the Earth to the bursters, as well as on the intrinsic brightnesses of the bursters. The timescale measures, the pulse widths and the intervals between pulses, depend on the cosmological time dilation factor $1+z$ as well as on the intrinsic timescales of the bursters. The remaining pulse characteristics, the pulse asymmetry and the peakedness parameter ν, give the shapes of pulses and are not directly affected by the distances to the bursters, though they may be affected by the signal-to-noise ratios compared with background, which does depend on the distances to the bursters. The effects of distance and cosmological time dilation will be discussed further in the next chapter.

Following the statistical properties of pulse characteristics will be a discussion of how pulse characteristics tend to evolve with time within bursts. This chapter will end with some examples of constraints on possible models of the burst production mechanism that these results impose. The next chapter, Chapter 5 will examine whether burst time profiles show evidence of cosmological time dilation, or whether the time profiles are more strongly affected by properties of the burst production mechanism itself or by selection effects. Chapter 6 will examine possible selection effects arising from the pulse-fitting procedure by comparing of simulated bursts generated with known characteristics against fits to simulated data generated from these artificial bursts.

4.1 Numbers of Bursts and Pulses

I used my program to fit pulses to the time profiles of all bursts observed by BATSE for which TTS data were available, up to trigger number 2000, in all energy channels that contained valid data and showed temporal structure above the Poisson noise of the background. This covers the period from April 21, 1991 to October 22, 1992, during which BATSE detected a total of 461 bursts. TTS data files exist for 404 of these bursts. Some time profiles, most often in energy channel 4, $E > 325$ keV, showed no activity other than the background, and weren't fitted in those energy channels. Some of these may have been very short bursts that ended before the burst trigger time, and so weren't represented in the TTS data. Time profiles that contained data gaps were only fitted for the interval between the burst trigger and the first data gap, since the absolute times of spills after data gaps cannot be determined. A few contained data gaps at the very beginning, immediately after the burst trigger, and couldn't be fitted at all. Some time profiles showed no time variation, not even the Poisson noise of the background, presumably due to data loss. A total of 211 bursts were pulse-fitted in one or more energy channels, with only 58 bursts pulse-fitted in all four energy channels, and another 70 bursts were pulse-fitted in energy channels 1, 2, and 3, but not channel 4. Table 4.1 gives the numbers of burst time profiles which were pulse-fitted in each energy channel, the total number of pulses fitted to all bursts in each energy channel, and the number of fits containing only a single pulse in each energy channel.

The number of pulses in a fit gives a measure of the complexity of the time profile. The number of pulses per fit range from 1 to 43, with smaller numbers of pulses per fit occurring more often than larger numbers of pulses. (See Figures 4.1 and 4.2 and Table 4.2.) The number of pulses per fit tends to be highest in energy channel 3, followed in order by channels 2, 1, and 4, respectively. A likely cause of this is that higher amplitude pulses are easier to identify above the background and pulse amplitudes tend to decrease in the same order; they are highest in channel 3, followed in order by channels 2, 1, and 4, as we shall see in Section 4.4.

Norris *et al.* [22] have used the pulse model of Equation 3.1 to fit the time profiles of 45

Table 4.1: Numbers of Bursts Fitted and Total Pulses.

Energy Channel	No. of Fits	Total Pulses	No. Single Pulse
1	158	526	64
2	179	776	70
3	168	883	52
4	69	280	34
Total	574	2465	220

Table 4.2: Number of Pulses per Fit.

Energy Channel	Median No. of Pulses	Mean No. of Pulses	Max. No. of Pulses	% Single Pulse
1	2	3.3	33	64/158 = 41%
2	2	4.3	36	70/179 = 39%
3	3	5.3	43	52/168 = 31%
4	2	4.1	38	34/69 = 49%
All	2	4.3	43	38%

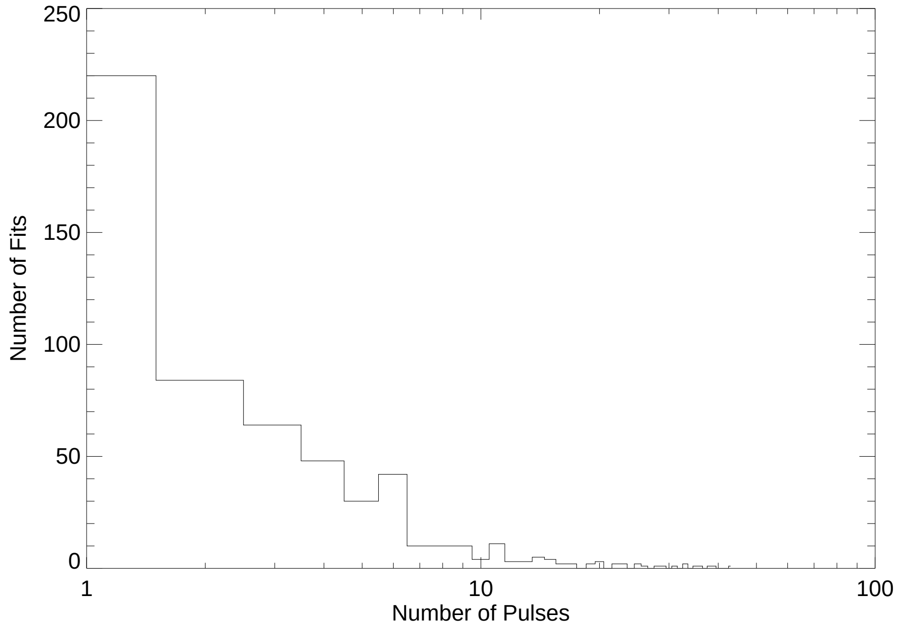

Figure 4.1: Number of pulses per fit for all energy channels combined.

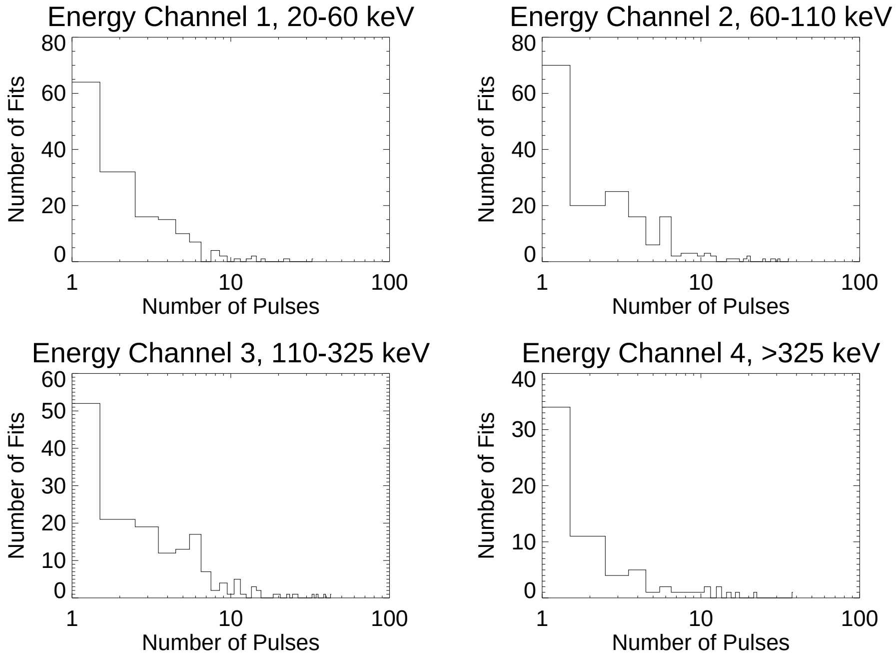

Figure 4.2: Number of pulses per fit by energy channel.

Table 4.3: Differences Between Numbers of Pulses per Fit Between Energy Channels.

Energy Channels	Median Difference	Mean Difference	$\% > 0$
2 - 1	0	1.2	$65/141 = 46\%$
3 - 2	0	1.0	$65/151 = 43\%$
4 - 3	-3	-4.3	$3/67 = 4\%$

bright, long bursts. They selected all bursts from the BATSE catalog with trigger numbers up to 2450 which had peak count rates above 18,000 counts/second on the 256 ms timescale and T_{90} durations greater than 1.5 seconds. They analyzed the BATSE PREB and DISCSC data types, which contain four-channel discriminator data with 64 ms resolution beginning 2 seconds before the burst trigger. For their selected sample of bursts, they fitted an average of 10 pulses per burst, with no time profiles consisting of only a single pulse. This number is considerably higher than the mean number of pulses per fit for my sample of bursts, probably because their sample was selected for high peak flux and long duration, which makes it easier to resolve more pulses.

Figure 4.3 and Tables 4.3 and 4.4 compare the numbers of pulses per fit between adjacent energy channels. They show that for most bursts, the numbers of pulses per fit tend to have similar variation between energy channels, *e.g.*, the bursts with the most complex time profiles in one energy channel are usually the ones that have the most complex time profiles in other energy channels. It does *not* appear, for example, that there are many bursts that are mainly active at lower energies and not at higher energies and others that are mainly active at higher energies and not at lower energies. For energy channels 1, 2, and 3, there is a slight tendency for the number of pulses in each fit to increase with energy, but in channel 4, the fits tend to have considerably fewer pulses than in channel 3. Again, this may be largely an artifact of the systematically different pulse amplitudes observed in the various energy channels. There is also considerable variation in the change in the number of pulses between energy channels 3 and 4. Pendleton, *et al.* [61, 62] call bursts that show little activity above 300 keV (approximately where energy channel 4 starts) *NHE*, or “No-High-Energy” bursts, and call those that do show activity above 300 keV *HE*, or “High-Energy” bursts, with the HE bursts containing individual peaks that may be HE or NHE.

Table 4.4: Ratios of Numbers of Pulses per Fit Between Energy Channels.

Energy Channels	Median Ratio	Geo. Mean Ratio
2 / 1	1.0	1.2
3 / 2	1.0	1.2
4 / 3	0.4	0.4

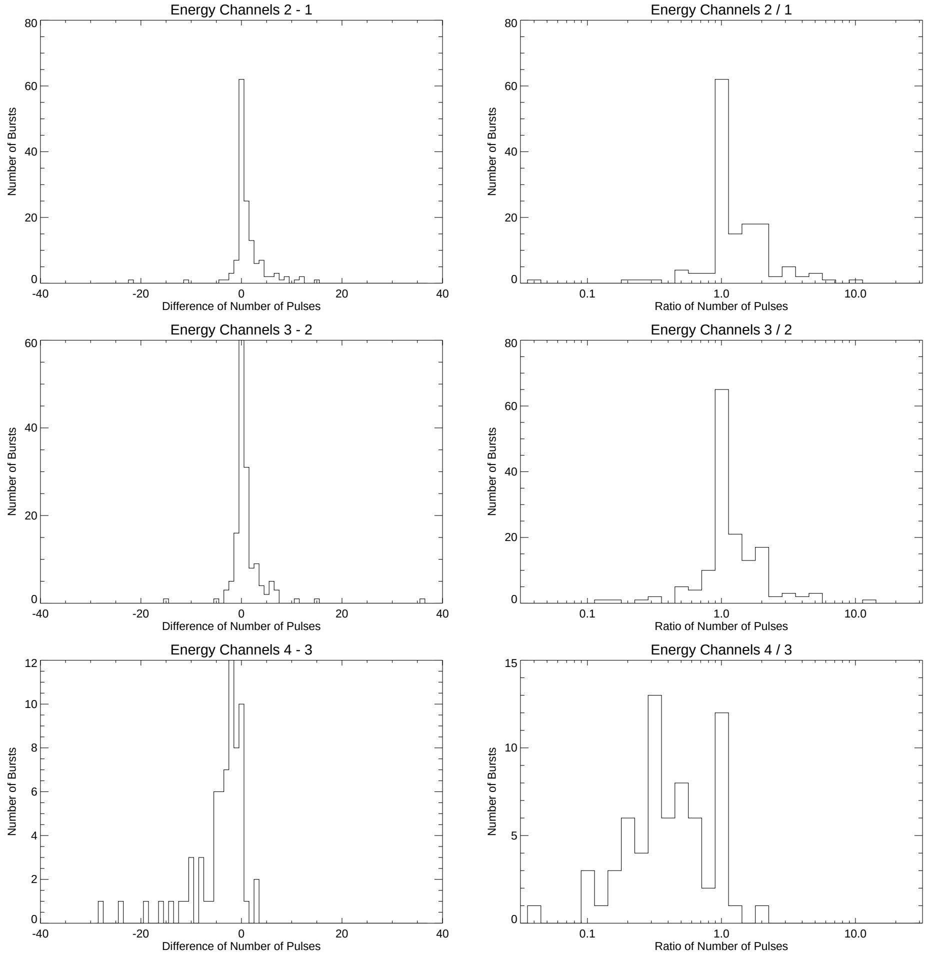

Figure 4.3: Differences and ratios of number of pulses per fit between energy channels.

A number of studies have reported differences in characteristics between "simple" and "complex" bursts, often defined as those with time profiles consisting of a single pulse and those consisting of multiple pulses, respectively. This distinction may be somewhat artificial, because many bursts may appear to be "simple" merely because their sources are more distant, so that complex structure is difficult to identify above background. In any case, in my sample of bursts, around 40% of fits in energy channels 1, 2, and 3 contained only a single pulse, while nearly 50% of fits in energy channel 4 contained only a single pulse. However, bursts that were fitted with only a single pulse in one energy channels may have been fitted with more than one pulse in other energy channels. A total of 74 bursts, 35% of the entire sample of 211 bursts, were fitted with at most one pulse in all four energy channels. The pulses from single-pulse fits make up only a small fraction of the total numbers of pulses from all fits in each energy channel, usually less than 10%, since multiple-pulse bursts contribute more to these totals.

4.2 Obtaining Statistics from Pulse Parameters

The simplest way to determine statistical properties of pulse parameters is to directly calculate them from the complete set of all pulse parameters for all fits in all energy channels, giving equal weight to each pulse. These can then be broken down into separate energy channels, or by various characteristics of the bursts represented. One drawback of this approach is that the statistics may be dominated by a small number of fits that each contain many pulses.

Another approach is to select a single pulse from each fit, either the one with the highest amplitude, or the one with the highest fluence, and calculate statistics from these representative pulses, so that each fit is equally weighted in the statistics. Again, statistics can be calculated for all fits in all energy channels, or they can be broken down by energy channel or other burst characteristics.

It is also useful to compare parameters of different pulses within individual fits, for example, to see if pulse characteristics evolve with time during a burst. For these comparisons, pulses can be ordered by their peak times, and each pulse is compared with the pulse immediately following it, or pulses can be ordered by their amplitudes or fluences, and each pulse is compared with the pulse with the next smaller amplitude or the next smaller fluence. These statistics may also be dominated by a small number of fits that each contain

Table 4.5: Numbers of Bursts Fitted with Pulses Matched Between Adjacent Energy Channels and Total Pulses.

Energy Channels	No. of Fits	Total Pulses
1 and 2	141	448
2 and 3	151	628
3 and 4	67	259

Table 4.6: Number of Pulses per Fit Matched Between Adjacent Energy Channels.

Energy Channels	Median No. of Pulses	Mean No. of Pulses	Max. No. of Pulses	% Single Pulse
1 and 2	2	3.2	29	58/141 = 41%
2 and 3	3	4.1	31	56/151 = 37%
3 and 4	1	3.9	35	34/67 = 51%

many pulses. To avoid this, one can compare the two pulses from each fit that have the highest amplitudes or the highest fluences.

The distributions of many pulse characteristics span multiple orders of magnitude, so they are plotted here on logarithmic scales. Many of these distributions also have very long tails, which can strongly affect the mean and standard deviation. In a few cases, one or more pulse parameters are obviously unreasonable. For example the TTS data contains at most $2^{20} \approx 10^6$ counts in each energy channel, and in the sample of bursts used for this analysis, ends about 240 seconds after the burst trigger. A few pulses have pulse rise times or decay times far greater than 240 seconds, or count fluences far greater than 10^6 counts, so these are clearly not reasonable fits for the data. (These problems don't occur with pulse amplitudes or pulse peak times.) For this reason, wherever possible, I use "robust" statistics, which are less sensitive to outlying points than non-robust statistics.[63] For example, I give the median of a distribution, rather than the mean, because the median depends on the zeroth moment of the distribution while the mean depends on the first moment of the distribution. To characterize the width of a distribution, I give the ratio of the 84th percentile value to the 16th percentile value. This covers the central 68% of the distribution, which for a normal distribution is the region within one standard deviation of the mean or median.

4.3 Comparing Pulse Characteristics Between Energy Channels

To see how attributes of pulses within an individual burst vary with energy, it is necessary to match pulses in different energy channels. Although burst time profiles generally have similar features in different energy channels, this matching is not straightforward, since the number of pulses fitted to a burst time profile is very often different between energy channels. I have used a simple algorithm for matching pulses between adjacent energy channels. This algorithm begins by taking all pulses from the channel with fewer pulses. It then takes the same number of pulses of highest amplitude, or alternatively of highest fluence, from the other channel, and matches them in time order with the pulses from the channel with fewer pulses. For example, the time profiles of BATSE trigger number 1577 were fitted with nine pulses in energy channel 3, and only four pulses in channel 4. This algorithm simply matches all four pulses in channel 4 in time order with the four highest ampitude pulses in channel 3, or alternatively with the four highest fluence pulses in channel 3. While this method will not always correctly match individual pulses between energy channels and will result in broad statistical distributions, it should still preserve central tendencies and yield useful statistical information.

To weight each fit equally in the statistics, one can also select the single pulse from each fit which has the highest amplitude or the highest fluence, and compare the parameters of these representative pulses between different energy channels.

Neither of these methods for comparing pulses between different energy channels allows for direct comparison among *all* energy channels. For example, the sample of pulses in energy channel 3 used to compare with channel 4 differs from the sample of pulses in channel 3 used to compare with channel 2. This problem could be avoided by making comparisons using only the bursts that have fits in all four energy channels, but since only 58 of the 211 bursts fitted were fitted in all energy channels, this would only use a small subset of the data. In addition, bursts that are pulse-fitted in energy channel 4 tend to have more pulses fitted in channel 3 than bursts that have no pulses fitted in channel 4, so using only the 58 bursts with fits in all four energy channels is likely to bias the statistics. Comparing only energy channels 1, 2 and 3 gives a much larger sample of bursts, 128 with fits in all of the lower three energy channels, but this also makes it difficult to test hypotheses, since any functional form more complex than a straight line can be fit to only three data points.

We can use the statistics from the comparisons between adjacent energy channels to determine the overall behavior, ignoring the difference in samples, *e.g.* use the median ratios of pulse widths between energy channels 1 and 2, 2 and 3, and 3 and 4 to obtain the overall variation of pulse width with energy channel.

We can also compare pulse characteristics between energy channels by comparing the distributions of the characteristics for each energy channel, without matching individual pulses at all, *e.g.* compare the median pulse widths for each energy channel.

Another difficulty in determining how pulse characteristics vary with energy is that the BATSE discriminator energy channels are broad, and their boundaries do not follow simple progressions, such as arithmetic (linear) or geometric (exponential). This makes it difficult to express pulse characteristics as a function of energy. Norris *et al.* [22] simply uses both the lowest energy of each energy channel, and the geometric mean of the lowest and highest energies of each energy channels, when fitting a functional form to the variation of a pulse characteristic with energy. Still another difficulty is that there is considerable overlap between the energy channels, which is given by the detector response matrices (DRMs).

4.4 Pulse Amplitudes

The amplitude of a pulse, parameter A in Equation 3.1, is the maximum count rate within the pulse, and measures the observed intensity of the pulse, which depends on the absolute intensity of the pulse at the burst source and the distance to the burst source. The amplitudes of the pulses fitted ranged from 40 counts/second to over 500,000 counts/second. (See Table 4.7 and Figure 4.4.) Pulses tend to have the highest amplitudes in energy channel 3, followed in order by channels 2, 1, and 4. This has been noted before [22], and is partly a result of the arbitrary widths of the energy channels, as well as the energy sensitivity of the BATSE detectors, so that the pulse amplitudes in different energy channels don't directly give spectral information. However, the ratios of these pulse amplitudes can be compared between different pulses within a burst, and between different bursts, to compare the spectral characteristics. The central 68% of the pulse amplitude distributions span a range of about one order of magnitude in each of the four energy channels, with a somewhat greater range in channel 3.

The amplitude of the highest amplitude pulse in a burst is an approximation to the

Table 4.7: Pulse Amplitudes, All Pulses in All Fits Combined.

Energy Channel	Min. Amp. (Counts / Sec.)	Median Amp. (Counts / Sec.)	Max. Amp. (Counts / Sec.)	84%ile / 16%ile
1	47	2200	136,000	10.8
2	85	2700	543,000	12.9
3	93	3000	250,000	16.2
4	43	1900	63,000	11.8

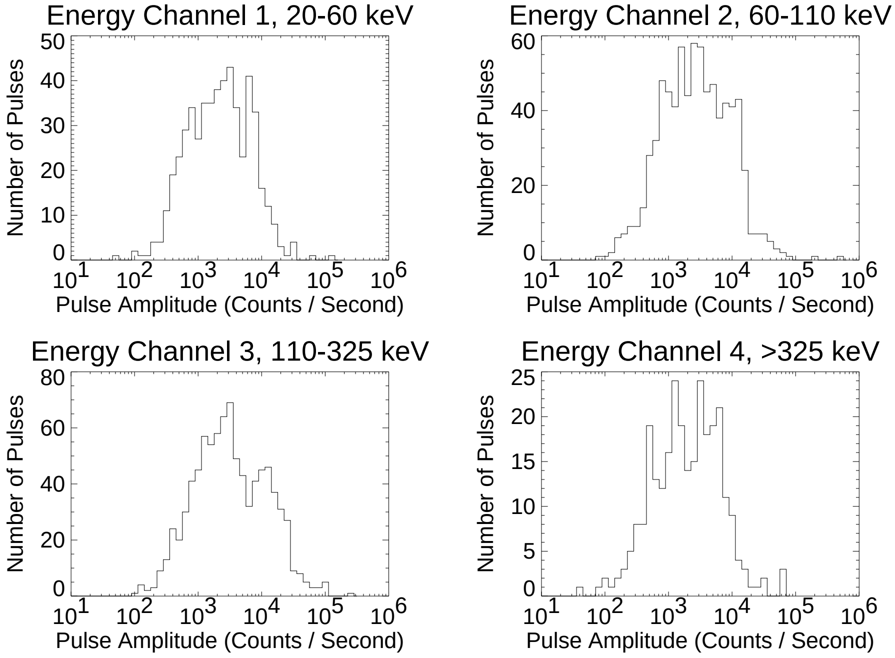

Figure 4.4: Pulse amplitudes, all pulses by energy channel.

Table 4.8: Pulse Amplitudes, Highest Amplitude Pulse in Each Fit.

Energy Channel	Min. Amp. (Counts / Sec.)	Median Amp. (Counts / Sec.)	Max. Amp. (Counts / Sec.)	84%ile / 16%ile
1	241	2200	136,000	11.1
2	148	2800	543,000	9.9
3	116	3500	250,000	12.4
4	82	1500	63,000	18.8

instantaneous peak flux above background of that burst in that energy channel. The peak flux is often used as an indicator of the distance to the burst source, and this will be discussed further in Chapter 5. Since pulses can overlap, the highest pulse amplitude can be less than the actual background-subtracted peak flux. The BATSE burst catalogs give background-subtracted peak fluxes for 64, 256, and 1024 ms time bins in units of photons/cm^2/second, for which effects such as the energy acceptances of the detectors and the orientation of the spacecraft and hence the detectors relative to the source have been accounted for and removed. The BATSE burst catalog also lists peak count rates which are not background-subtracted or corrected for any of the effects described, for 64, 256, and 1024 ms time bins in the second most brightly illuminated detector for each burst. These peak count rate are primarily useful for comparison with the BATSE event trigger criteria. In some bursts, the highest pulses are considerably narrower than the shortest time bins used to measure peak flux in the BATSE burst catalog. For these bursts, these peak fluxes will be lower than the true peak flux, and the fitted pulse amplitudes are likely to be a better measure of the true peak flux. The central 68% of the pulse amplitude distributions span a range of about one order of magnitude in each of the four energy channels, with a somewhat greater range in channel 4. (See Table 4.8 and Figure 4.5.) The observed highest pulse amplitudes depend on the intrinsic highest pulse amplitudes at the burst sources and the distances from the Earth to the burst sources.

Figure 4.6 shows the number of pulses in each fit plotted against the amplitudes of all of the pulses comprising each fit. It shows that in fits with more pulses, the minimum pulse amplitude, which can be seen from the left boundary of the distribution, tends to be higher. This could result in part from intrinsic properties of the burst sources, but may also result

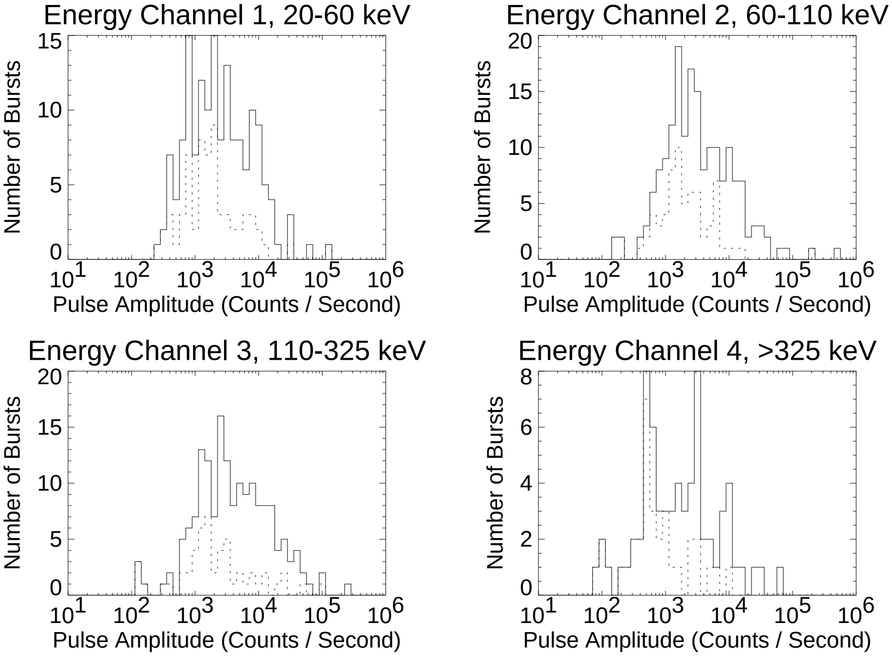

Figure 4.5: Pulse amplitudes, highest amplitude pulse in each fit by energy channel. Dashed lines are single-pulse fits.

at least in part from a selection effect: In a complex time profile with many overlapping pulses, low amplitude pulses, which have poor signal-to-noise ratios, will be more difficult to resolve, while in a less complex time profile, they will be easier to resolve. Table 4.9 shows strong positive correlations between pulse amplitudes and the number of pulses in the fit for all energy channels.

Figure 4.7 and Table 4.10 compare the number of pulses in each fit with the amplitude of the highest amplitude pulse in each fit. They show that more complex bursts tend to have higher peak count rates, as measured by the amplitude of the highest pulse. This may also result at least in part from the same selection effect described above, further enhanced because more complex bursts have more pulses to select from.

Table 4.11 shows the amplitudes of single-pulse fits, which tend to be lower than amplitudes of pulses from all fits in the same energy channels. Figure 4.5 compares the distributions of pulse amplitudes for single-pulse fits with the highest amplitude pulses from all fits.

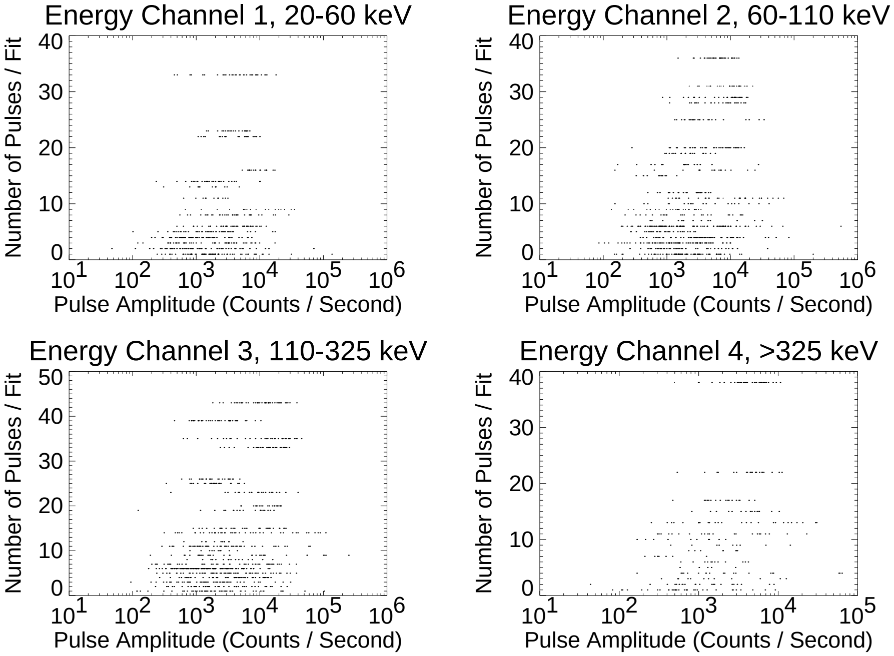

Figure 4.6: Number of pulses per fit versus pulse amplitudes of all pulses by energy channel.

Table 4.9: Correlation Between Number of Pulses per Fit and Pulse Amplitudes for All Pulses.

Energy Channel	r_s	Prob.
1	0.37	3.9×10^{-18}
2	0.36	1.8×10^{-24}
3	0.30	4.2×10^{-20}
4	0.45	2.2×10^{-15}

Table 4.10: Correlation Between Number of Pulses per Fit and Pulse Amplitudes, Highest Amplitude Pulse in Each Fit.

Energy Channel	r_s	Prob.
1	0.38	6.2×10^{-7}
2	0.44	8.2×10^{-10}
3	0.40	5.3×10^{-8}
4	0.69	5.5×10^{-11}

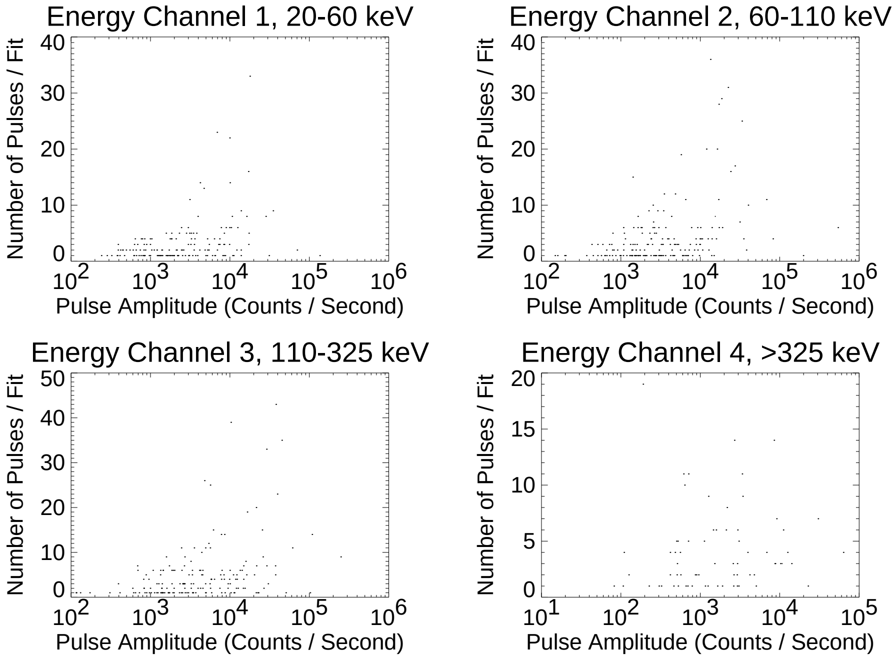

Figure 4.7: Number of pulses per fit versus pulse amplitude, highest amplitude pulse in each fit by energy channel.

Table 4.11: Pulse Amplitudes, Single Pulse Fits.

Energy Channel	Min. Amp. (Counts / Sec.)	Median Amp. (Counts / Sec.)	Max. Amp. (Counts / Sec.)	84%ile / 16%ile
1	241	1700	136,000	8.4
2	148	1700	198,000	8.3
3	116	1700	103,000	12.0
4	82	660	9200	11.9

Table 4.12: Percentage of Fits with Time Resolution < 64 ms, < 16 ms.

Energy Channel	% BG < 64 ms	% BG < 16 ms	% Peak < 64 ms	% Peak < 16 ms
1	100%	16%	100%	80%
2	100%	8%	100%	75%
3	100%	3%	100%	67%
4	68%	1%	100%	30%
All	96%	8%	100%	69%

4.5 Count Rates and Time Resolution

The fitted background rates and the amplitudes of the individual pulses can be used to determine the time resolution of the TTS data at background levels and at the peaks of the pulses. Table 4.12 shows the percentage of fits where the time resolution at background levels and at the peak of the highest amplitude pulse are finer than 64 ms and 16 ms, which are the time resolutions of the more commonly used DISCSC and MER data, respectively. The background rates are taken at the time of the burst trigger, and ignore the fitted constant slope of the background. The rates at the peaks of the highest amplitude pulses include the background rates at the peak times of the pulses calculated with the background slopes. However, these rates ignore overlapping pulses, so the actual time resolution will be finer since the actual count rates will be higher. Note that even at background levels, the TTS data always has finer time resolution than the DISCSC data, except in energy channel 4 where the DISCSC data has finer time resolution at background levels for 32% of the fits.

Table 4.13 shows the percentage of individual pulses where the TTS data has time resolution finer than 16 ms and 64 ms at the peaks. Again, the count rates include the fitted background rates at the peak times of the pulses but ignore overlapping pulses. For all individual pulses, the TTS data has finer time resolution at their peaks than the DISCSC data.

Table 4.13: Percentage of Pulses with Time Resolution < 64 ms, < 16 ms, All Fits Combined.

Energy Channel	% < 64 ms	% < 16 ms
1	100%	80%
2	100%	68%
3	100%	62%
4	100%	42%
All	100%	65%

4.6 Pulse Asymmetries

Although the pulse model uses separate rise and decay times as its basic parameters, it is often more natural to consider the widths and asymmetries of pulses, which give equivalent information to the rise and decay times. The ratios of pulse rise times to decay times σ_r/σ_d are a convenient way to measure the asymmetry of pulses. The pulse rise and decay times are the time intervals between the pulse peak and when it falls to $1/e$ of the peak height, but the asymmetry ratio is independent of the fraction of the peak height used. As noted before, the asymmetry ratios depend only on the shapes of pulses. The asymmetry ratios cover a very wide range of values, but there is a clear tendency for pulses to have slightly shorter rise times than decay times. (See Figures 4.8 and 4.9.) If, for example, individual pulses are produced by separate explosive events, then we might expect that the pulses would have shorter rise times than decay times.

We can test the hypothesis that pulses tend to be asymmetric by computing the probability that the observed numbers of pulses with asymmetry ratios less than 1 will occur by chance if asymmetry ratios less than 1 and greater than 1 are equally probable. This probability can be computed from the binomial distribution, and is shown in the last column of Table 4.14. We see that the hypothesis that pulses are symmetric is strongly excluded in energy channels 2 and 3. The probability isn't computed for all pulses in all energy channels combined, because pulses cannot be considered to be independent between energy channels. We also see that the asymmetry isn't significantly different for the different energy channels. Norris *et al.* [22] found far greater asymmetry, with average values of σ_d/σ_r (the inverse of the ratio used here) ranging from 2 to 3 for their selected sample of bursts, and about 90%

Table 4.14: Pulse Asymmetries, All Pulses in All Fits Combined.

Energy Channel	Median σ_r/σ_d	84%ile / 16%ile	% $\sigma_r < \sigma_d$	Binom. Prob.
1	0.76	16.8	297/526 = 56%	0.0030
2	0.76	16.1	457/776 = 59%	7.2×10^{-7}
3	0.71	14.0	528/883 = 60%	5.8×10^{-9}
4	0.80	15.9	158/280 = 56%	0.031
All	0.75	15.4	1440 / 2465 = 58%	

of pulses having shorter rise times than decay times.

The highest amplitude pulses in each fit also tend to have shorter rise times than decay times, though the asymmetry ratio tends to be closer to 1 than for all pulses in all fits combined. (See Figures 4.10 and 4.11.) In all energy channels except 2, the observed distributions of asymmetry ratios could be produced by symmetric pulses. We can use the Kolmogorov-Smirnov test [64] to determine if the distributions of asymmetry ratios for the highest amplitude pulses in each fit are the same as for all pulses in all fits combined. These results are shown in the last column of Table 4.15, and the K-S test doesn't find any significant differences between the distributions for the highest amplitude pulses and for all pulses. On the other hand, the binomial distribution test doesn't exclude the possibility that the highest amplitude pulses in each fit are symmetric. The reason for these two seemingly contradictory results is that the sample of fits in each energy channel isn't large enough to draw statistically significant conclusions about the asymmetry of the highest amplitude pulse in each fit.

For bursts with time profiles composed of a single pulse, the rise-to-decay time ratios tend to be larger than for pulses in more complex bursts, except for energy channel 4. (See Table 4.16.) In energy channels 1 and 3, most single-pulse bursts have longer rise times than decay times, though the observed distribution asymmetry ratios in all energy channels could be produced by symmetric pulses. The distribution of asymmetry ratios is much broader for single-pulse fits than for all pulses in all fits combined, and the Kolmogorov-Smirnov test gives some evidence that the distributions aren't the same for single pulse fits as for all pulses.

Comparison of pulse asymmetries of pulses matched between adjacent energy channels

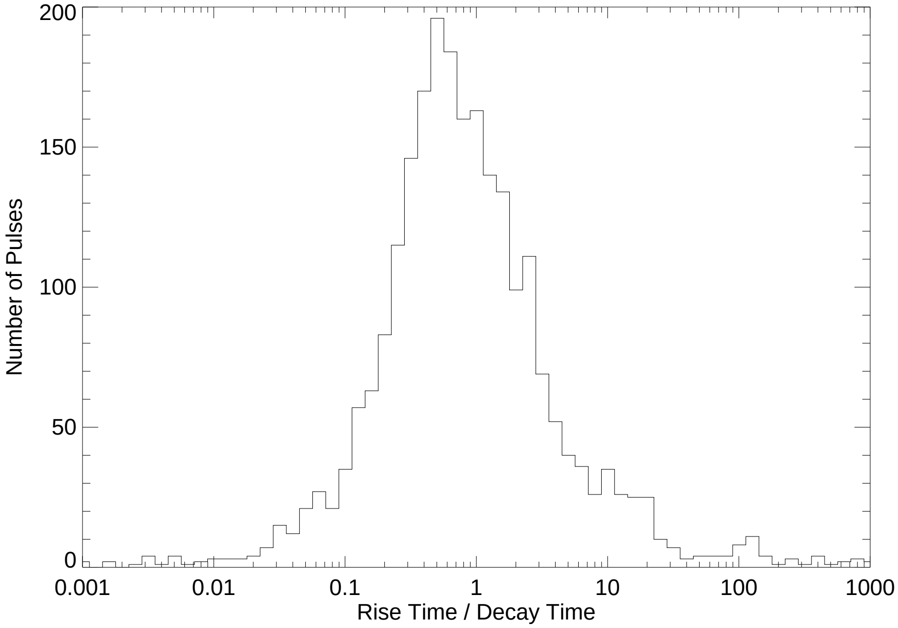

Figure 4.8: Pulse asymmetries, all pulses in all energy channels combined.

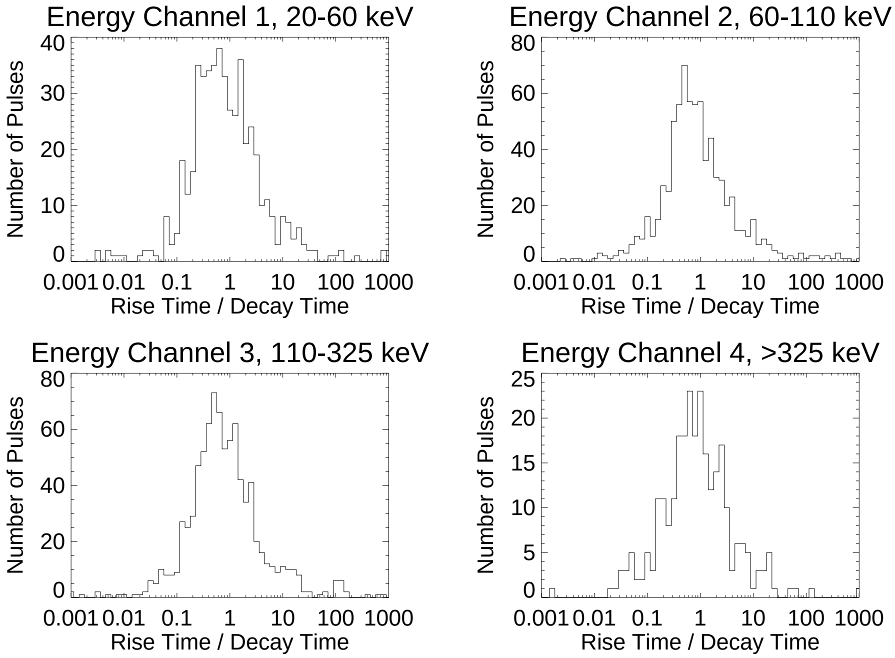

Figure 4.9: Pulse asymmetries, all pulses by energy channel.

Table 4.15: Pulse Asymmetries, Highest Amplitude Pulse in Each Fit.

Energy Channel	Median σ_r/σ_d	84%ile / 16%ile	% $\sigma_r < \sigma_d$	Binom. Prob.	K-S Prob.
1	0.90	21.3	83/158 = 53%	0.52	0.34
2	0.76	28.6	106/179 = 59%	0.014	0.64
3	0.96	13.5	88/168 = 52%	0.54	0.22
4	0.80	41.8	36/69 = 52%	0.72	0.77
All	0.86	22.1	313/574 = 55%		

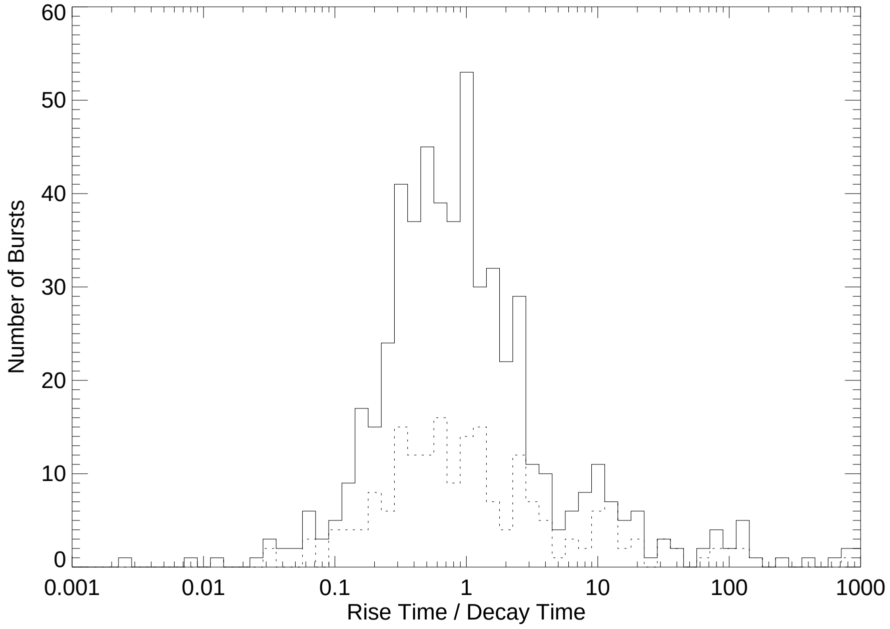

Figure 4.10: Pulse asymmetries, highest amplitude pulse in each fit, all energy channels combined. Dashed line is single-pulse fits.

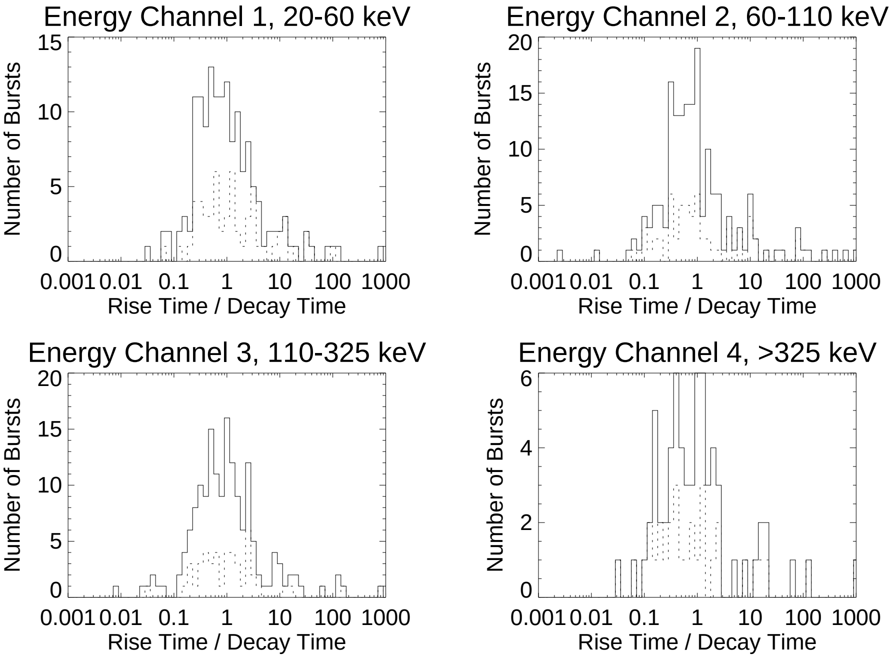

Figure 4.11: Pulse asymmetries, highest amplitude pulse in each fit by energy channel. Dashed lines are single-pulse fits.

Table 4.16: Pulse Asymmetries, Single Pulse Fits.

Energy Channel	Median σ_r/σ_d	84%ile / 16%ile	% $\sigma_r < \sigma_d$	Binom. Prob.	K-S Prob.
1	1.35	59.0	27/64 = 42%	0.21	0.013
2	0.98	112.8	37/70 = 53%	0.63	0.0055
3	1.15	49.0	24/52 = 46%	0.58	0.098
4	0.77	127.2	20/34 = 59%	0.79	0.48
All	1.12	95.8	108/220 = 49%		

Table 4.17: Ratios of Pulse Asymmetries Between Pulses Matched Between Adjacent Energy Channels

Energy Channels	Median Ratio of Asymmetries	% < 1	Binom. Prob.	K-S Prob.
2 / 1	0.98	229/446 = 51%	0.57	0.29
3 / 2	0.97	318/625 = 51%	0.66	0.31
4 / 3	1.03	127/258 = 49%	0.80	0.62

Table 4.18: Pulse Widths, All Pulses in All Fits Combined.

Energy Channel	Median FWHM (Seconds)	84%ile / 16%ile
1	1.86	19.9
2	1.05	23.0
3	0.68	22.9
4	0.41	21.4
All	0.90	27.0

doesn't show any tendencies for the asymmetry ratios to be larger or smaller at higher energy channels. (See Table 4.17.)

4.7 Pulse Widths

Pulse widths, or durations, are timescales that are likely to be characteristic of the physical processes that produce gamma rays at the burst sources. Since some, and possibly all, bursts are produced at cosmological distances, all observed timescales, including pulse widths, will be affected by cosmological time dilation, and won't represent the physical timescales at the sources. This will be discussed further in Chapter 5. I use the full-width at half-maximum, T_{FWHM} given by Equation 3.3, to measure the widths, or durations, of pulses. Widths of individual pulses have a range of about a factor of 20. The distributions of the pulse widths peak near one second in all energy channels. Pulses tend to be narrower (shorter) at higher energies. (See Figures 4.12 and 4.13 and Table 4.18.)

The highest amplitude pulses in each fit tend to be wider than other pulses in the same

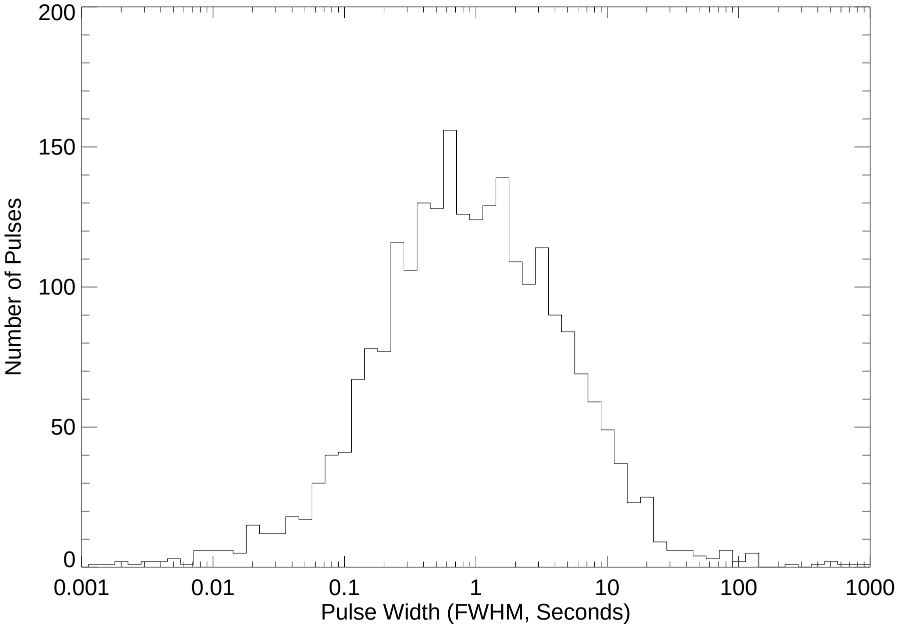

Figure 4.12: Pulse widths (FWHM), all pulses in all energy channels combined.

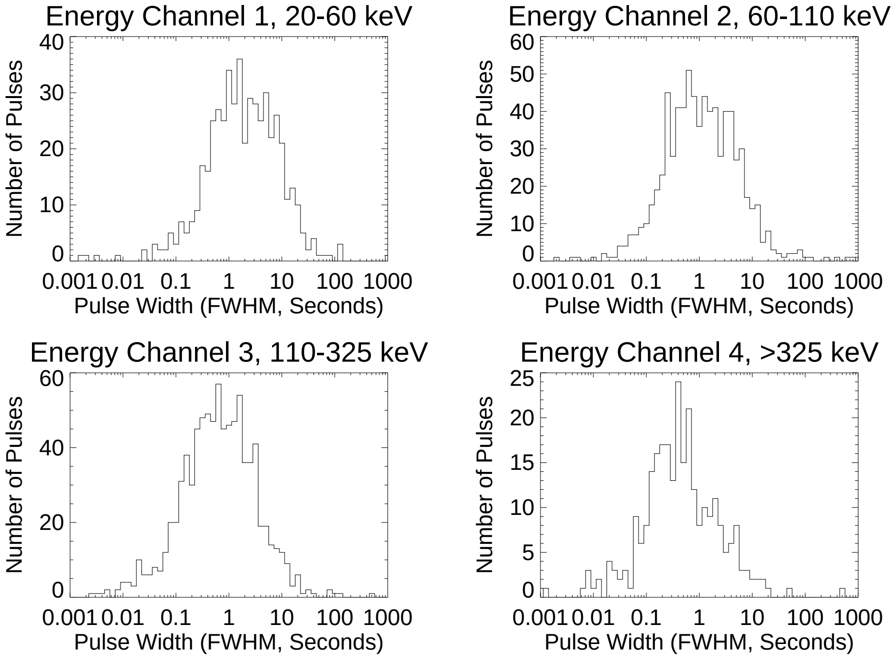

Figure 4.13: Pulse widths (FWHM), all pulses by energy channel.

Table 4.19: Pulse Widths, Highest Amplitude Pulse in Each Fit.

Energy Channel	Median FWHM (Seconds)	84%ile / 16%ile
1	2.99	32.7
2	1.50	63.0
3	0.69	63.8
4	0.65	269
All	1.39	78.3

fit in all energy channels. These pulses also tend to become narrower at higher energies. The distribution of widths of the highest amplitude pulses is much broader than the distribution of widths of all pulses. (See Figures 4.14 and 4.15 and Table 4.19.) As with all timescales, the variation in observed pulse widths results from a combination of the intrinsic variation in pulse widths at the burst sources and possible cosmological time dilation effects.

The narrowing of pulses in higher energy channels can also be measured from the ratios of pulse widths of pulses matched between adjacent energy channels, as shown in Table 4.20. This shows less narrowing than a simple comparison of median pulse widths from Table 4.18 would suggest, though the pulse width ratios have a significant tendency to be less than 1. The pulse width ratios tend to be closer to 1 between energy channels 3 and 4, so there is less narrowing than between the lower energy channels, although the statistics are poorer, as with anything involving channel 4. Norris *et al.* [22] found the opposite tendency, for the pulse narrowing to be greater between energy channels 3 and 4. The table gives the probability for the pulse narrowing from channel 2 to channel 3 to occur by chance only as $< 10^{-16}$ because, on the computers that were used, roundoff error causes the standard IDL function `BINOMIAL` [60] to return 0 for any probabilities smaller than $2^{-53} \approx 10^{-16}$. (I do not know what the corresponding thresholds are for the probabilities associated with the Spearman rank-order coefficient correlation coefficients given by `R_CORRELATE` and with the Kolmogorov-Smirnov test given by `KSTWO`, so these are simply listed as 0 here.) The Kolmogorov-Smirnov test also shows significant differences in the distribution of pulse widths of matched pulses between adjacent energy channels.

The narrowing of pulses at higher energies appears to be caused by the burst production mechanism itself. This could arise, for example, if lower energy gamma-rays are produced

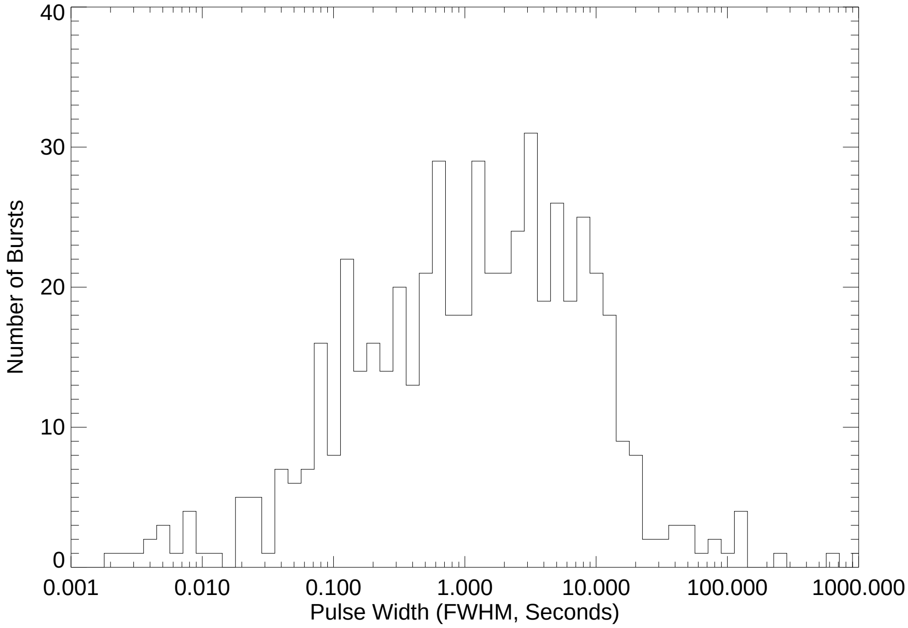

Figure 4.14: Pulse widths (FWHM), highest amplitude pulse in each fit, all energy channels combined.

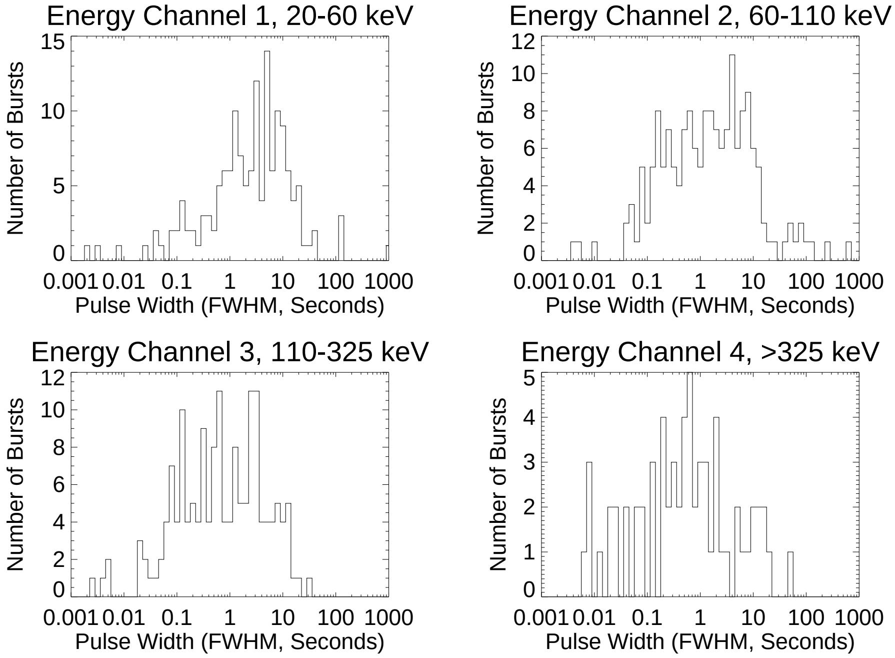

Figure 4.15: Pulse widths (FWHM), highest amplitude pulse in each fit, by energy channel.

Table 4.20: Ratios of Pulse Widths of Pulses Matched Between Adjacent Energy Channels.

Energy Channels	Median Width Ratio	% < 1	Binom. Prob.	K-S Prob.
2 / 1	0.73	304/446 = 68%	1.7×10^{-14}	1.1×10^{-5}
3 / 2	0.68	436/625 = 70%	$< 10^{-16}$	8.7×10^{-7}
4 / 3	0.83	153/258 = 59%	0.0028	0.62

Table 4.21: Correlation Between Number of Pulses per Fit and Widths of All Pulses.

Energy Channel	r_s	Prob.
1	-0.36	1.8×10^{-17}
2	-0.35	8.0×10^{-24}
3	-0.23	9.4×10^{-12}
4	-0.28	1.3×10^{-6}

by scattering of higher energy gamma-rays, which would naturally broaden pulses at lower energies. We might also expect this to cause pulses to peak later at lower energies, which does occur, as we shall see in Section 4.9. The only other possible cause for the narrowing of pulses is that it is an effect of the differing signal-to-noise ratios in the different energy channels, but if this were the case, we wouldn't expect a monotonic decrease of pulse width with increasing energy, since pulse amplitudes generally increase from channel 1 to 3, then decrease from channel 3 to 4.

Figure 4.16 and Table 4.21 compare the number of pulses in each fit with the widths of the individual pulses. They show that pulses tend to be narrower in bursts with more pulses. This may be an intrinsic property of GRBs, or it may be a selection effect arising because narrower pulses have less overlap with adjacent pulses, hence they are easier to resolve, so more pulses tend to be identified in bursts with narrower pulses. This may also be a side effect of correlations between other burst and pulse characteristics with the number of pulses per fit and the pulse widths.

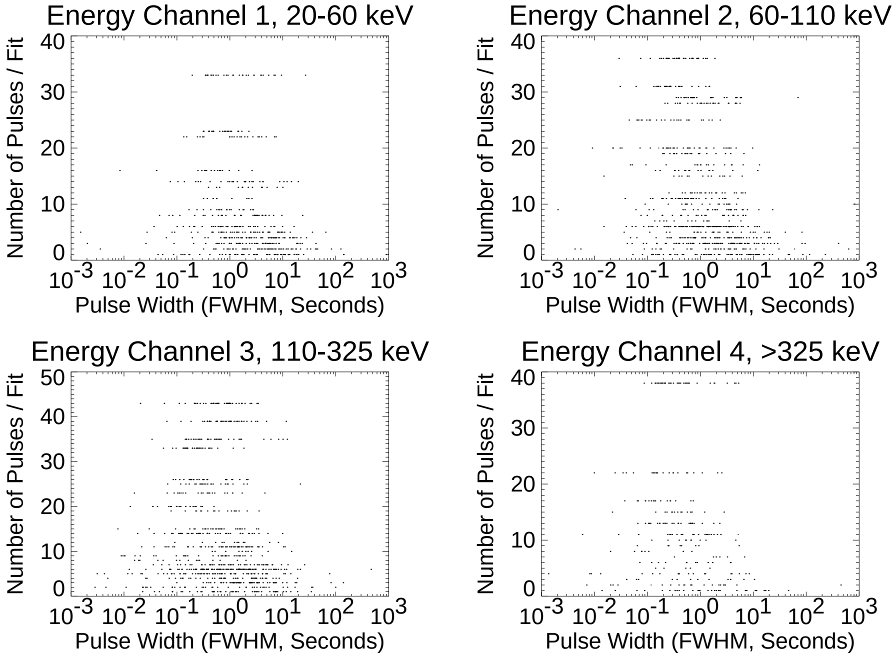

Figure 4.16: Number of pulses per fit versus widths of all pulses, by energy channel.

4.8 Time Intervals Between Pulses

In addition to pulse widths, the time intervals between pulses within bursts are timescales that may also be characteristic of the gamma-ray production mechanisms in gamma-ray bursts. We'll examine the intervals between consecutive pulses first. If the individual pulses are produced by independent events, then the time intervals between consecutive pulses would be expected to obey Poisson statistics, with the distribution of pulse intervals following a decaying exponential distribution, or a flat distribution when histogrammed with logarithmic bins.[22] The intervals between peak times $t_{\max}$ of consecutive pulses clearly don't obey Poisson statistics. (See Figures 4.17 and 4.18.) However, this may result from a selection effect: Two pulses with short separations between their peaks may have a large overlap, and thus be identified as only one pulse, which may limit the shortest observed interval between pulses. On the other hand, when two pulses have a large separation between them, additional smaller pulses may be resolved between them that wouldn't be resolved if the separation were smaller, which may limit the the longest observed intervals between consecutive pulses.

Table 4.22: Intervals Between Peak Times of Consecutive Pulses, All Pulses in All Fits Combined.

Energy Channel	Min. Interval (Sec.)	Median Interval (Sec.)	Max. Interval (Sec.)	84%ile / 16%ile
1	0.042	3.91	146	15.7
2	0.044	2.35	146	18.8
3	0.020	1.67	134	16.2
4	0.044	1.10	137	12.3
All	0.020	2.11	147	18.7

The median intervals between consecutive pulses are shorter at higher energies. This is similar to the tendency for the pulses widths to be narrower at higher energies, and is likely to be a selection effect caused by this narrowing of pulses. It is interesting to note that the range of values spanned by the intervals between consecutive pulses is slightly smaller than the range of values spanned by the pulse widths, as measured by the ratio of the 84th percentile to the 16th percentile values, *i.e.*, there is slightly less variation in the intervals between consecutive pulses than in the pulse widths.

Table 4.23 shows the ratios of intervals between consecutive pulses matched between adjacent energy channels. It shows a slight tendency for intervals between pulses to be shorter at higher energies, except between energy channels 3 and 4. This effect is smaller than that observed by simply comparing the median intervals in different energy channels. The latter effect may result from resolving more low-amplitude pulses between the higher amplitude pulses at higher energies, because the pulses are narrower at higher energies, and the process of matching individual pulses between adjacent energy channels can eliminate this selection effect. Here, it seems somewhat unphysical for the intervals between matched pulses to be shorter at higher energies, especially if we believe that individual pulses represent distinct events within the burst source. As noted earlier, the process for matching pulses between energy channels is not at all perfect, which may be the cause of this result.

Of the 1881 intervals between peak times of consecutive pulses in all fits in all energy channels, only 46 of the intervals, fewer than 2.5%, are shorter than 128 ms, the length of two time bins of the DISCSC data. This suggests that the binned data has sufficient time resolution to resolve the peaks of separate pulses and the local minimum between them in

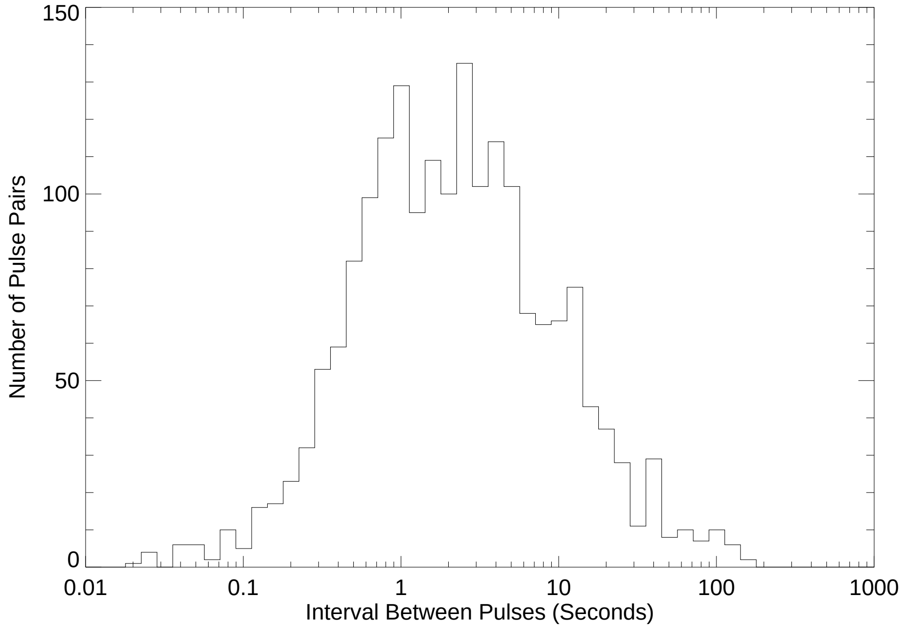

Figure 4.17: Intervals between peak times of consecutive pulses, all pulses in all energy channels combined.

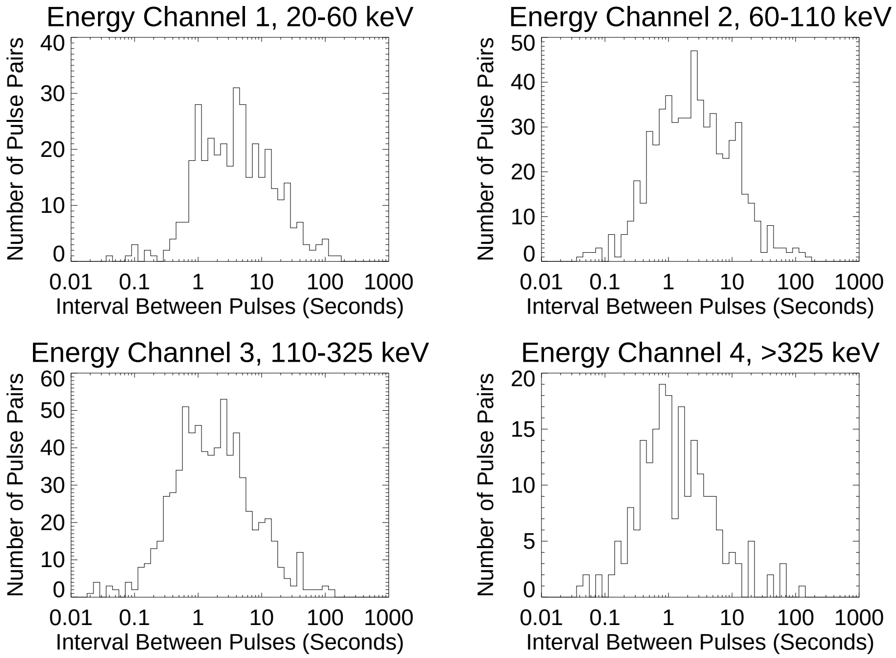

Figure 4.18: Intervals between peak times of consecutive pulses, all pulses by energy channel.

Table 4.23: Ratios of Intervals Between Consecutive Pulses Matched Between Adjacent Energy Channels.

Energy Channels	Median Interval Ratio	$\% < 1$	Binom. Prob.	K-S Prob.
2 / 1	0.95	$179/305 = 59\%$	0.0024	0.042
3 / 2	0.92	$290/474 = 61\%$	1.1×10^{-6}	0.0015
4 / 3	1.00	$93/191 = 49\%$	0.72	0.98

Table 4.24: Correlation Between Number of Pulses per Fit and Intervals Between Adjacent Pulses.

Energy Channel	r_s	Prob.
1	-0.39	1.8×10^{-14}
2	-0.47	3.0×10^{-33}
3	-0.24	1.6×10^{-10}
4	-0.27	8.0×10^{-5}

nearly all cases, although it may not be sufficient to determine the shapes of those pulses accurately.

Figure 4.19 and Table 4.24 compare the number of pulses in each fit with the time intervals between the peak times of consecutive pulses. They show that pulses tend to be closer together in bursts with more pulses. One selection effect that may contribute to this result is that more complex bursts may simply be bursts with stronger signal-to-noise ratios, which allows more pulses to be resolved within any given time interval.

The time interval between the peak times of the first and last pulses in a burst might be expected to give a good measure of the total duration of the burst, but the determination of this interval can be greatly affected by whether or not low amplitude pulses can be identified above background. This is essentially the same effect as the sensitivity of the T_{90} interval to the signal-to-noise ratios of bursts.[65, 66]

Figure 4.20 and Table 4.25 compare the number of pulses in each fit with the time interval between the first and last pulses in each fit. They show that the time intervals between the first and last pulse are greater in bursts with more pulses. This may result from the selection effect described above.

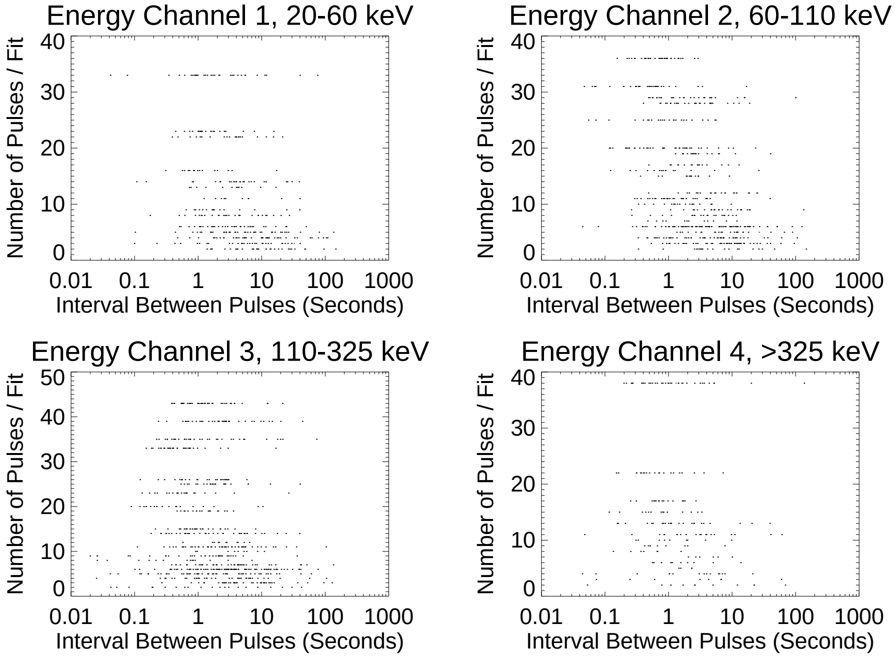

Figure 4.19: Number of pulses per fit versus intervals between adjacent pulses by energy channel.

Table 4.25: Correlation Between Number of Pulses per Fit and Intervals Between First and Last Pulse.

Energy Channel	r_s	Prob.
1	0.53	3.6×10^{-8}
2	0.50	2.7×10^{-8}
3	0.56	4.4×10^{-11}
4	0.52	0.0013

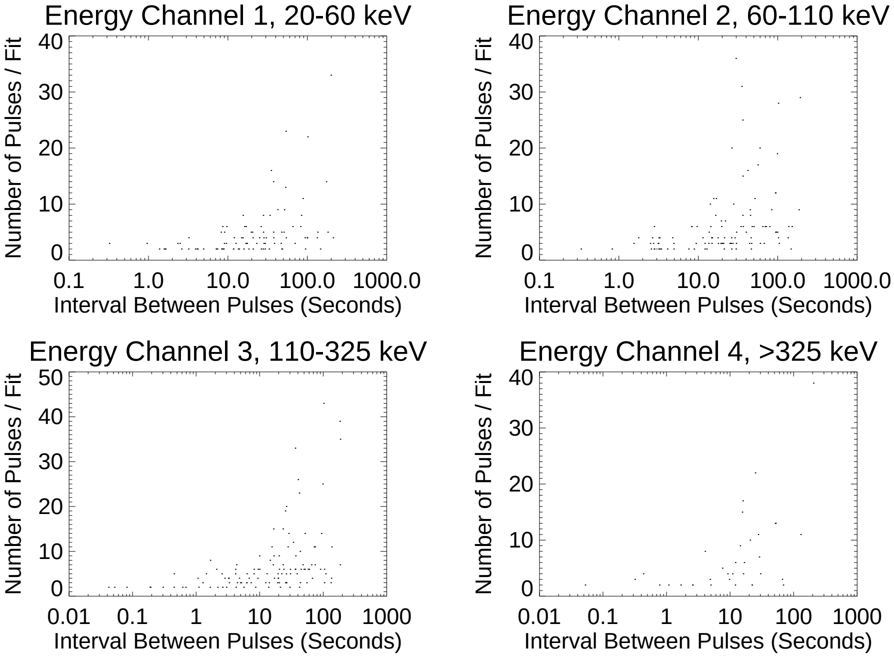

Figure 4.20: Number of pulses per fit versus interval between first and last pulse in each fit by energy channel.

The time interval between the peak times of the two highest amplitude pulses in a burst gives a characteristic time scale for the entire burst. Determination of this interval should be less affected by selection effects due to finite pulse widths than determination of the intervals between consecutive pulses. However, the identification of the two highest pulses may be affected by whether a particular structure in a burst is identified as a single pulse with large amplitude or as multiple overlapping pulses with smaller amplitudes. If pulses are independent events, then these intervals should also obey Poisson statistics, which they clearly don't. (See Figure 4.21.) The interval between the two highest amplitude pulses should be less influenced by the selection effects that affect the interval between the first and last pulses in a burst. We see that the range of values spanned by the intervals between the two highest pulses in a burst is somewhat smaller than the range of values spanned by the pulse widths of the highest amplitude pulses in a burst, as measured by the ratio of the 84th percentile to the 16th percentile values. (See Table 4.26.)

The ratios of intervals between the two highest pulses of each burst between adjacent energy channels don't show any consistent tendency for shorter or longer intervals at higher

Table 4.26: Intervals Between Peak Times of the Two Highest Amplitude Pulses in Each Fit, All Fits Combined.

Energy Channel	Min. Interval (Sec.)	Median Interval (Sec.)	Max. Interval (Sec.)	84%ile / 16%ile
1	0.15	7.4	176	20.1
2	0.19	6.2	188	20.2
3	0.04	3.7	104	30.2
4	0.05	2.6	69	16.7
All	0.04	5.0	188	23.8

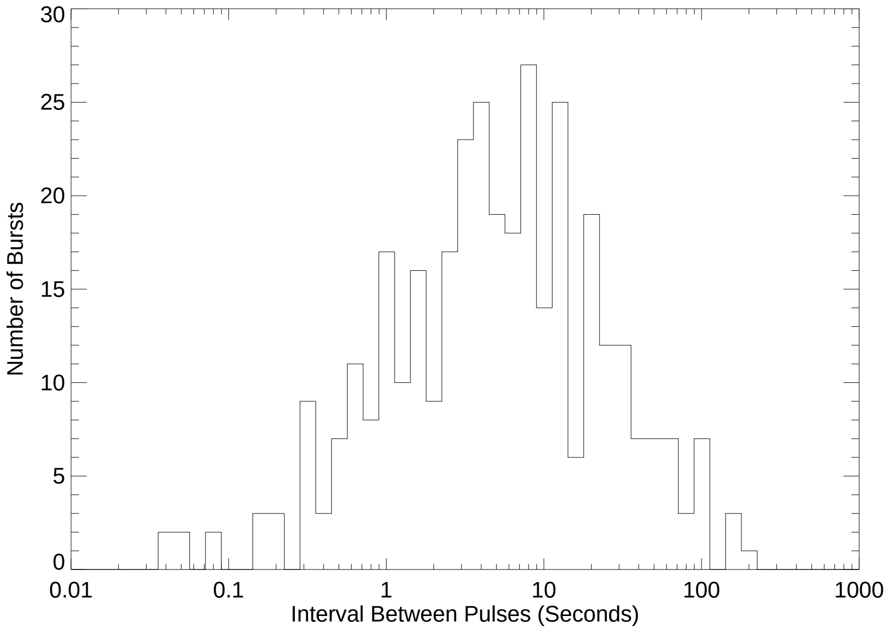

Figure 4.21: Intervals between peak times of the two highest amplitude pulses in all fits in all energy channels combined.

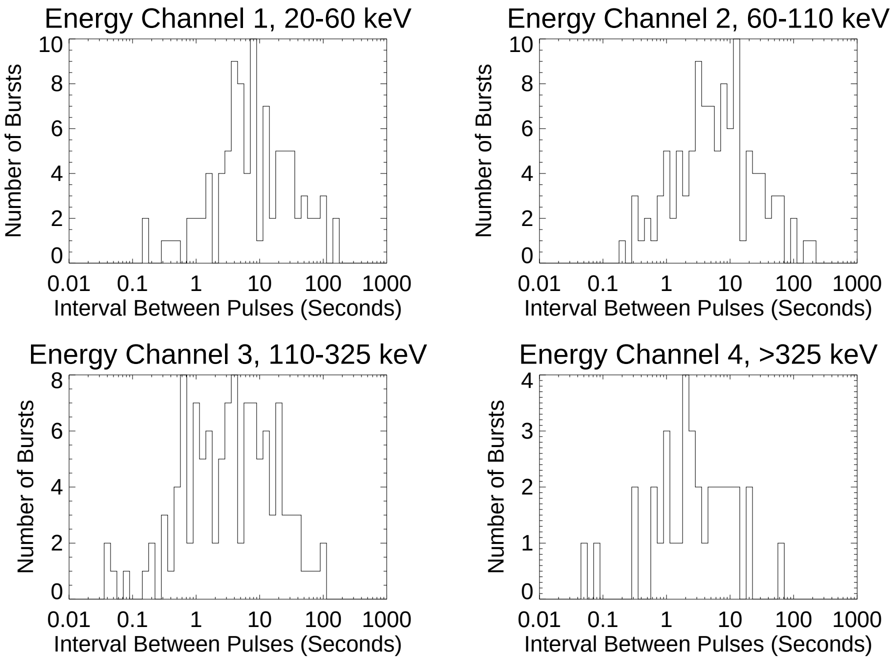

Figure 4.22: Intervals between peak times of the two highest amplitude pulses in all fits, by energy channel.

energies. (See Table 4.27.)

Figure 4.23 and Table 4.28 compare the number of pulses in each fit with the time intervals between the peak times of the two highest amplitude pulses in each fit. They show no tendency for these intervals to be shorter or longer in bursts with more pulses. This suggests that the interval between the two highest pulses in each fit isn't subject to the signal-to-noise selection effect described above for the intervals between adjacent pulses, or for the interval between the first and last pulse in each fit.

Table 4.27: Ratios of Intervals Between Two Highest Pulses Between Adjacent Energy Channels.

Energy Channels	Median Interval Ratio	% < 1	Binom. Prob.	K-S Prob.
2 / 1	0.98	44/83 = 53%	0.29	0.98
3 / 2	0.98	55/95 = 58%	0.062	0.77
4 / 3	1.02	13/33 = 39%	0.11	0.96

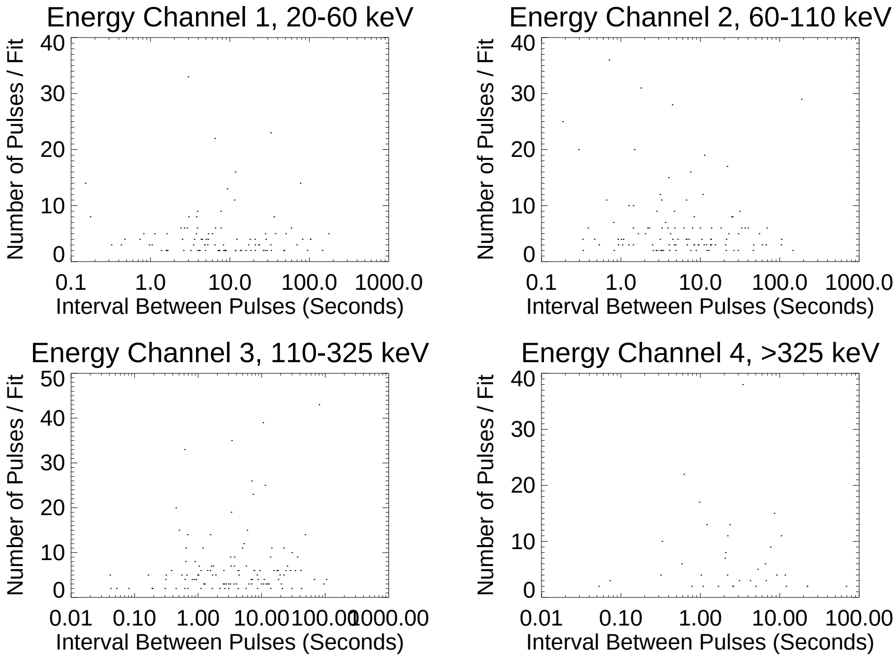

Figure 4.23: Number of pulses per fit versus intervals between two highest amplitude pulses in each fit by energy channel.

Table 4.28: Correlation Between Number of Pulses per Fit and Intervals Between Two Highest Amplitude Pulses in Each Fit.

Energy Channel	r_s	Prob.
1	-0.07	0.50
2	-0.12	0.23
3	0.14	0.13
4	-0.16	0.35

Table 4.29: Time Delays Between Peak Times of Pulses Matched Between Adjacent Energy Channels.

Energy Channels	Median Time Lag (Seconds)	% > 0	Binom. Prob.
1 - 2	0.11	290/446 = 65%	2.2×10^{-10}
2 - 3	0.27	459/625 = 73%	$< 10^{-16}$
3 - 4	0.01	140/258 = 54%	0.17

Table 4.30: Time Delays Between Peak Times of Highest Amplitude Pulses in Each Fit.

Energy Channels	Median Time Lag (Seconds)	% > 0	Binom. Prob.
1 - 2	0.08	95/141 = 67%	3.7×10^{-5}
2 - 3	0.05	97/151 = 64%	0.00047
3 - 4	0.14	47/67 = 70%	0.00097

4.9 Time Delays Between Energy Channels

Table 4.29 shows the differences, or time delays, between the peak times of pulses matched between adjacent energy channels. It shows a significant tendency for individual pulses to peak earlier at higher energies. This has been previously observed, and described as a hard-to-soft spectral evolution of the individual pulses.[67, 22] The time delays found here are greater than those found by Norris, *et al.* [22], who found an average pulse peak time delay between adjacent energy channels of $\sim$ 20 ms.

Comparing the peak times of the highest amplitude pulses in each fit between adjacent energy channels also shows a significant tendency for bursts to peak earlier at higher energies. (See Table 4.30.)

It has been suggested that gamma-ray bursts could be used to test the *in vacuo* energy dispersion of electromagnetic radiation that arises in some quantum gravity theories.[68] However, this suggestion is based on the assumption that gamma-ray arrival times from bursts differ by less than 0.01 seconds for energies separated by $\approx$ 200 keV, so that quantum gravity effects are the dominant source of energy differences in gamma-ray arrival times. It appears from the pulse-fitting data that the time lags are far greater than this amount over an energy separation of this size within the BATSE energy range, so that other effects are larger than the expected quantum gravity effects.

Table 4.31: Peakedness Parameter ν, All Pulses in All Fits Combined.

Energy Channel	Median ν	84%ile / 16%ile
1	1.22	5.3
2	1.26	5.6
3	1.26	5.7
4	1.17	5.8
All	1.25	5.6

The time delays between energy channels observed here and elsewhere are likely to result from intrinsic properties of the burst sources. As discussed earlier, in Section 4.7, one way this could arise could be that lower energy gamma-rays are produced by scattering of higher energy gamma-rays at or very near the source.

4.10 The Peakedness Parameter ν

The relation of the peakedness parameter ν to physical characteristics of gamma-ray burst sources is far less clear than for other pulse attributes. Nevertheless, it does give information that can be used to compare the shapes of different pulses. The peakedness ν has a median value near 1.2 in all energy channels, so that pulses tend to have shapes between an exponential, for which $\nu = 1$, and a Gaussian, for which $\nu = 2$. (See Figures 4.24 and 4.25 and Table 4.31.) Stern, *et al.* [56] use the functional form of Equation 3.1 to fit averaged time profiles of many bursts rather than individual constituent pulses, and find that $\nu \approx 1/3$ for the *averaged time profiles.*

The highest amplitude pulses in each fit tends to have a smaller value of ν, so that these pulses have sharper peaks and more slowly falling tails. The single-pulse fits show a similar distribution. The Kolmogorov-Smirnov test shows that the distributions of ν for both the highest amplitude pulses in each fit and the single-pulse fits are significantly different from the distributions for all pulses in all fits combined. It shows no significant differences between the distributions of ν for the highest amplitude pulses in each fit and for the single pulse fits. It is unclear why this occurs. One possible reason is that unresolved pulses contribute to the tails of these pulses, making them fall off more slowly and decreasing the values of ν

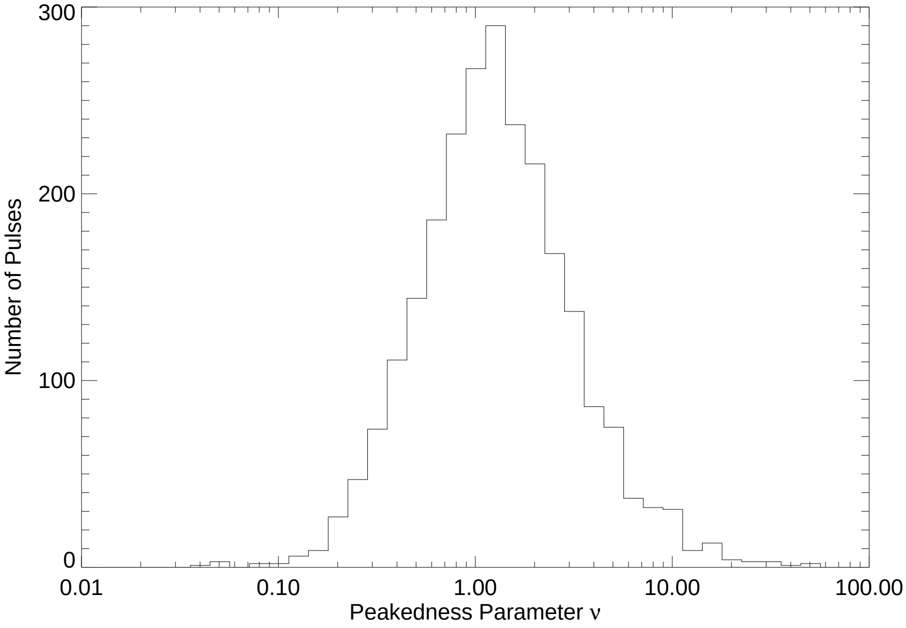

Figure 4.24: Peakedness ν, all pulses in all energy channels combined.

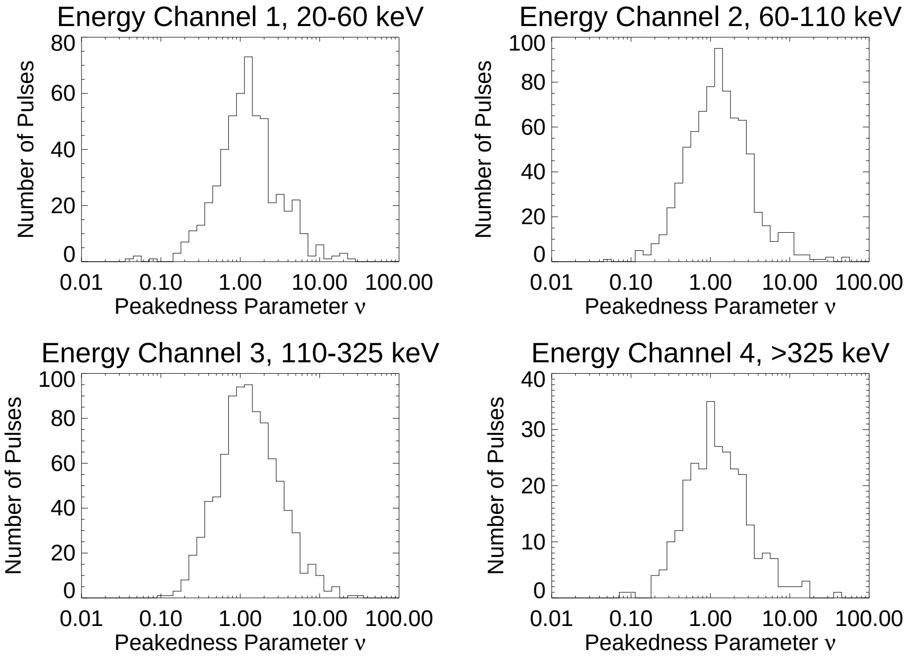

Figure 4.25: Peakedness ν, all pulses by energy channel.

Table 4.32: Peakedness Parameter ν, Highest Amplitude Pulse in Each Fit.

Energy Channel	Median ν	84%ile / 16%ile	K-S Prob.
1	0.94	3.8	2.8×10^{-5}
2	0.93	3.7	2.2×10^{-7}
3	0.88	4.4	3.1×10^{-6}
4	0.82	5.1	0.010
All	0.91	4.1	

Table 4.33: Peakedness Parameter ν, Single-Pulse Fits.

Energy Channel	Median ν	84%ile / 16%ile	K-S Prob. vs. All	K-S Prob. vs. Highest
1	0.96	3.1	0.00097	0.95
2	0.90	3.0	5.3×10^{-6}	0.78
3	0.86	4.6	0.00023	0.60
4	0.63	4.0	0.0066	0.73
All	0.88	4.0		

fitted. The distributions of ν for the highest amplitude pulses and for the single-pulse fits are both slightly narrower than for all pulses.

Comparison of the ratio of ν between pulses matched between adjacent energy channels doesn't show any significant tendency for pulses to have larger or smaller values of ν in adjacent energy channels. This implies that the results of comparing pulse widths between different energy channels using the full width at half maximum should be similar to those that would be obtained using the full width of pulses at other fractions of their peak heights.

4.11 Count Fluences of Bursts and Individual Pulses

The area of a pulse, which is given by Equation 3.5, is the total number of counts contained in the pulse, which is the count fluence of the pulse. This gives the apparent integrated luminosity of the pulse, which depends on the total absolute luminosity of the pulse and the distance to the burst source. The count fluence can be directly calculated from its

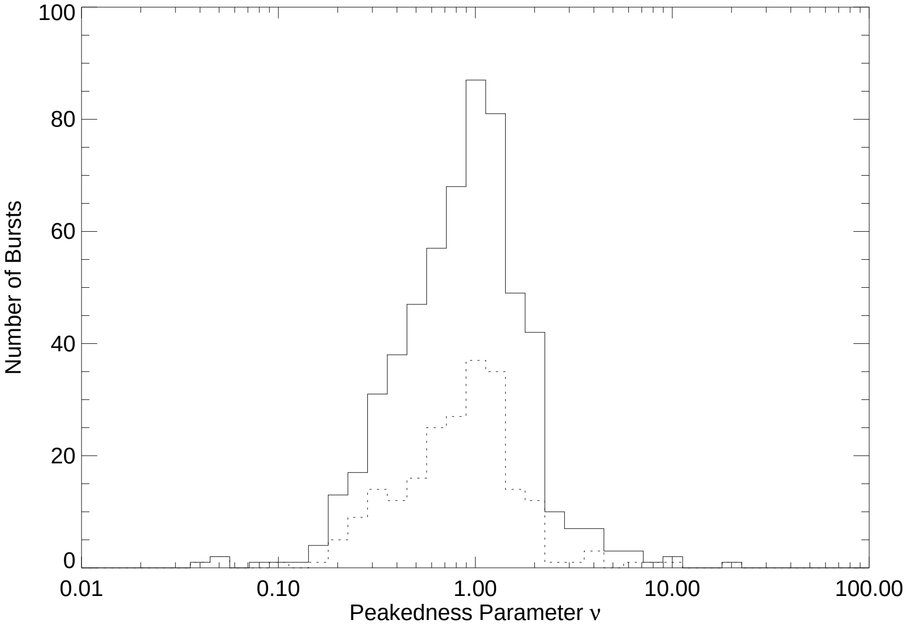

Figure 4.26: Peakedness ν, highest amplitude pulse in each fit, all energy channels combined. Dashed line is single-pulse fits.

Table 4.34: Ratios of Peakedness ν Between Pulses Matched Between Adjacent Energy Channels

Energy Channels	Median Interval Ratio	% < 1	Binom. Prob.	K-S Prob.
2 / 1	0.95	233/446 = 52%	0.34	0.53
3 / 2	0.96	323/625 = 52%	0.40	0.90
4 / 3	0.94	136/258 = 53%	0.38	0.25

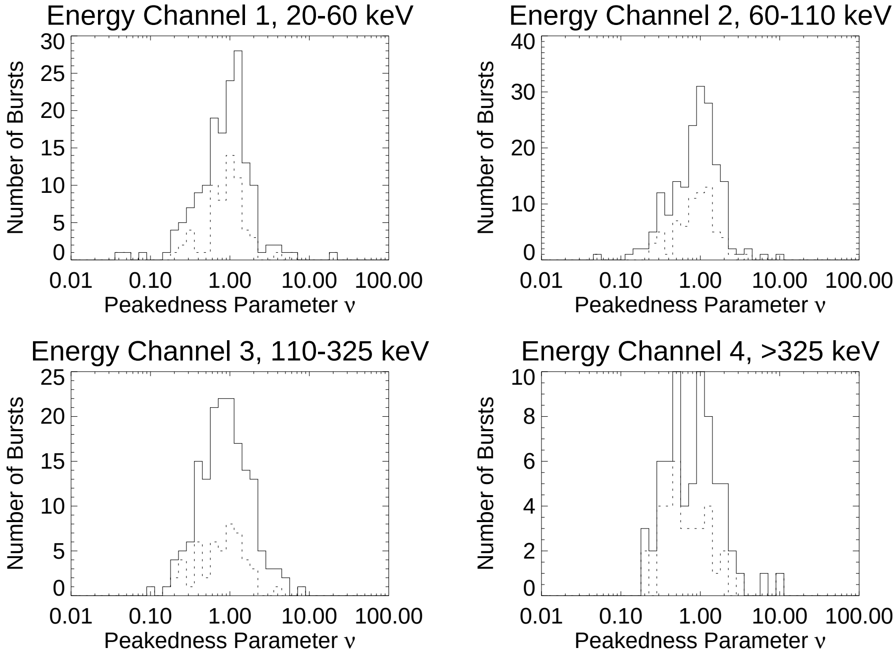

Figure 4.27: Peakedness ν, highest amplitude pulse in each fit by energy channel. Dashed lines are single-pulse fits.

parameters as the product of the pulse amplitude, the sum of the pulse rise and decay times (or any other measure of the pulse width), and a function of the peakedness ν, as shown in Chapter 3.1. The count fluences of all pulses in a fitted time profile for a burst in a particular energy channel can be summed to give the total count fluence for that burst in that energy channel. The total count fluence can be used as another indicator of the distance to the burst source, and this will be discussed further in Chapter 5. The count fluences can also be summed across different energy channels for individual pulses or bursts. Individual pulses and entire bursts both tend to have higher count fluences in lower energy channels, although the count fluences depend in part on the energy channel boundaries, just as the pulse amplitudes do. The pulse count fluences span a range of values almost twice as large as the range spanned by the pulse amplitudes.

Figure 4.29 shows the number of pulses in each fit versus the count fluences of the individual pulses. It shows that in bursts containing more pulses, the individual pulses tend to contain fewer counts. This suggests that the tendency for pulses to be narrower in more complex bursts is stronger than the tendency for pulses to have higher amplitudes

Table 4.35: Pulse Count Fluences, All Pulses in All Fits Combined.

Energy Channel	Median Fluence (Counts)	84%ile / 16%ile
1	7400	15.6
2	5100	20.6
3	3780	23.5
4	1480	20.8

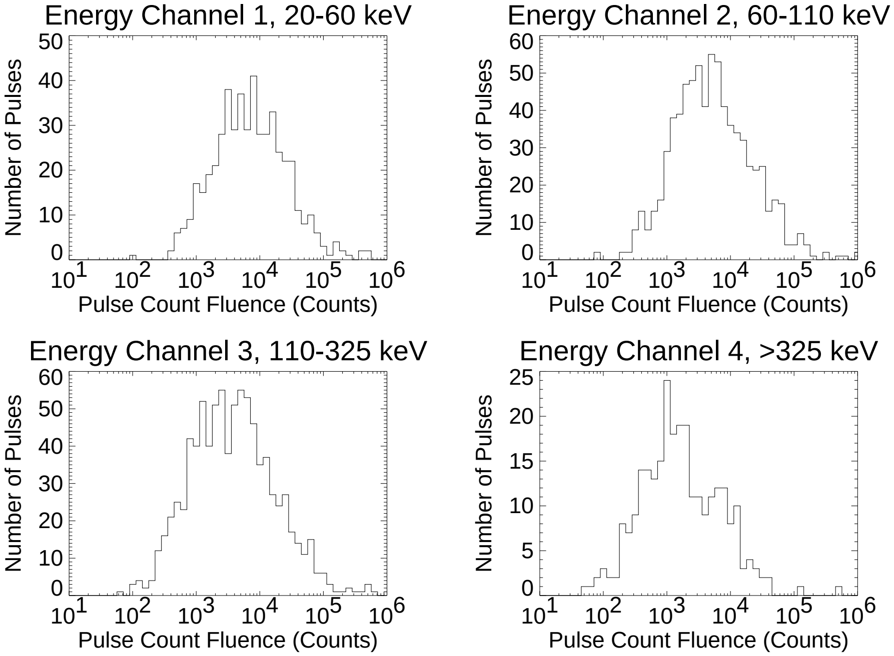

Figure 4.28: Pulse count fluences, all pulses by energy channel.

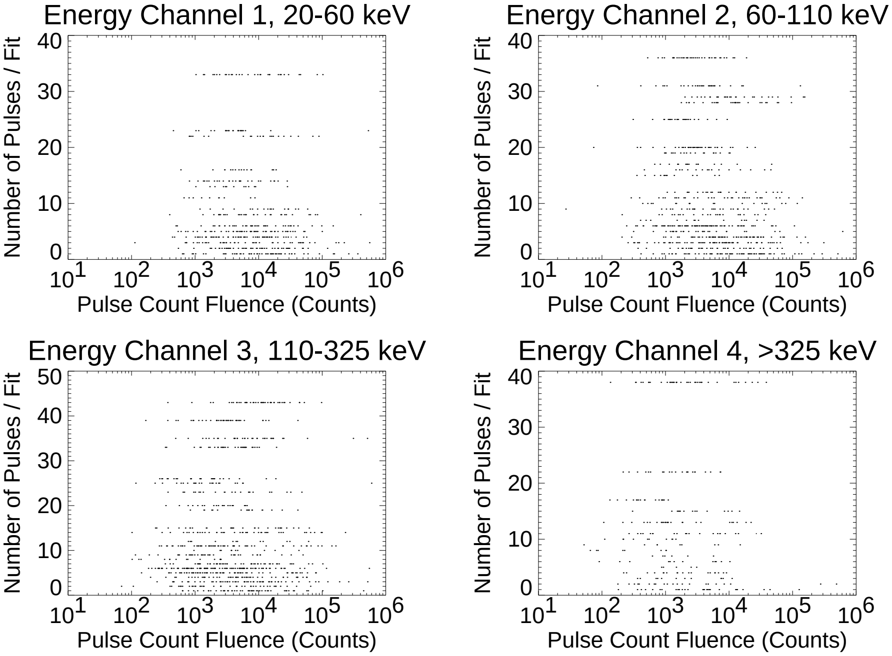

Figure 4.29: Number of pulses per fit versus count fluences of all pulses, by energy channel.

in more complex bursts. Table 4.36 shows that the corresponding negative correlations are statistically significant in energy channels 1 and 2, but not in channels 3 and 4.

Table 4.37 gives the median total burst count fluences, and Table 4.38 gives the minimum, median, and mean percentages of the total burst count fluences that are contained in the single pulse with highest count fluence in each fit, and the percentage of bursts where a single pulse contains more than 50% of the total count fluence. (The maximum percentage of the total burst count fluences that are contained in a single pulse is 100% for all channels, which occurs for all single-pulse fits. A single pulse necessarily contains at least 50% of the

Table 4.36: Correlation Between Number of Pulses per Fit and Count Fluences of All Pulses.

Energy Channel	r_s	Prob.
1	-0.17	9.2×10^{-5}
2	-0.20	3.4×10^{-8}
3	-0.04	0.21
4	-0.13	0.027

Table 4.37: Total Burst Count Fluences.

Energy Channel	Median Fluence (Counts)	84%ile / 16%ile
1	32,300	36.7
2	32,300	39.9
3	27,900	76.2
4	9400	176.6

Table 4.38: Fraction of Total Burst Count Fluences Contained in a Single Pulse.

Energy Channel	Min. % in 1 Pulse	Median % in 1 Pulse	Mean % in 1 Pulse	% > $\frac{1}{2}$ Fluence in 1 Pulse
1	17%	94%	79%	84%
2	12%	96%	76%	74%
3	12%	75%	71%	57%
4	12%	100%	75%	72%

total count fluence in any fit consisting of one or two pulses.) It is common for a single pulse to contain a large fraction of the total count fluence of a burst.

Figure 4.32 shows the number of pulses in each fit versus the total count fluences of the bursts. It shows that bursts with more pulses tend to contain more total counts. Table 4.39 shows that the corresponding correlations are statistically significant in all energy channels except channel 4.

Table 4.39: Correlation Between Number of Pulses per Fit and Total Burst Count Fluences.

Energy Channel	r_s	Prob.
1	0.47	5.1×10^{-10}
2	0.50	1.3×10^{-12}
3	0.51	2.1×10^{-12}
4	0.36	0.0021

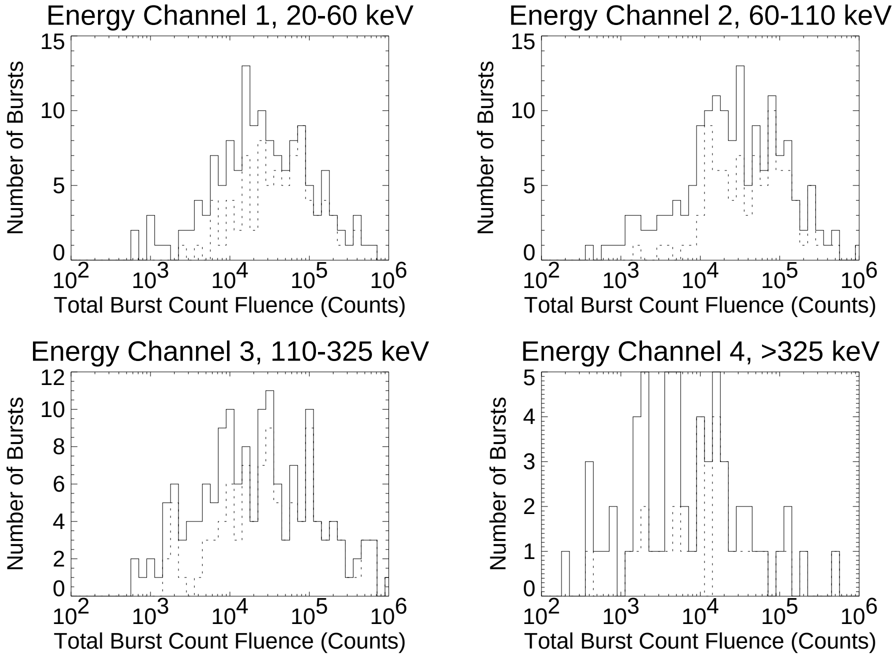

Figure 4.30: Total burst count fluences by energy channel. Dashed lines are multiple-pulse fits.

4.12 Finding Correlations Between Pulse Characteristics

Correlations between different characteristics of pulses, or the lack thereof, may reveal much about gamma-ray bursts that the distributions of the individual characteristics cannot. Some correlations may arise from intrinsic properties of the burst sources, or bursters, while others may result from the differing distances from the bursters to the Earth. In order to distinguish between the two kinds of effects, it is useful to examine correlations of pulse characteristics both between different bursts, and between pulses within individual bursts.

It is simplest to find correlations between characteristics of all pulses, but such correlations would combine both kinds of effects, and the statistics would be weighted in favor of bursts containing more pulses. It is also possible to select a single pulse from each burst, and find correlations between the characteristics of these pulses in order to look for effects arising from the locations of burst sources. However, if the correlations are taken using the single highest amplitude or highest fluence pulse from each burst, then they could still be affected by correlations of pulse characteristics within individual bursts. For example, if

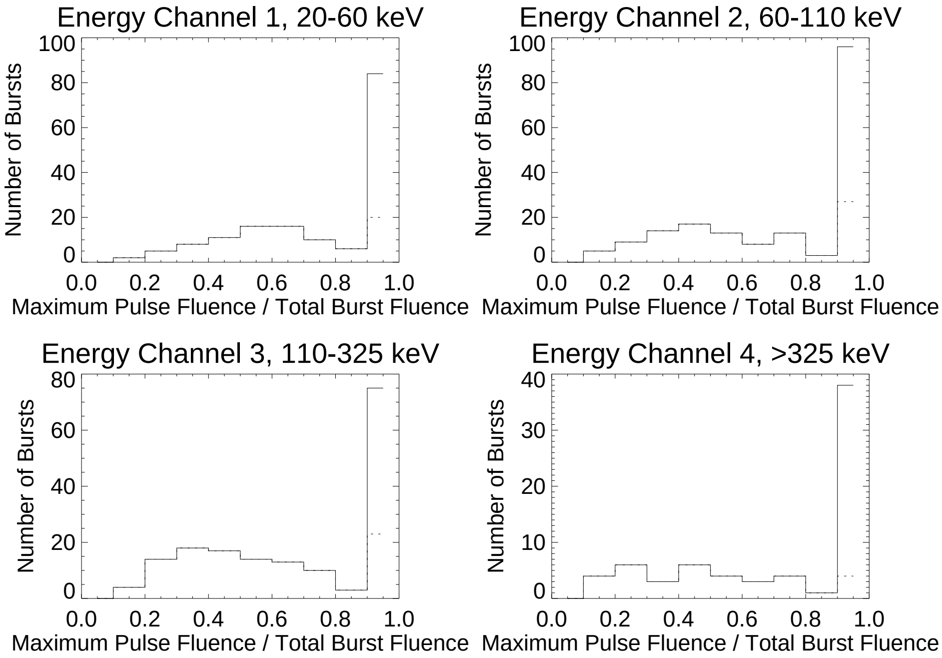

Figure 4.31: Fraction of burst count fluence contained in a single pulse, by energy channel. Dashed lines are multiple-pulse fits (only affects the last bin).

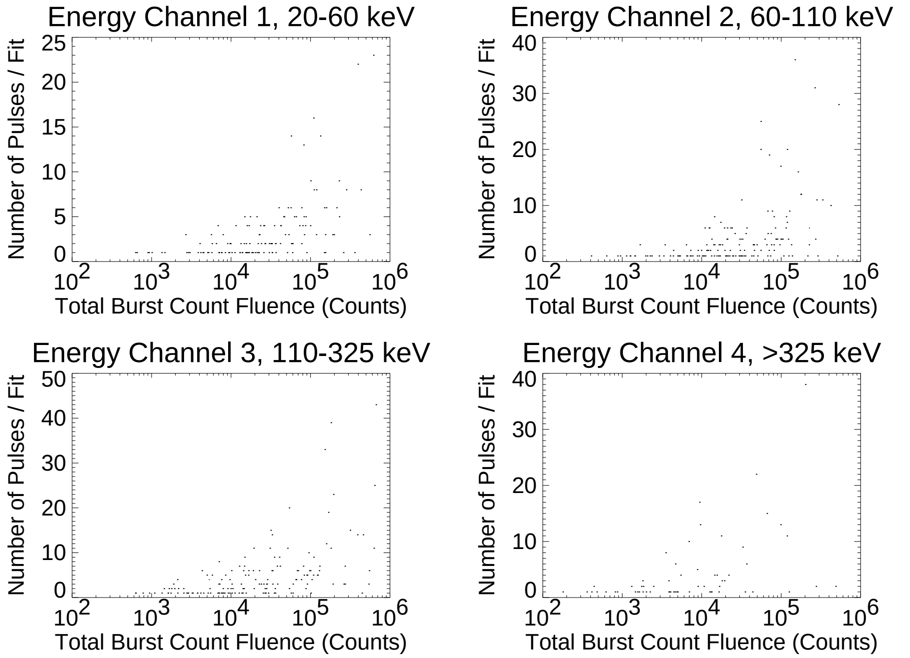

Figure 4.32: Number of pulses per fit versus total burst count fluences, by energy channel.

pulse amplitudes and durations within individual bursts are correlated, but all bursts have an identical distribution of pulse amplitudes and durations, then if we select the single highest amplitude pulse from each burst, we would find a spurious correlation between highest pulse amplitude and duration between bursts.

One way to find correlations of pulse characteristics within individual bursts is to calculate a correlation coefficient for each burst and examine the distribution of the correlation coefficients, for example to see if the correlation coefficients were positive for a large majority of bursts. Various correlation coefficients are described in Appendix D, and the Spearman rank-order correlation coefficient r_s, given by Equation D.2, is used here. When using the Spearman rank-order correlation coefficient, the coefficients for the individual bursts are often not statistically significant because the number of pulses in each burst is not large, even though the coefficents for the different bursts may be mostly positive or mostly negative. We can test the hypothesis that there is no correlation because in the absence of any correlation, we would expect an equal number of bursts with positive correlations as with negative correlations, so the probability that the observed numbers of bursts with positive and negative correlations could occur by chance if there was no correlation is given by the binomial distribution. This is the method used here. This method ignores the strengths of the individual correlations, so it is more sensitive to a weak correlation that affects large numbers of bursts than it is to a strong correlation that affects only a small number of bursts.

Another possible way to look for correlations within individual bursts is to select the two highest amplitude or highest fluence pulses from each burst and directly compare the characteristics of interest for each burst to see if there is a positive or negative correlation for that burst. If there is no correlation, then the numbers of bursts with positive and negative correlations should also follow a binomial distribution.

Still another possible way to find correlations within bursts is to remove correlations of pulse characteristics between bursts by normalizing the attributes of the pulses in each burst to those of a single pulse in each burst, such as the highest amplitude pulse. It is then straightforward to look for correlations in the collection of normalized pulse attributes for all bursts. Unlike the previous methods, this method may yield correlations dominated by complex bursts containing large numbers of pulses.

Table 4.40: Correlations Between Pulse Amplitude Hardness Ratio and Pulse Width Within Bursts.

Energy Channels	% Pos. Corr.	Binom. Prob.
2 / 1	45/83 = 54%	0.44
3 / 2	50/95 = 53%	0.61
4 / 3	14/33 = 42%	0.38
All	109/211 = 52%	

We can investigate spectral characteristics with the pulse-fitting data by using the *hardness ratios* of individual pulses. The hardness ratio of a pulse between two specified energy channels is the ratio of the fluxes or fluences of the pulse between the two energy channels. Although the actual numerical values of the hardness ratios depend on the somewhat arbitrary boundaries of the energy channels, the values can be compared between different pulses, and between different bursts.

Table 4.40 shows the correlations between pulse amplitude hardness ratios and pulse widths within bursts. The pulse widths used are arithmetic means of the widths in the two adjacent energy channels that the hardness ratios are taken between, *e.g.* hardness ratios between channels 2 and 3 are compared with pulse widths averaged over channels 2 and 3. The table shows no significant tendency for longer or shorter duration pulses to have harder or softer spectra, measured using fluxes.

Table 4.41 shows the correlations between pulse amplitude hardness ratios and pulse amplitudes within bursts. The pulse amplitudes are summed over the two adjacent energy channels that the hardness ratios are taken between. It shows no statistically significant tendency for higher amplitude pulses to have harder or softer spectra, although slightly more bursts show a positive correlation (higher amplitude pulses are harder) than a negative correlation (higher amplitude pulses are softer.)

Table 4.42 shows the correlations between pulse count fluence hardness ratios and pulse widths within bursts. In channels 1 and 2, more bursts show negative correlations between the two quantities, *i.e.* longer duration pulses tend to have softer spectra, as measured using count fluences, and this effect may be statistically significant. There are no statistically effects between channels 2 and 3 or between channels 3 and 4.

Table 4.43 shows the correlations between pulse count fluence hardness ratios and pulse

Table 4.41: Correlations Between Pulse Amplitude Hardness Ratio and Pulse Amplitude Within Bursts.

Energy Channels	% Pos. Corr.	Binom. Prob.
2 / 1	44.5/83 = 54%	0.51
3 / 2	49/95 = 52%	0.76
4 / 3	20.5/33 = 62%	0.16
All	114/211 = 54%	

Table 4.42: Correlations Between Pulse Count Fluence Hardness Ratio and Pulse Width Within Bursts.

Energy Channels	% Neg. Corr.	Binom. Prob.
2 / 1	52.5/83 = 63%	0.016
3 / 2	47.5/95 = 50%	1.0
4 / 3	18.5/33 = 56%	0.49
All	118.5/211 = 56%	

count fluences within bursts. The pulse count fluences are summed over the two adjacent energy channels that the hardness ratios are taken between. In channels 1 and 2, more bursts show negative correlations, *i.e.* higher fluence pulses tend to have softer spectra, but again, this effect appears weak, and there is no significant effect in the other pairs of energy channels.

4.13 Time Evolution of Pulse Characteristics Within Bursts

One class of correlations between pulse characteristics within bursts are those between the pulse peak time and other pulse characteristics. These indicate whether certain pulse characteristics tend to evolve in a particular way during the course of a burst, *e.g.* if pulse amplitudes tend to increase or decrease, and may be useful for constraining possible physical models of burst sources. A possible variation of the last method described in the previous section is as follows: We divide the pulses in each burst into those that occur before the highest amplitude pulse and those that occur after the highest amplitude pulse,

Table 4.43: Correlations Between Pulse Count Fluence Hardness Ratio and Pulse Count Fluence Within Bursts.

Energy Channels	% Neg. Corr.	Binom. Prob.
2 / 1	51.5/83 = 62%	0.028
3 / 2	47/95 = 49%	0.49
4 / 3	20/33 = 66%	0.61
All	118.5/211 = 56%	

combine each of the two populations among all bursts, and compare the characteristics of the two populations. Again, I have used the first method described in the previous section, calculating the Spearman rank-order correlation coefficients for the individual bursts, and testing the observed numbers of bursts with positive and negative correlations using the binomial distribution.

Table 4.44 shows the number of fits in each channel where there is a negative correlation between pulse amplitude and peak time. Fits for which the calculated Spearman rank-order correlation coefficient was 0, indicating no correlation, were counted as half for decreasing and half for increasing in order to calculate, using the binomial distribution, the probability of this occurring randomly if pulse amplitudes within bursts are equally likely to increase as to decrease with time. The probability was not calculated for all energy channels combined, because fits to the same burst in different energy channels cannot be considered independent, so the binomial distribution cannot be used. In all energy channels except channel 1, pulse amplitudes are more likely to decrease with time than increase with time within bursts. However, this effect is not statistically significant, except possibly in energy channel 4. If such an effect existed, it could be an intrinsic property of bursters, or it could also be a selection effect of the BATSE trigger criteria, which favors fast-rising bursts.[69]

Table 4.45 shows that the pulse asymmetry ratios tend to decrease with time during bursts, except in energy channel 4. This effect appears to be statistically significant in channel 3, and possibly channels 1 and 2.

Examining separately the correlations between pulse rise time (See Table 4.46) or pulse decay time (See Table 4.47) and pulse peak time within bursts, we find that pulse rise times tend to become shorter during bursts, while pulse decay times tend to become longer during bursts. However, the statistical significance of these effects is weaker than for the

Table 4.44: Correlations Between Pulse Amplitude and Peak Time Within Bursts.

Energy Channel	% Decreasing	Binom. Prob.
1	43.5/94 = 46%	0.47
2	59/109 = 54%	0.39
3	65.5/116 = 55%	0.16
4	23/35 = 66%	0.063
All	163/354 = 54%	

Table 4.45: Correlations Between Pulse Asymmetry Ratio and Peak Time Within Bursts.

Energy Channel	% Decreasing	Binom. Prob.
1	61.5/94 = 66%	0.0028
2	66.5/109 = 61%	0.022
3	81/116 = 70%	1.9×10^{-5}
4	16/35 = 45%	0.61
All	225/354 = 64%	

Table 4.46: Correlations Between Pulse Rise Time and Peak Time Within Bursts.

Energy Channel	% Decreasing	Binom. Prob.
1	60/94 = 64%	0.0073
2	61.5/109 = 56%	0.18
3	72.5/116 = 63%	0.0071
4	18.5/35 = 53%	0.74
All	212.5/354 = 60%	

Table 4.47: Correlations Between Pulse Decay Time and Peak Time Within Bursts.

Energy Channel	% Increasing	Binom. Prob.
1	59/94 = 63%	0.0067
2	61/109 = 63%	0.013
3	68/116 = 56%	0.063
4	15/35 = 43%	0.40
All	203/354 = 57%	

correlations between pulse asymmetry ratio and pulse peak time. These effects may be artifacts of the fitting procedure that arise because the earliest pulse in a burst will have little overlap with other pulses on its rising slope (only with exponentially smaller rising slopes of pulses that peak later), and the last pulse in a burst will have little overlap with other pulses on its decaying slope. They are unlikely to result from selection effects of the BATSE trigger criteria, which should select for shorter rise times in the first pulse, and have no bias for rise times of subsequent pulses, or for decay times of any pulses.

Energy channel 4 appears to show a tendency for pulse widths to become shorter with time during bursts (See Table 4.48), but this result is probably not statistically significant. The other energy channels show a similar tendency, but the effect is clearly statistically insignificant in these energy channels. This result is relevant to external shock models of gamma-ray burst production, which will be discussed in Section 4.14. Comparing this with the correlations described for the rise times and decay times taken separately, we see that the decrease in rise times is nearly balanced by the increase in decay times, with the decreasing

Table 4.48: Correlations Between Pulse Width and Peak Time Within Bursts.

Energy Channel	% Decreasing	Binom. Prob.
1	$47.5/94 = 51\%$	0.92
2	$60/109 = 55\%$	0.29
3	$64/116 = 55\%$	0.27
4	$23.5/35 = 67\%$	0.043
All	$195/354 = 55\%$	

Table 4.49: Correlations Between the Peakedness Parameter ν and Peak Time Within Bursts.

Energy Channel	% Decreasing	Binom. Prob.
1	$53/94 = 56\%$	0.22
2	$60/109 = 55\%$	0.29
3	$68.5/116 = 59\%$	0.051
4	$22.5/35 = 64\%$	0.091
All	$204/354 = 58\%$	

rise times possibly a slightly stronger effect than the increasing decay times. Ramirez-Ruiz and Fenimore [70, 71] have found no evidence that pulse widths increase or decrease with time when fitting a power-law time dependence, using a small sample of complex bursts selected from the bright, long bursts fitted by Norris, *et al.* [22]

Table 4.49 shows that the peakedness parameter ν is more likely to decrease with time within bursts than to increase with time. This effect is statistically insignificant in energy channels 1 and 2, but may be statistically significant in channels 3 and 4.

Energy channel 3 shows a tendency for pulse count fluences to decrease during the course of a burst that may be statistically significant. (See Table 4.50.) The other energy channels show no statistically significant effects.

It has been previously reported that bursts tend to show a hard-to-soft spectral evolution, which we can test by seeing how the hardness ratios of individual pulses vary with time. Table 4.51 shows that the pulse amplitude hardness ratios have a slight tendency to

Table 4.50: Correlations Between Pulse Count Fluence and Peak Time Within Bursts.

Energy Channel	% Decreasing	Binom. Prob.
1	40.5/94 = 43%	0.18
2	56.5/109 = 52%	0.70
3	73/116 = 63%	0.0053
4	21/35 = 60%	0.24
All	191/354 = 54%	

Table 4.51: Correlations Between Pulse Amplitude Hardness Ratio and Peak Time Within Bursts.

Energy Channels	% Decreasing	Binom. Prob.
2 / 1	46.5/83 = 56%	0.27
3 / 2	54.5/95 = 57%	0.15
4 / 3	18.5/33 = 56%	0.48
All	119.5/211 = 57%	

decrease with time during bursts between all three pairs of adjacent energy channels. However, with the numbers of available bursts that are composed of multiple pulses in adjacent energy channels, this tendency is statistically insignificant.

When we consider the time evolution of the pulse count fluence hardness ratios within bursts, we find no tendency for the hardness ratio of energy channel 2 to channel 1 to increase or decrease, a possibly significant tendency for the hardness ratio of energy channel 3 to 2 to decrease with time, and a statistically insignificant tendency for the hardness ratio of channel 4 to 3 to increase with time. (See Table 4.52.)

4.14 Examples of Constraints on Models of Gamma-Ray Bursts

The characteristics of bursts and their constituent pulses can be used to constrain possible models of gamma-ray bursts. Here are some simple examples of such constraints:

A simplistic way to try to explain the great variety of GRB time profiles is that the

Table 4.52: Correlations Between Pulse Count Fluence Hardness Ratio and Peak Time Within Bursts.

Energy Channels	% Decreasing	Binom. Prob.
2 / 1	42.5/83 = 51%	0.83
3 / 2	61/95 = 64%	0.0056
4 / 3	13/33 = 39%	0.22
All	116.5/211 = 55%	

gamma-ray emission from the source is beamed, with the beam direction changing chaotically, so that a pulse is observed whenever the beam points towards the Earth. Examination of the actual GRB time profiles reveals several shortcomings of such a model. One is that the asymmetries of pulses requires that the characteristics of a beam must vary in the direction that it is traveling in, so that pulse rise times will be shorter than decay times. Also, the time lags between energy channels require that a beam peak at higher energies forward of where it peaks at lower energies, so that pulses peak earlier at higher energies. The beams would also have to be narrower at higher energies, because pulses are, but this can be accommodated. The greatest difficulty is probably with overlapping pulses, especially in bursts with narrow spikes overlaid on top of a long emission. It is very difficult to explain such bursts without greatly complicating such a model, for example, with multiple beams that are all changing direction.

Some models use mechanisms for producing burst time profiles containing multiple pulse that require all of the pulses within a single burst to have similar shapes, because all of the pulses originate from a single explosion.[72] In the context of the pulse model used here, this requires that the pulse asymmetry ratio σ_r/σ_d and the peakedness parameter ν be approximately the same for all pulses within a burst. Some models also require that the pulse durations, or widths, for all pulses within a burst to be approximately the same, leaving the pulse amplitude and pulse peak time as the only characteristics that can vary between pulses within a burst. Since all of these pulse characteristics often vary significantly between pulses within individual bursts, such models cannot account for the full variety of time profiles observed.

According to Ramirez-Ruiz and Fenimore [70], in external shock models of GRB production, in which an expanding relativistic shell from a central source produces gamma-rays when it interacts with the external medium, pulse durations should increase over the course of a burst. They fitted power laws for the time evolution of pulse widths in the 28 most complex bursts fitted by Norris *et al.* [22] and found no evidence that pulse durations tend to increase with time. For the much larger sample of bursts examined here, I have also found that more bursts have pulse durations that decrease with time than increase with time, although the result appears to be statistically insignificant with the test that I used. This supports the argument of Ramirez-Ruiz and Fenimore favoring internal shock models, where the observed time variation of GRBs are produced in the central engine, over external shock models.

Chapter 5

Time Dilation

For gamma-ray bursts originating at cosmological distances, all timescales observed in more distant bursts will be lengthened compared to those in nearer bursts as a result of cosmological time dilation.[73, 74] The time dilation factor is $1 + z$, where z is the cosmological redshift parameter for the burst source, or burster. Except for a handful of bursts for which counterparts have been discovered in optical and radio frequencies, there is no way to determine the distances to the bursters. However, more distant bursts should tend to appear dimmer than nearer bursts, and therefore dimmer bursts should have longer timescales if bursters are at cosmological distances. This assumes that the distributions of intrinsic luminosities and timescales of bursts haven't changed during the history of the universe, *i.e.*, that bursters haven't evolved with time. Measuring the distances to bursters requires finding a *standard candle*, a quantity that is approximately equal for all bursters, so that the observed variation results from the different distances to bursters rather than to intrinsic differences between the bursters. Measuring the time dilation factor requires finding a standard timescale of bursts. Given the great diversity in burst time profiles, it seems unlikely that any particular timescale is approximately the same in all bursts, so we expect to find time dilation as a statistical effect, rather than for individual bursts.

The apparent brightnesses of bursts are generally measured using either peak fluxes, which attempt to give the instantaneous intensity of bursts when they peak, or fluences, which attempt to measure the total output of bursts integrated over their entire durations. The brightness measures can also be divided another way, into photon measures and energy measures. This gives a total of four different measures of the apparent brightnesses of bursts. Energy fluxes are not commonly used, or even calculated, for gamma-ray bursts. The BATSE burst catalogs give peak photon fluxes and total energy fluences for bursts. The pulse-fitting data presented here can be used to determine count fluxes and count fluences.

It is useful to know how the various measures of brightness, as well as other quantities, vary for objects at cosmological distances. Table 5.1 shows how various apparent quantities scale with luminosity distance d_L and redshift z. The luminosity distance is defined so that the apparent energy flux scales as $1/d_L^2$. It is given in terms of z, the Hubble constant H_0, and the matter density Ω_M and cosmological constant density Ω_Λ by [75]

$$d_L = \frac{c(1+z)}{H_0\sqrt{|\kappa|}} S\left(\sqrt{|\kappa|}\int_0^z \left[(1+z')^2(1+\Omega_M z') - z'(2+z')\Omega_\Lambda\right]^{-\frac{1}{2}} dz'\right) \tag{5.1}$$

where the function S is sinh for $\kappa \geq 0$ and sin for $\kappa \leq 0$. In the absence of a cosmological constant ($\Omega_\Lambda = 0$), this becomes

$$d_L = \frac{c}{H_0 q_0^2}[1 - q_0 + q_0 z + (q_0 - 1)\sqrt{2q_0 z + 1}] \tag{5.2}$$

for $q_0 \neq 0$ and

$$d_L = \frac{c}{2H_0 q_0^2} z(2+z) \tag{5.3}$$

for $q_0 = 0$, where q_0 is the deceleration parameter, given by $q_0 = \Omega_M/2$.[76, 77, 78] For $z \ll 1$, we see that $d_L \approx \frac{cz}{H_0}$, while for $z \gg 1$, $d_L \approx \frac{cz}{H_0 q_0}$ for $q_0 \neq 0$ and $d_L \approx \frac{cz^2}{2H_0}$ for $q_0 = 0$. Figures 5.1 and 5.2 show how apparent photon flux and photon fluence vary with the time dilation factor $1+z$ for a case based on recent measurements of the cosmological parameters using high-redshift supernovae and the cosmic microwave background, $\Omega_\Lambda = 0.76$ and $\Omega_M = 0.24$ [79, 80], and also for the cases $\Omega_\Lambda = 0$ and $q_0 = 0, 1/2, 1$, corresponding respectively to $\Omega_M = 0$, 1, and 2, respectively. In all $\Omega_\Lambda = 0$ cosmologies, the luminosity distance always varies more steeply than the time dilation factor $1+z$, so that the observed photon fluxes of sources must fall more rapidly than $1/(1+z)$ due to cosmological effects, while the apparent photon fluences must always decrease, or asymptotically approach a constant, as z increases. In the presence of a non-zero cosmological constant, the luminosity distance cannot be expressed in closed form, but we can see from the figures that the behavior is similar to the cases with zero cosmological constant.

Consider a situation where we have transient sources that are identical at their sources, so that all observed variation in their characteristics are a result of their differing distances.

Table 5.1: Dependence of Observable Quantities on Luminosity Distance d_{L} and Redshift Parameter z.

Quantity	Scaling
Photon Energy	$\frac{1}{1+z}$
All Timescales	$1+z$
Energy Flux	$\frac{1}{d_{\mathrm{L}}^2}$
Photon Flux	$\frac{1+z}{d_{\mathrm{L}}^2}$
Energy Fluence	$\frac{1+z}{d_{\mathrm{L}}^2}$
Photon Fluence	$\frac{(1+z)^2}{d_{\mathrm{L}}^2}$

Then for $\Lambda = 0$, the apparent timescales, fluxes, and fluences would all fall exactly on the curves shown in Figures 5.1 and 5.2. The peak photon fluxes would span a broader range of values than the timescales.

Given the great variety of gamma-ray burst time profiles, it is clear that bursters are not identical, and that there is a large amount of intrinsic variation in their characteristics. Observed correlations between luminosity measures and timescale measures for bursts could result from a combination of cosmological effects, correlations between the absolute luminosities and timescales of bursters, as well as selection effects of the observations.

Most previous work on the evidence for time dilation in burst time profiles has selected two or three brightness classes of bursts and compared the timescales between these classes. Here I will try to relate apparent burst luminosities and observed timescales using power laws. Although cosmological models generally predict more complex relationships than a simple power law, it would be fruitless to attempt to fit anything more complex than a power law using the pulse-fitting data, which appears to have a large intrinsic scatter.

5.1 Peak Luminosity as a Standard Candle

The peak luminosities of bursts are most commonly assumed to be a standard candle. This corresponds to the amplitudes of the constituent pulses in bursts. It has previously been found that higher amplitude pulses have shorter durations (are narrower),[81, 54, 82], but it has also been noted that there could be an intrinsic property of bursters that causes

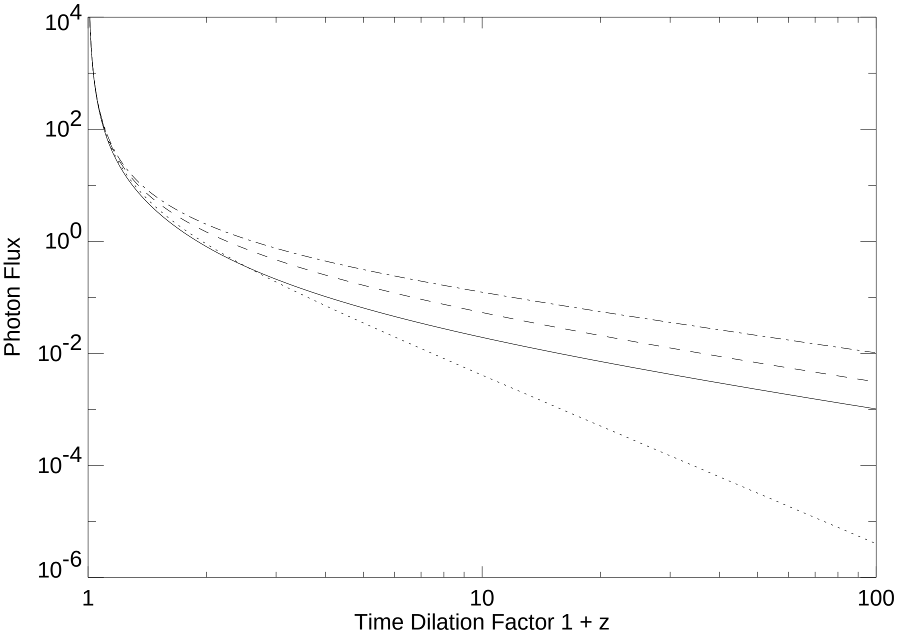

Figure 5.1: Apparent photon flux versus time dilation for $\Omega_\Lambda = 0.76$ and $\Omega_M = 0.24$ (solid line), and for $\Omega_\Lambda = 0$ and $q_0 = 0$ (dotted line), $q_0 = 1/2$ (dashed line) and $q_0 = 1$ (dash-dotted line).

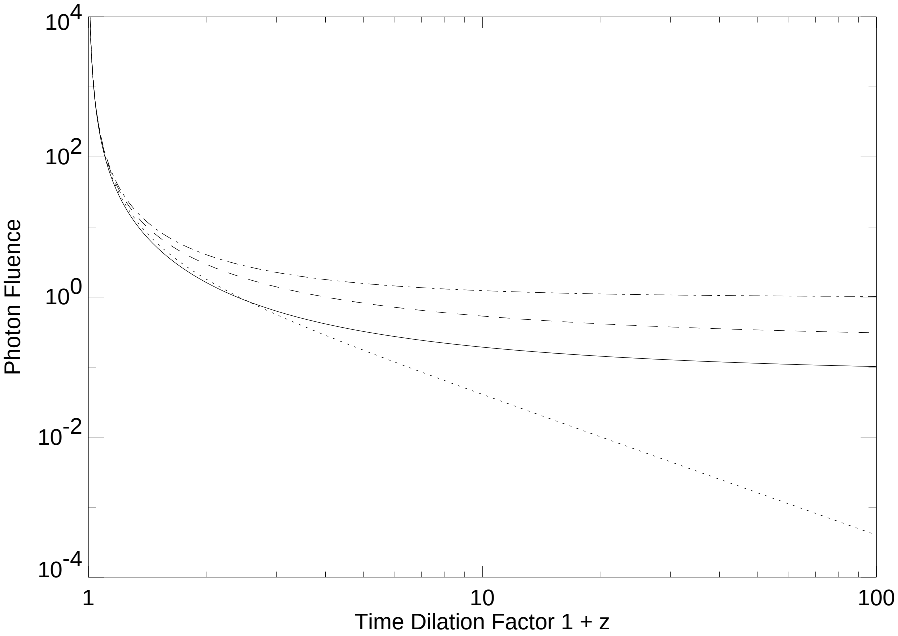

Figure 5.2: Apparent photon fluence versus time dilation for $\Omega_\Lambda = 0.76$ and $\Omega_M = 0.24$ (solid line), and for $\Omega_\Lambda = 0$ and $q_0 = 0$ (dotted line), $q_0 = 1/2$ (dashed line) and $q_0 = 1$ (dash-dotted line).

Table 5.2: Correlation Between Pulse Amplitude and Pulse Width (FWHM), All Pulses in All Fits Combined.

Energy Channel	r_s	Prob.	α
1	-0.53	9.9×10^{-39}	-0.73 ± 0.03
2	-0.49	0	-0.79 ± 0.02
3	-0.44	1.3×10^{-42}	-0.83 ± 0.02
4	-0.52	2.4×10^{-20}	-0.75 ± 0.03

higher amplitude pulses to be shorter, independent of the distance to the bursters [83]. It is also possible that this correlation is a result of both effects. A potential problem with using peak flux as a distance measure for bursts observed by BATSE is that data binned to 64 ms have been typically used, so that the peak fluxes of bursts with sharp spikes may be underestimated.[66] This should be less of a problem with the variable time resolution TTS data, where the time resolution is inversely proportional to the count rate and every spill represents the same number of counts. The pulse-fitting data shown in Figure 5.3 clearly shows that higher amplitude pulses tend to be narrower, or have shorter durations. Table 5.2 gives the Spearman rank-order correlation coefficients, which show that pulse amplitudes and pulse widths are inversely correlated in all energy channels. The table also gives fitted power laws for pulse amplitude as a function of pulse width. These were obtained by applying the ordinary least squares (OLS) bisector linear regression algorithm, which is described in Section D.3, to the logarithms of the pulse amplitudes and pulse widths.

Since none of the linear regression algorithms described in Section D.3 are robust algorithms, unlike the Spearman rank-order correlation coefficient, and are sensitive to outliers, pulses with fitted widths shorter than 1 ms or longer than 1000 seconds were removed when calculating all of the power law fits described in this chapter that involve pulse widths. The plots shown here have been truncated to make it easier to see the bulk of the distribution, but when plotting the complete sample of pulses, it is visually apparent that the extremely short and extremely long pulses that have been removed are outside the main part of the distribution. As noted before, the pulse amplitudes do not appear to have a problem with outliers.

Suppose that *within* multiple-pulse bursts, higher amplitude pulses tended to be narrower than lower amplitude pulses within the same bursts, but that there was no correlation

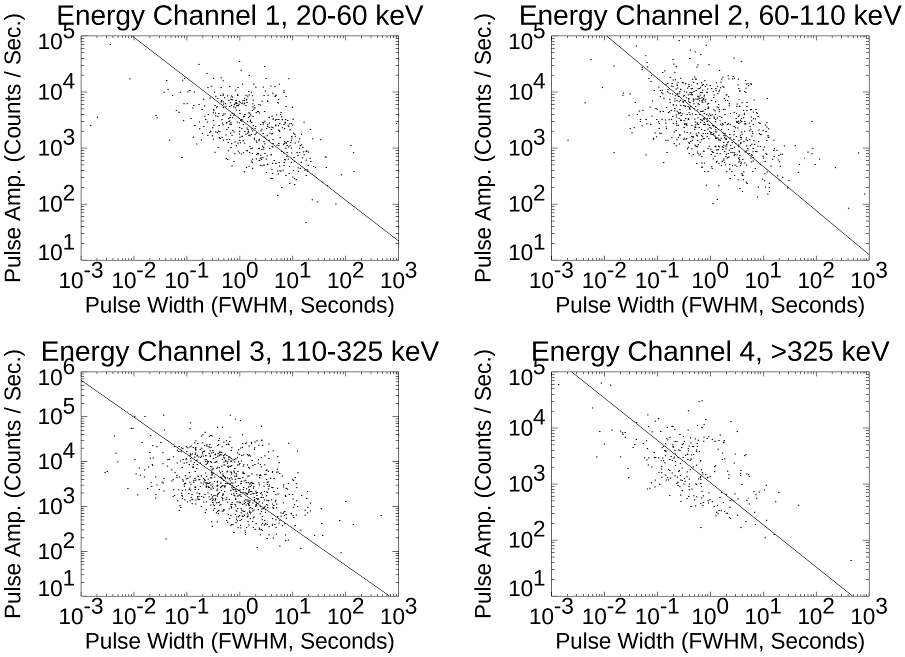

Figure 5.3: Pulse amplitude versus pulse width (FWHM), all pulses in all fits combined.

between pulse amplitude and pulse width *between* different bursts. This obviously couldn't result from cosmological time dilation, but would have to be caused by some characteristic of the bursters themselves, or by selection effects. In such a case, we would also see an inverse correlation when using all pulses from all bursts combined.

Therefore, it is more reasonable to compare the peak fluxes in each burst, corresponding to the amplitudes of the highest amplitude pulse in each burst, with the widths of the same pulses. This also shows a strong inverse correlation between peak pulse amplitude and pulse width. (See Figure 5.4 and Table 5.3.)

It is also useful to compare pulse widths and amplitudes of pulses within bursts, because correlations between pulse characteristics within bursts cannot be affected by the distances to the bursters, but are likely to be affected by the same selection effects, and possibly the same intrinsic properties of the bursters, that affect correlations between pulse characteristics between different bursts. This comparison may help to separate distance effects from other effects. The results are shown in Table 5.4, which gives the numbers and fractions of fits that show inverse correlations as determined from the Spearman coefficients, and the probabilities that this would occur by chance if there was no actual correlation, using the

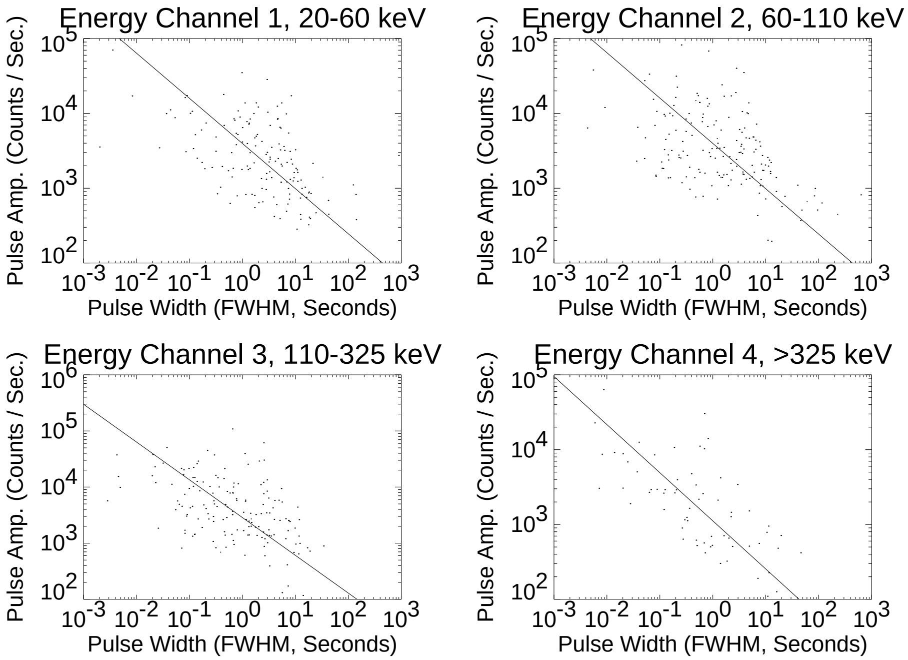

Figure 5.4: Pulse amplitude versus pulse width (FWHM), highest amplitude pulse in each fit.

Table 5.3: Correlation Between Pulse Amplitude and Pulse Width (FWHM), Highest Amplitude Pulse in Each Fit.

Energy Channel	r_s	Prob.	α
1	-0.57	9.1×10^{-15}	-0.60 ± 0.05
2	-0.52	5.8×10^{-14}	-0.61 ± 0.04
3	-0.51	1.1×10^{-12}	-0.67 ± 0.05
4	-0.71	7.1×10^{-12}	-0.64 ± 0.05

Table 5.4: Correlations Between Pulse Amplitude and Pulse Width Within Bursts.

Energy Channel	% Neg. Corr.	Binom. Prob.	$\alpha < -1$	$-1 < \alpha < 0$	$0 < \alpha < 1$	$\alpha > 1$	Med. α
1	$65/94 = 69\%$	0.00020	21	42	22	9	-0.37
2	$74/109 = 68\%$	0.00019	21	58	21	9	-0.43
3	$82.5/116 = 71\%$	5.4×10^{-6}	17	63	21	15	-0.46
4	$26.5/35 = 76\%$	0.0023	3	26	5	1	-0.55
All	$248/354 = 70\%$		62	189	69	34	-0.46

binomial distribution. It also gives the numbers of power-law fits to the pulse amplitudes as a function of pulse width (linear regression fits to the logarithms) with exponents (slopes), which we denote as α, with $\alpha < -1$, $-1 < \alpha < 0$, $0 < \alpha < 1$, and $\alpha > 1$, using any of the three methods OLS bisector, orthogonal regression, or reduced major-axis. (All three symmetric linear regression methods give the same numbers of fits with slopes in each octant of the plane.) The last column gives the median power law from the OLS bisector method. For all energy channels, a significant majority of fits show inverse correlations between pulse widths and pulse amplitudes *within* bursts. When we examine the bursts for which the rank correlations have the greatest statistical significance, we find that nearly all of these show inverse correlations between pulse widths and pulse amplitudes; in the bursts where the correlations are positive, the correlations also tend to be less statistically significant. Pulse amplitudes most often vary as a small negative power of the pulse width. The power laws are significantly different from those relating pulse amplitude to pulse width for the highest amplitude pulses in each burst.[84] Ramirez-Ruiz and Fenimore [71] have compared pulse width with pulse amplitude within bursts for the sample of 28 complex bursts fitted by Norris *et al.* [22], and have also found that higher amplitude pulses tend to have shorter durations. They found the anticorrelation to be consistent with internal shock models of GRBs.

Cosmological time dilation must affect all timescales within bursts, not only pulse widths. Also, all gamma-rays detected from bursts at cosmological distances will be observed at lower energies than they were produced with at the source due to cosmological redshift. Thus, for dimmer, hence more distant, bursts observed by BATSE, the observed

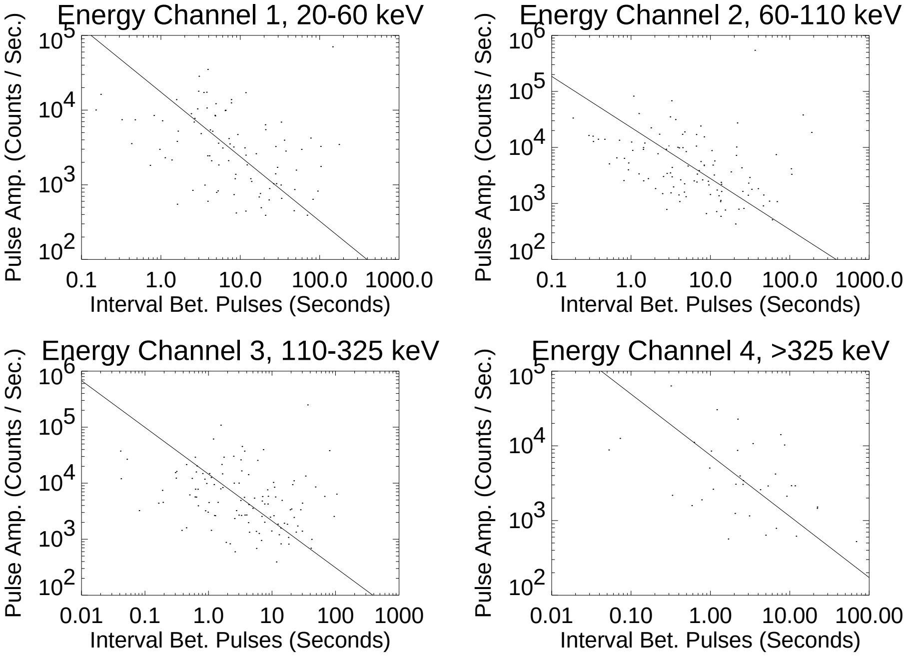

Figure 5.5: Highest pulse amplitude versus interval between two highest pulses in each fit.

gamma-rays were originally produced at higher energies but had redshifted to lower energies when they were detected. Since pulses tend to be narrower at higher energies (See Section 4.7.), this would reduce the *apparent* time dilation of pulse widths.

We have seen earlier that the intervals between the peak times of the two highest amplitude pulses in each burst don't appear to increase or decrease with energy, so that cosmological redshift of energies shouldn't affect these intervals. These intervals also show a significant inverse correlation with the amplitudes of the highest amplitude pulse in the corresponding bursts, so they are shorter for brighter bursts. (See Figure 5.5 and Table 5.5.) Since these intervals are the differences between the peak times of the two highest pulses in each burst, and the peak times don't have any unreasonable outliers in their distribution, there is no reason to remove any of the intervals as outliers. An early study of time dilation in intervals between pulses found inconsistent results [85], but a number of other studies have found evidence of time dilation.[86, 87, 88]

We can also compare pulse amplitudes with time intervals between pulses within bursts as follows: For each burst time profile consisting of three or more pulses, order the individual pulses by decreasing pulse amplitude. Then take the absolute values of the intervals between

Table 5.5: Correlation Between Highest Pulse Amplitude and Interval Between Two Highest Pulses in Each Fit.

Energy Channel	r_s	Prob.	α
1	-0.42	2.7×10^{-5}	-0.86 ± 0.06
2	-0.42	7.2×10^{-6}	-0.91 ± 0.06
3	-0.34	1.8×10^{-4}	-0.83 ± 0.06
4	-0.40	0.017	-0.82 ± 0.11

Table 5.6: Correlations Between Pulse Amplitude and Intervals Between Pulses Within Bursts.

Energy Channel	% Neg. Corr.	Binom. Prob.	$\alpha < -1$	$-1 < \alpha < 0$	$0 < \alpha < 1$	$\alpha > 1$	Med. α
1	42/62 = 68%	0.0052	5	38	14	5	-0.47
2	54/89 = 61%	0.044	9	49	26	5	-0.44
3	55/95 = 58%	0.12	4	51	34	6	-0.32
4	17.5/24 = 73%	0.064	2	15	5	2	-0.48
All	168.5/270 = 62%		20	153	79	18	-0.44

each pulse and the pulse with the next lower amplitude, match them with the amplitudes of the corresponding pulses (the higher amplitude pulse of each pair), and apply the same methods used for comparing pulse amplitudes and pulse widths within bursts. The results are shown in Table 5.6. They show inverse correlations between pulse amplitudes and intervals between pulses within bursts in all energy channels, but these are statistically insignificant in all energy channels except possibly channel 1. The fitted power laws are significantly different from those obtained by comparing the highest pulse amplitude in each fit with the time interval between the two highest pulses in each fit. However, these power laws are similar to those obtained by comparing pulse amplitudes with pulse widths within bursts, *i.e.*, pulse widths and intervals between pulses appear to vary the same with with pulse amplitudes within bursts.

The correlation between the highest pulse amplitude and the width of the same pulse in each burst gives a variation that doesn't appear to agree with the expected effects of cosmological time dilation alone. For a given variation in the highest pulse amplitude, the corresponding variation in pulse width is too great to account for with only cosmological effects. We have also seen that within individual bursts, higher amplitude pulses have a strong tendency to be narrower, which must result from intrinsic properties of the bursters themselves, or from selection effects in the pulse-fitting procedure. It seems likely that the observed correlation between the highest pulse amplitude and the width of the highest pulses in each burst results from a combination of cosmological and non-cosmological effects.

One of the possible intrinsic effects that could contribute to the inverse correlations of pulse widths with pulse amplitudes is that the total energy in a burst, or within individual pulses, might tend to fall within a limited range, or might have an upper limit. This would be the case if, for example, the fluence of a burst were a better measure of distance than the peak flux.

On the other hand, the correlation between the highest pulse amplitude and the time interval between the peaks of the two highest pulses in each burst gives a variation that may be consistent with the expected results of cosmological time dilation alone. It seems likely that this correlation is less affected by intrinsic properties of bursters or by selection effects than the correlation between the highest pulse amplitude and the width of the same pulse in each burst. For example, if the range of burst fluences or individual pulse fluences were limited by the production mechanism, or by selection effects, this would be far less likely to affect intervals between pulses than to affect pulse widths.

5.2 Integrated Luminosity as a Standard Candle

Petrosian and Lee [89] and Lloyd and Petrosian [90] have suggested that the integrated luminosities, measured using either energies or photons, of bursts are likely to be better standard candles than their peak luminosities. This would be the case if the total energy output of bursters fall in a narrow range of values, and much of the variation in flux results from the broad range of burst durations. Petrosian and Lee [91, 66] have also found that the energy fluences of bursts and their durations show a positive correlation, which is the opposite of what cosmological time dilation should cause. We shall see that the count fluences of bursts and pulse widths show a positive correlation, while the count fluences of bursts and time intervals between pulses show no correlation, and neither of these effects can arise from cosmological effects

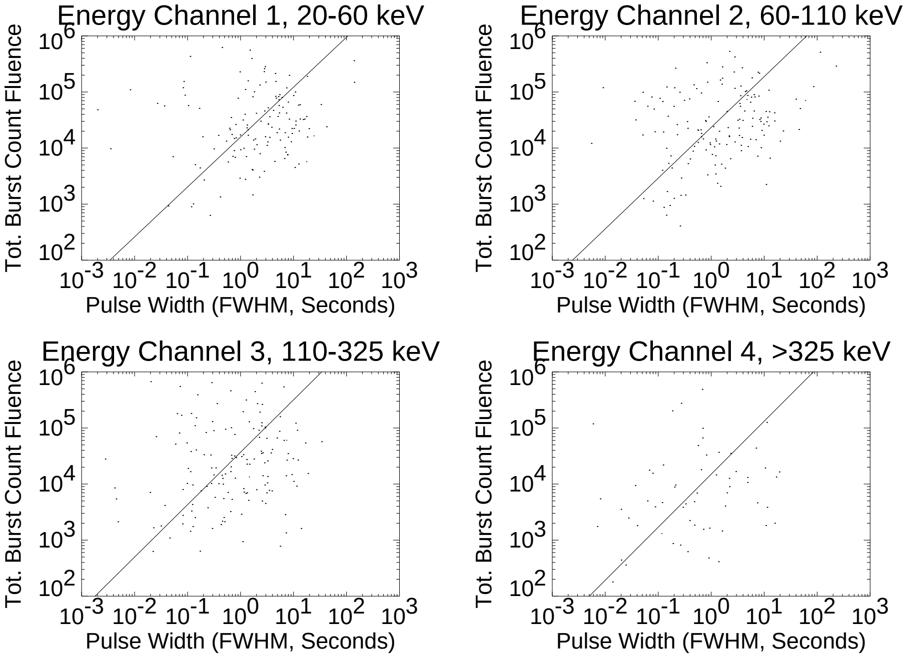

Figure 5.6: Total count fluence versus pulse width (FWHM) of highest amplitude pulse in each fit.

Comparison of the pulse widths of the highest amplitude pulses in each fit with the total count fluences of each fit shows positive correlations that appear to be significant in all energy channels except perhaps in channel 3. (See Figure 5.6 and Table 5.7.) In all of the power law fits in this chapter involving total burst count fluences, in addition to removing extremely short and long duration pulses, fits for which the total count fluence was less than 100 counts or greater than 10^7 counts were removed because the untruncated plots showed that they were clearly outside the main part of the distribution.

If we compare instead the pulse widths and pulse count fluences of the highest amplitude pulses in each fit, we find stronger positive correlations, but smaller power laws, so that the individual pulse count fluences increase more slowly than the total burst count fluence as we increase the pulse width. (See Figure 5.7 and Table 5.8.) The truncations used when fitting power laws involving pulse count fluences were a minimum of 10 counts and maximum of 10^6 counts in an individual pulse, which are lower than the limits used for total count fluence in a burst. Again, the limits were chosen because the untruncated plots showed that these were outside the main part of the distribution.

Table 5.7: Correlation Between Total Count Fluence and Pulse Width (FWHM) of Highest Amplitude Pulse in Each Fit.

Energy Channel	r_s	Prob.	β
1	0.29	2.4×10^{-4}	0.89 ± 0.06
2	0.27	2.7×10^{-4}	0.91 ± 0.05
3	0.17	0.023	0.93 ± 0.04
4	0.33	5.8×10^{-3}	0.95 ± 0.05

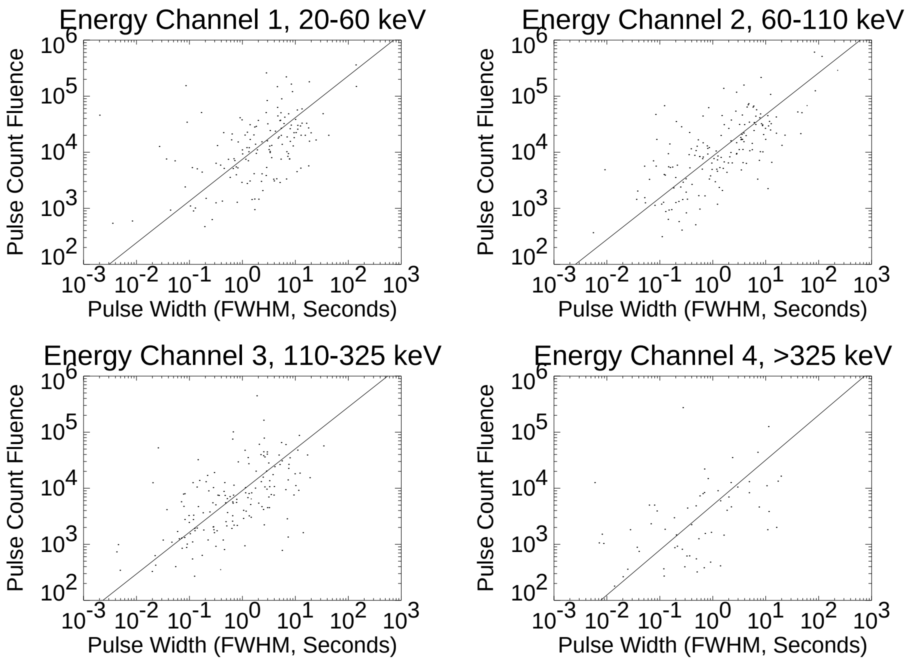

Figure 5.7: Pulse count fluence versus pulse width (FWHM) of highest amplitude pulse in each fit.

Table 5.8: Correlation Between Pulse Count Fluence and Pulse Width (FWHM) of Highest Amplitude Pulse in Each Fit.

Energy Channel	r_s	Prob.	β
1	0.56	1.3×10^{-14}	0.74 ± 0.06
2	0.69	3.0×10^{-26}	0.74 ± 0.05
3	0.62	2.2×10^{-19}	0.74 ± 0.05
4	0.63	5.4×10^{-9}	0.80 ± 0.08

Table 5.9: Correlation Between Pulse Count Fluence and Pulse Width (FWHM), All Pulses in All Fits Combined.

Energy Channel	r_s	Prob.	β
1	0.48	1.5×10^{-31}	0.88 ± 0.03
2	0.51	0	0.91 ± 0.03
3	0.49	0	0.93 ± 0.02
4	0.56	5.2×10^{-24}	0.93 ± 0.05

If we compare the pulse widths and pulse count fluences of all pulses in all fits combined, we find even stronger positive correlations, and the power laws are larger than for the pulse widths and pulse count fluences of the highest amplitude pulses in each fit. (See Figure 5.8 and Table 5.9.) The power laws are the same as for the pulse widths of the highest pulse in each fit and the total burst count fluences of each fit, but there is no apparent reason for this to occur.

Correlations between pulse width and pulse count fluence *within* bursts do not appear to have been studied before. A significant majority of fits in all energy channels show positive correlations between pulse width and pulse count fluence within individual bursts. (See Table 5.10.) Pulse count fluences most often vary as a large positive power of the pulse width. The reciprocal of the median of $1/\beta$, where we use β to denote the power law index, is shown because $|\beta| > 1$ for more bursts than $|\beta| < 1$, so that taking the median of the reciprocal of β is more appropriate.

The time interval between the two highest amplitude pulses in each fit also appears to increase as the total count fluence in the fit increases. (See Figure 5.9.) The two quantities

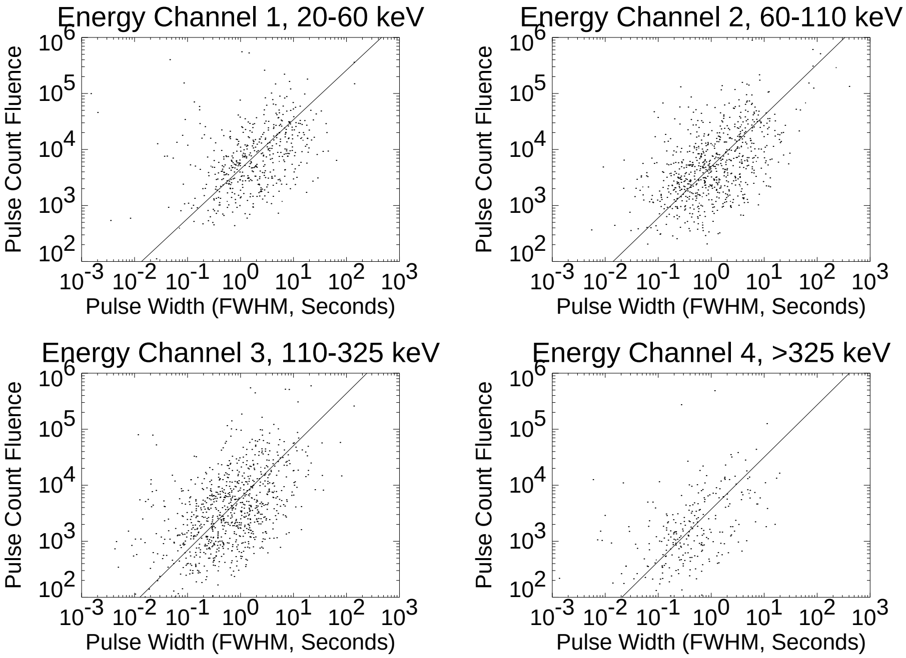

Figure 5.8: Pulse count fluence versus pulse width (FWHM), all pulses in all fits combined.

Table 5.10: Correlations Between Pulse Count Fluence and Pulse Width Within Bursts.

Energy Channel	% Pos. Corr.	Binom. Prob.	$\beta < -1$	$-1 < \beta < 0$	$0 < \beta < 1$	$\beta > 1$	$\frac{1}{\text{Med.}(1/\beta)}$
1	$66/94 = 70\%$	8.9×10^{-5}	14	15	23	42	1.88
2	$77.5/109 = 71\%$	1.0×10^{-5}	20	13	25	51	1.46
3	$90.5/116 = 78\%$	$< 10^{-16}$	16	12	38	50	1.29
4	$27/35 = 77\%$	0.0013	3	5	17	10	1.03
All	$261/354 = 74\%$		53	45	103	153	1.41

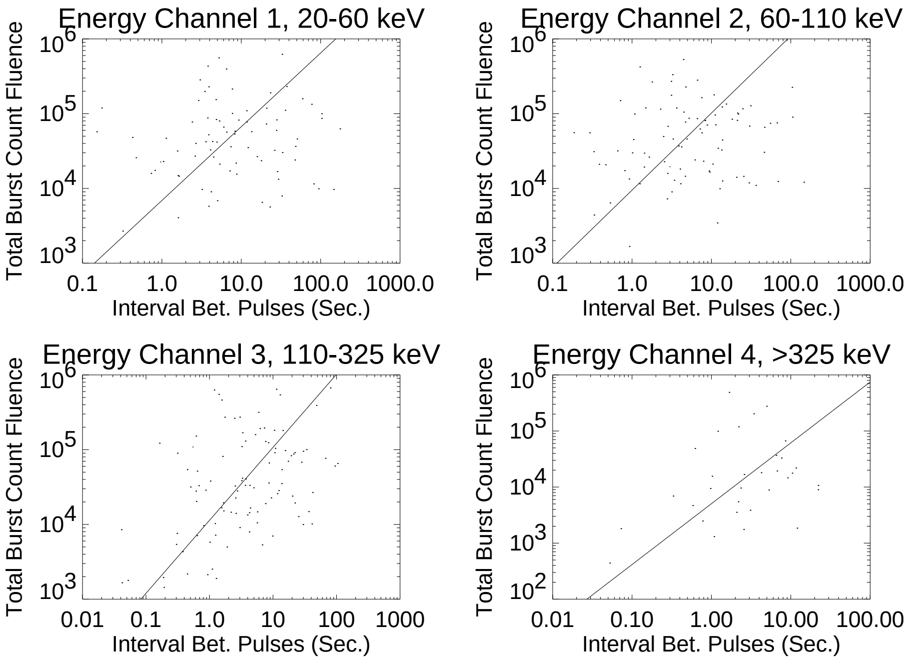

Figure 5.9: Total count fluence versus interval between two highest pulses in each fit.

have positive correlations in all energy channels as determined from the Spearman rank-order correlation coefficients. However, the correlation is statistically insignificant in all channels, except perhaps in channel 3. (See Table 5.11.)

We can also compare the count fluences of individual pulses with the time intervals between pulses within bursts. The results, shown in Table 5.12, show no statistically significant correlations between these two quantities.

The correlations between pulse count fluences and pulse widths are all positive, and probably result from the simple fact that pulses of longer duration tend to contain more counts. The correlation between total burst count fluence and the width of the highest amplitude pulse in each burst is probably a result of this correlation and the fact that the majority of the total count fluence of a burst is often contained in a single pulse. Any cosmological effects have been overwhelmed by other effects.

It is not clear why there appears to be no correlation between total burst count fluence and the interval between the two highest pulses in each burst. One possibility is that most of the observed bursts are sufficiently far away that the count fluence varies very little with luminosity distance. (See Figure 5.2.) However, this would place many bursts at redshifts

Table 5.11: Correlation Between Total Count Fluence and Interval Between Two Highest Pulses in Each Fit.

Energy Channel	r_s	Prob.	β
1	0.096	0.36	0.99 ± 0.03
2	0.15	0.11	1.03 ± 0.06
3	0.26	4.5×10^{-3}	0.98 ± 0.06
4	0.25	0.15	1.09 ± 0.10

Table 5.12: Correlations Between Pulse Count Fluence and Intervals Between Pulses Within Bursts.

Energy Channel	% Pos. Corr.	Binom. Prob.	$\beta < -1$	$-1 < \beta < 0$	$0 < \beta < 1$	$\beta > 1$	$\frac{1}{\text{Med.}(1/\beta)}$
1	33/62 = 53%	0.61	21	8.5	14.5	18	13.5
2	49.5/89 = 56%	0.29	19	18	18	34	6.5
3	54.5/95 = 57%	0.15	17	20	24	34	3.1
4	12/24 = 50%	1.0	4	9	7	4	-4.6
All	148/270 = 55%		61	55.5	63.5	90	6.8

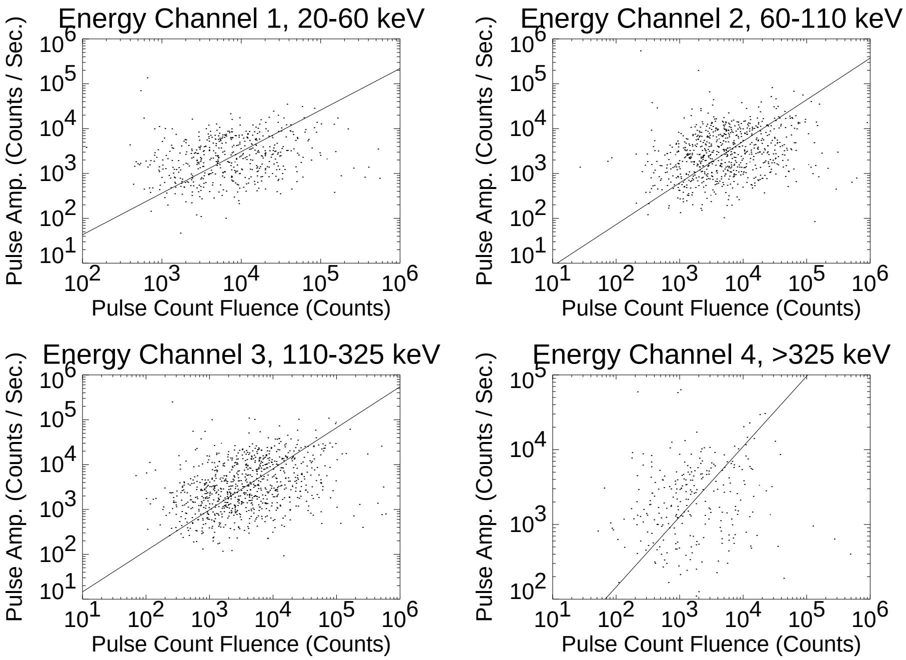

Figure 5.10: Pulse amplitude versus pulse count fluence, all pulses in all fits combined.

of $z > 10$, which seems unlikely given current evidence.

5.3 Correlations Between Flux and Fluence

Since the count fluence of a pulse scales as the product of its amplitude and its width, and a factor involving the peakedness ν, or equivalently, the amplitude of a pulse scales as its count fluence divided by its width, again with a factor involving ν, various selection effects could cause observed pulse amplitudes and widths to have an inverse correlation or cause observed pulse count fluences and widths to have a positive correlation. We might also expect pulse amplitudes and count fluences to show a positive correlation, and when we compare these for all pulses in all fits combined, we see that they indeed show a positive correlation. (See Figure 5.10 and Table 5.10.)

For the highest amplitude pulses in each burst, there is no significant correlation between the pulse amplitudes and the individual pulse count fluences. (See Figure 5.11 and Table 5.11.) This implies that the positive correlation seen between the pulse amplitudes and individual pulse count fluences for all pulses in all bursts combined must result from

Table 5.13: Correlation Between Pulse Amplitude and Pulse Count Fluence, All Pulses in All Fits Combined.

Energy Channel	r_s	Prob.	γ
1	0.19	1.8×10^{-5}	0.93 ± 0.02
2	0.21	3.8×10^{-9}	0.93 ± 0.02
3	0.32	2.4×10^{-22}	0.91 ± 0.02
4	0.12	0.052	0.94 ± 0.03

Table 5.14: Correlation Between Pulse Amplitude and Pulse Count Fluence, Highest Amplitude Pulse in Each Fit.

Energy Channel	r_s	Prob.	γ
1	0.059	0.46	0.97 ± 0.04
2	-0.10	0.18	-0.98 ± 0.04
3	0.022	0.77	0.97 ± 0.02
4	-0.23	0.054	-0.97 ± 0.05

correlations within the individual bursts. This in turn implies that the distribution of widths of pulses within individual bursts have a smaller range than the distribution of widths of all pulses in all bursts combined. The power law fits to these distributions give meaningless results due to the lack of actual correlation; the fits have different signs in different energy channels, and the fits from other linear regression methods give very different slopes.

It is the peak flux and total fluence of bursts that are candidates for standard candles, so it is useful to compare the amplitudes of the highest amplitude pulses in each burst with the total count fluences of each burst. Figure 5.12 and Table 5.15 show that there are no strong correlations between the maximum pulse amplitudes and the total count fluences of bursts. This result is somewhat mysterious, because even in the absence of cosmological effects, we would expect both peak flux and total fluence to scale approximately as the inverse square of the luminosity distance to the bursters (the effects of the time dilation factor $1+z$ are much smaller), and hence to have a positive correlation with each other. The total fluence divided by the peak flux gives a characteristic timescale of bursts, which Lee and Petrosian [66] call the *effective duration*, and have shown to be less subject to

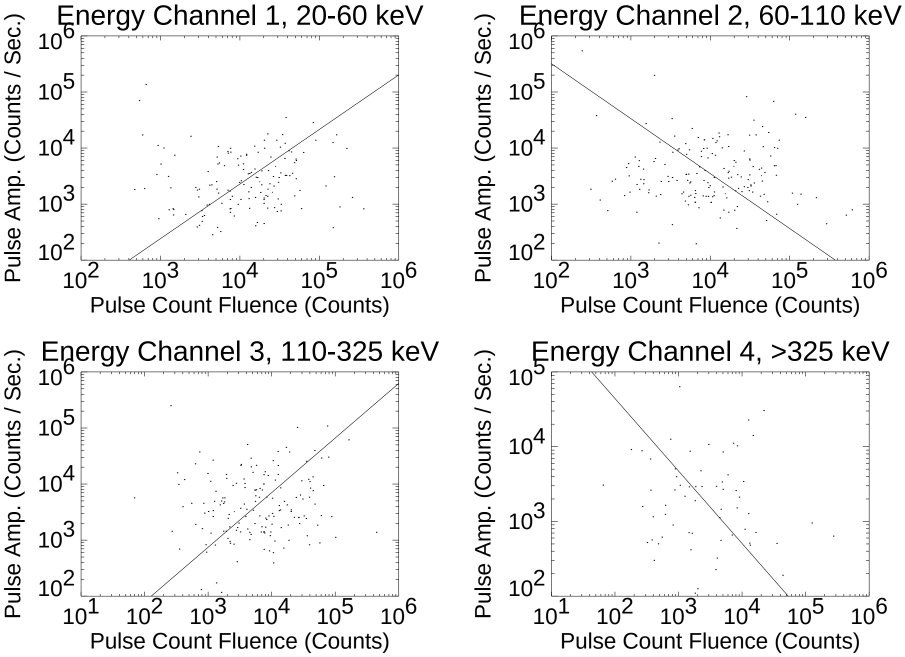

Figure 5.11: Pulse amplitude versus pulse count fluence, highest amplitude pulse in each fit.

signal-to-noise ratio related biases than the more commonly used T_{50} and T_{90} durations. The present result implies that the intrinsic range of the effective durations of bursts is large enough that distance effects cannot be seen in the distribution of fluences and peak fluxes. It also suggests that if one of the two brightness measures is a good standard candle, then the other cannot be a good standard candle, probably due to selection effects, or due to evolution of the characteristics or of the spatial distribution of the bursters themselves.

A significant majority of fits in all energy channels show a positive correlation between pulse count fluence and amplitude within bursts. (See Table 5.16.) In every energy channel, the majority of fits have pulse amplitudes varying as a small positive power, which we denote by γ, of the pulse count fluence within bursts.

It is not clear why there is no correlation between the highest pulse amplitude and the total count fluence of bursts, since we expect both quantities to decrease as the luminosity distances to the source increases. Again, it is possible that the sources are so distant that the count fluence varies little with redshift, as shown in Figure 5.2. However, if we plot the expected photon flux against the expected photon fluence, we see that this explanation

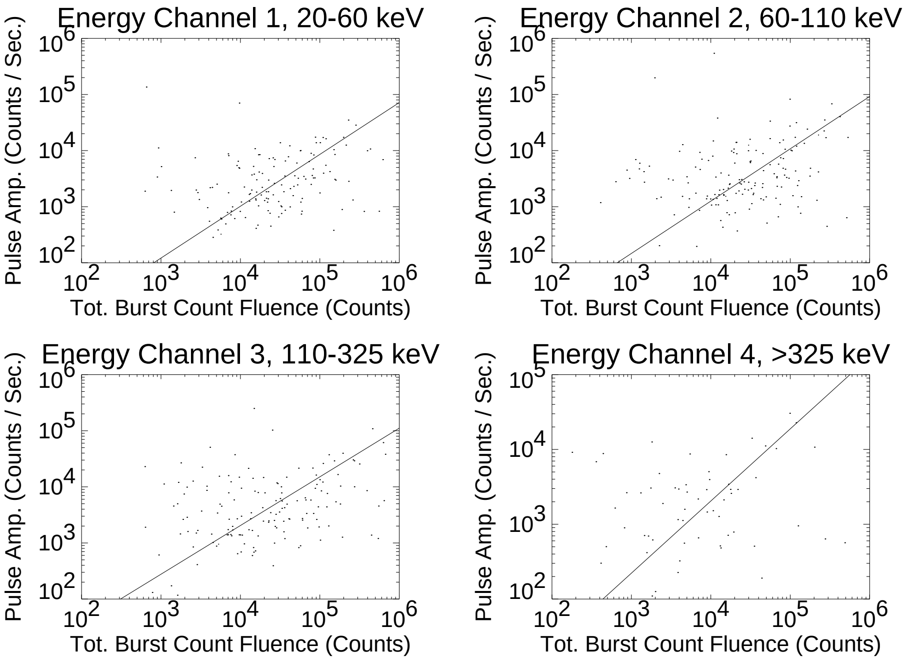

Figure 5.12: Amplitude of highest amplitude pulse versus total count fluence in each fit.

Table 5.15: Correlation Between Amplitude of Highest Amplitude Pulse and Total Count Fluence in Each Fit.

Energy Channel	r_s	Prob.	γ
1	0.13	0.096	0.92 ± 0.07
2	0.043	0.57	0.93 ± 0.05
3	0.15	0.053	0.87 ± 0.04
4	-0.036	0.77	0.96 ± 0.12

Table 5.16: Correlations Between Pulse Amplitude and Pulse Count Fluence Within Bursts.

Energy Channel	% Pos. Corr.	Binom. Prob.	$\gamma < -1$	$-1 < \gamma < 0$	$0 < \gamma < 1$	$\gamma > 1$	Med. γ
1	$71/94 = 76\%$	7.2×10^{-7}	8	18	54	14	0.48
2	$86.5/109 = 79\%$	$< 10^{-16}$	3	23	62	21	0.61
3	$85/116 = 73\%$	4.8×10^{-7}	6	22	75	13	0.63
4	$24/35 = 69\%$	0.028	3	8	19	5	0.61
All	$266.5/354 = 75\%$		20	71	210	53	0.58

seems unlikely, because when z is large enough that there is little variation in count fluence, there is also relatively little variation in photon flux. (See Figure 5.13.) The correlations between pulse amplitudes and pulse count fluences within bursts are likely to result from the fact that higher amplitude pulses tend to contain more counts.

5.4 Correlations Between Flux and Pulse Asymmetry

It has been reported that when considering the averaged time profiles of bursts, the decay times from the peaks of bursts show an inverse correlation with peak flux, while the rise times to the peaks of bursts show a smaller inverse correlation or no variation at all with peak flux.[92, 56, 93, 94] Such a result could not come from cosmological time dilation, but would have to be caused by the burst production mechanism itself, or by some selection effect, perhaps resulting from the BATSE trigger criteria, which selects for fast-rising bursts [69] and is independent of burst decay times. It is possible that a similar effect could appear in the individual pulses comprising bursts, as a *positive* correlation between pulse amplitudes and pulse rise time to decay time ratios. Although there may be selection effects in the pulse-fitting procedure that could bias correlations between pulse amplitudes and pulse rise times, or between pulse amplitudes and pulse decay times, most of these should affect both rise and decay times equally, and therefore shouldn't affect pulse asymmetry ratios.

For bursts consisting of a single pulse, the pulse rise and decay times are of course the rise and decay times for the entire burst. The plots of pulse asymmetries versus pulse amplitudes (Figure 5.14) don't show any clear correlations, but suggest that the range

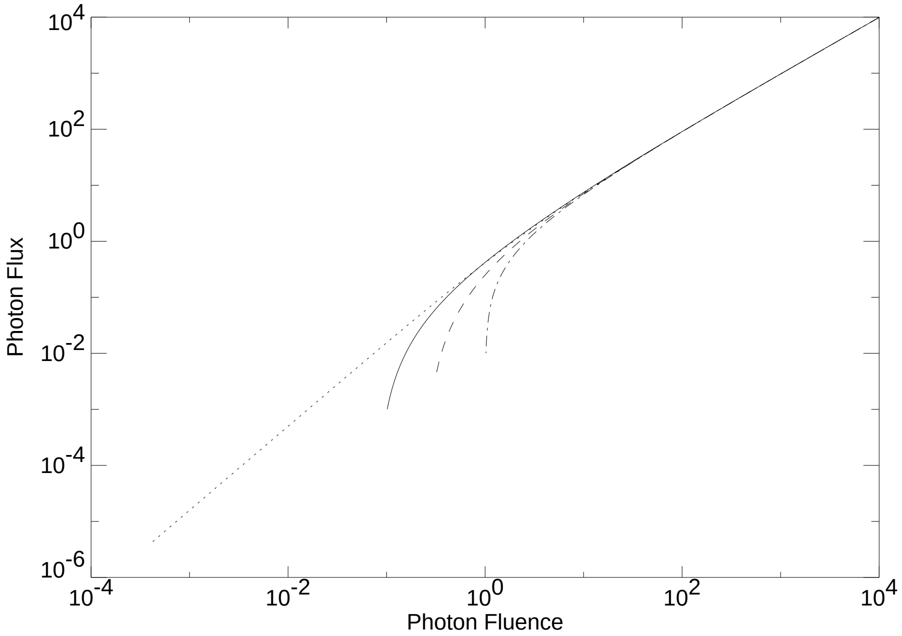

Figure 5.13: Apparent photon flux versus apparent photon fluence for $z = 0.01$ (upper right) to $z = 100$ (lower left) and for $\Omega_\Lambda = 0.76$ and $\Omega_M = 0.24$ (solid line), and for $\Omega_\Lambda = 0$ and $q_0 = 0$ (dotted line), $q_0 = 1/2$ (dashed line) and $q_0 = 1$ (dash-dotted line).

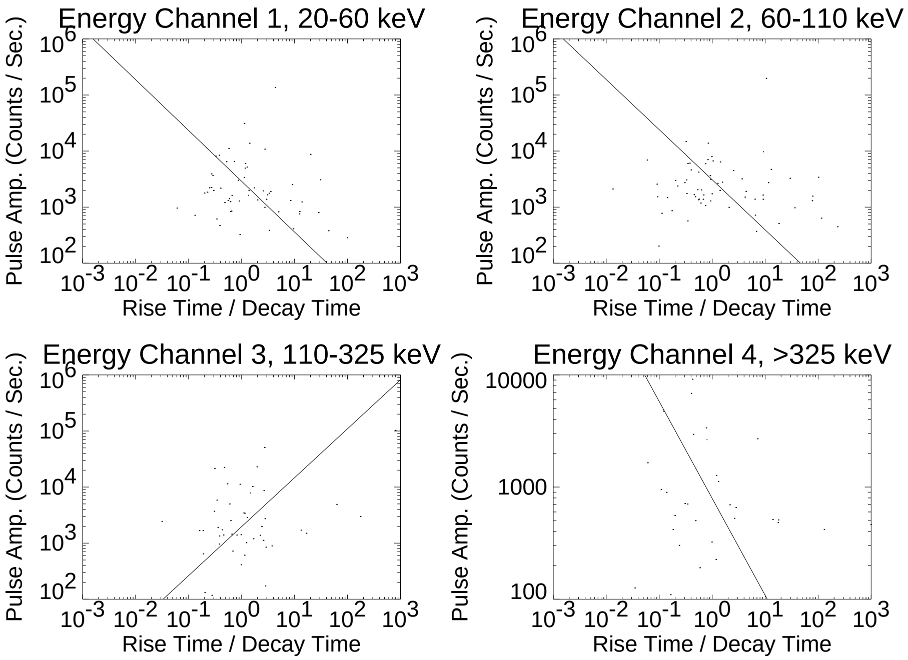

Figure 5.14: Pulse amplitude versus pulse asymmetry, single-pulse fits.

of pulse asymmetry ratios is broader for lower amplitude bursts than for higher amplitude bursts. The latter effect could result from the lower signal-to-noise of lower amplitude pulses. The Spearman rank-order correlation coefficients (Table 5.17) comparing pulse amplitudes and pulse asymmetries of single-pulse bursts actually show rather weak evidence of an *inverse* correlation in energy channels 1, 2, and 4, and no correlation in channel 3. The power law fits using the OLS bisector method give negative power laws, which we denote by δ, in channels 1, 2, and 4, and a positive power law in channel 3. Pulses with asymmetry ratios smaller than 10^{-3} or greater than 10^{3} were removed for all of the power law fits involving pulse asymmetry ratios because the untruncated plots showed that they were outside the main part of the distribution.

We have seen earlier that single-pulse bursts appear to have larger pulse asymmetry ratios than pulses in multiple-pulse bursts. Although the properties of individual pulses in multiple-pulse bursts may be different from those of the entire bursts, it may still be useful to look for correlations between pulse amplitude and asymmetry for individual pulses in multiple-pulse bursts. For the highest amplitude pulses from each fit, plots of pulse asymmetry versus pulse amplitude (See Figure 5.15) show that pulse asymmetries span a

Table 5.17: Correlation Between Pulse Amplitude and Asymmetry, Single Pulse Fits.

Energy Channel	r_s	Prob.	δ
1	-0.25	0.049	-0.91 ± 0.10
2	-0.27	0.022	-0.89 ± 0.20
3	0.01	0.93	0.87 ± 0.11
4	-0.27	0.12	-0.86 ± 0.20

Table 5.18: Correlation Between Pulse Amplitude and Asymmetry, Highest Amplitude Pulse in Each Fit.

Energy Channel	r_s	Prob.	δ
1	-0.24	0.0020	-0.89 ± 0.06
2	-0.32	1.7×10^{-5}	-0.84 ± 0.06
3	-0.15	0.051	-0.99 ± 0.04
4	-0.13	0.30	-0.26 ± 0.09

larger range of values at lower amplitudes. The Spearman rank-order correlation coefficients (See Table 5.18) show weak inverse correlations in energy channels 1 and 3, a strong inverse correlation in channel 2, and no correlation in channel 4.

Combining all pulses in all fits (See Table 5.19) shows no correlation between pulse amplitude and pulse asymmetry in energy channels 1 and 3, a weak inverse correlation in channel 4, and an apparently strong inverse correlation in channel 2. It is not clear why the different energy channels give such different results. The plots (See Figure 5.16) again show that pulse asymmetries span a larger range of values at lower amplitudes.

In energy channels 2 and 3, slightly more fits show positive correlations within bursts between pulse asymmetry ratio and pulse amplitude than show inverse correlations, but this doesn't appear to be statistically significant, except possibly in channel 3. (See Table 5.20.)

There is no clear evidence of any correlations between pulse amplitudes and pulse asymmetry, so that the variations of pulse rise time and pulse decay time with pulse amplitude don't appear to be significantly different.

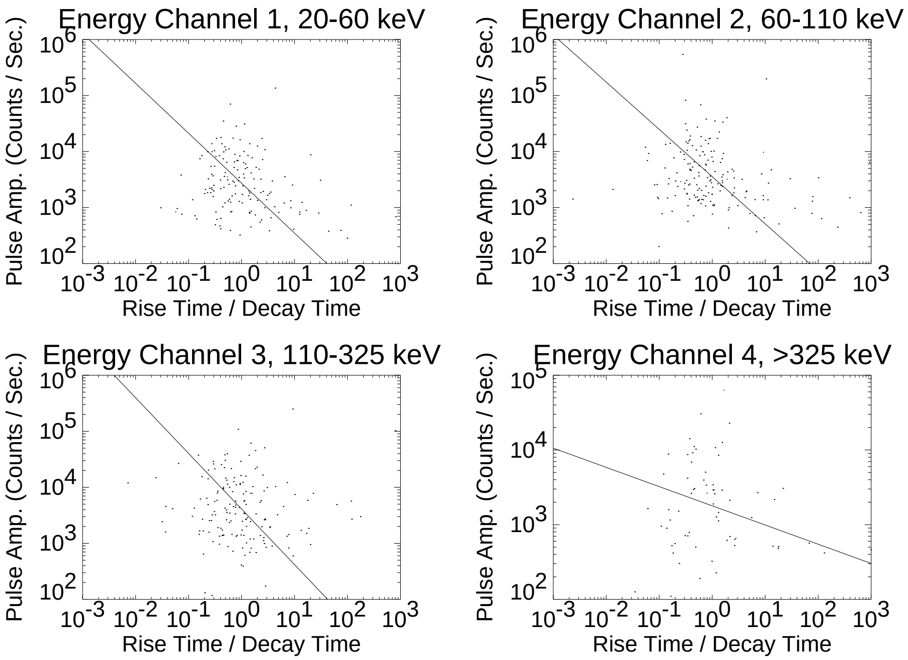

Figure 5.15: Pulse amplitude versus pulse asymmetry, highest amplitude pulse in each fit.

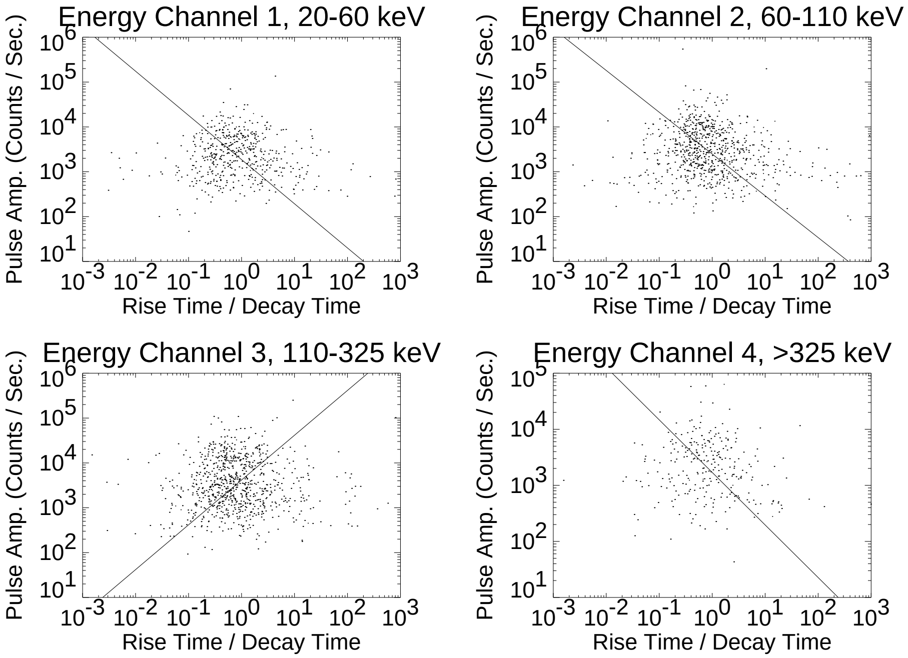

Figure 5.16: Pulse amplitude versus pulse asymmetry, all pulses in all fits combined.

Table 5.19: Correlation Between Pulse Asymmetry and Amplitude, All Pulses in All Fits Combined.

Energy Channel	r_s	Prob.	δ
1	-0.04	0.37	-0.99 ± 0.04
2	-0.15	4.3×10^{-5}	-0.93 ± 0.02
3	0.01	0.78	1.00 ± 0.01
4	-0.14	0.022	-0.94 ± 0.04

Table 5.20: Correlations Between Pulse Asymmetry and Amplitude Within Bursts.

Energy Channel	% Pos. Corr.	Binom. Prob.	$\delta < -1$	$-1 < \delta < 0$	$0 < \delta < 1$	$\delta > 1$	Med. δ
1	47/94 = 50%	1	7	42	36	9	-0.029
2	60/109 = 55%	0.29	6	48	44	11	-0.066
3	70.5/116 = 61%	0.020	5	52	50	9	0.077
4	17/35 = 49%	0.87	2	16	14	3	-0.090
All	194.5/354 = 55%		20	158	144	32	-0.0093

Chapter 6

Testing for Selection Effects

There are a number of ways in which the pulse-fitting procedure may introduce selection effects into correlations between pulse characteristics. One is that the errors in the different fitted pulse parameters may be correlated. Another is that the pulse-fitting procedure may miss some pulses by not identifying them above the background noise. Still another cause of selection effects is that overlapping pulses may be identified as a single broader pulse.

In order to characterize possible selection effects in the pulse-fitting procedure, simulated bursts with known characteristics were generated and fitted. For each simulated burst, a random number of pulses was chosen with the probability of n pulses proportional to $1/n^{1.4}$. A background rate was generated according to a log-normal distribution based on the distribution of fitted background rates for the actual burst time profiles observed by BATSE, with the background slope set to 0. Then for each pulse in the burst, the pulse amplitude, pulse width, peakedness ν, asymmetry ratio, and peak time were generated randomly and independently according to log-normal distributions. These distributions were also based on the distributions of parameters fitted to the actual burst time profiles observed by BATSE. The characteristics of the pulses in the simulated bursts were generated with no correlations between different pulse characteristics within individual pulses, or between different pulses.

For each simulated burst, 2^{20} independent counts were randomly generated according to the simulated time profiles, and the time of every 64^{th} count was taken to obtain a spill time. These spill times were truncated at 240 seconds because the BATSE TTS data that was fitted always ended at 240 seconds. The simulated spill times were then fitted using the pulse-fitting program in the same way that the actual BATSE TTS data was fitted.

Table 6.1: Number of Pulses.

	Median No. of Pulses	Mean No. of Pulses	Max. No. of Pulses	% Single Pulse
Simulation	3	9.3	126	62/286 = 22%
Fit to Sim.	2	3.6	19	88/286 = 31%

Table 6.2: Differences Between Numbers of Pulses Between Simulations and Fits.

	Median Difference	Mean Difference	$\% < 0$
Fit - Sim.	-1	-15.1	154/286 = 54%

6.1 Numbers of Bursts and Pulses

A total of 286 simulated bursts were generated, with only one energy channel for each burst. For many of these, the limit of 2^{20} counts was reached before the 240 second limit, which almost never occurred in the actual BATSE TTS data. These simulated bursts contained a total of 2671 pulses that had peak times before the limits of 2^{20} counts and 240 seconds, while the fits to the simulated bursts contained a total of only 1029 pulses. Of these, 223 of the simulated bursts and 198 of the fits to the simulations contained more than one pulse. (See Figure 6.1 and Table 6.1.) Note that in the fits to actual BATSE data, the largest number of fits containing more than one pulse was 116 for energy channel 3, so that the simulated data set is larger. Figure 6.2 shows the number of pulses fitted versus the number of pulses originally generated for each simulated bursts. It shows that the greatest differences between the the fitted and the simulated numbers of pulses tend to occur in the most complex bursts. Figure 6.3 and Tables 6.2 and 6.3 compare the numbers of pulses per fit between the simulations and the fits to simulations.

Table 6.3: Ratios of Numbers of Pulses Between Simulations and Fits.

	Median Ratio	Geo. Mean Ratio
Fit / Sim.	0.80	0.63

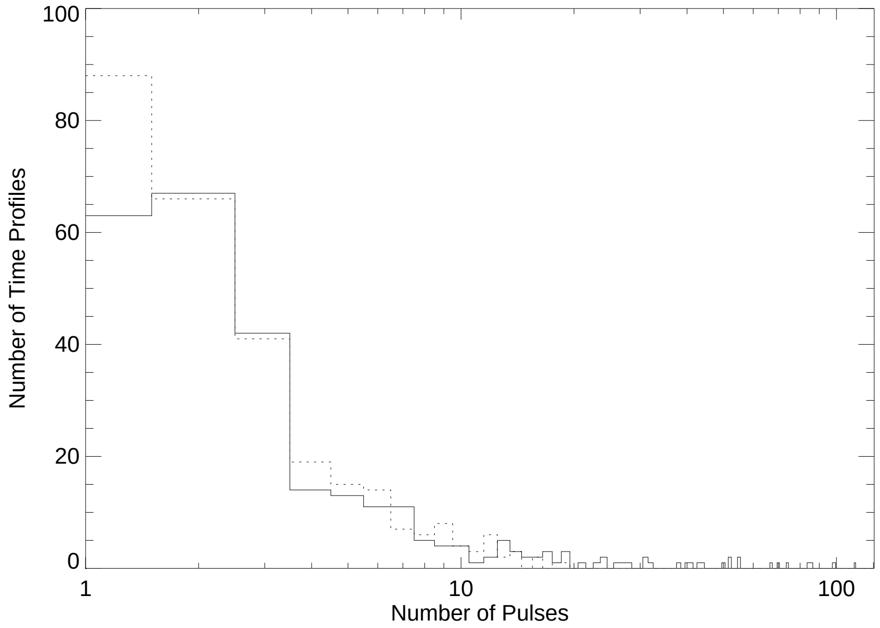

Figure 6.1: Number of pulses. Solid line is simulations, dashed line is fits.

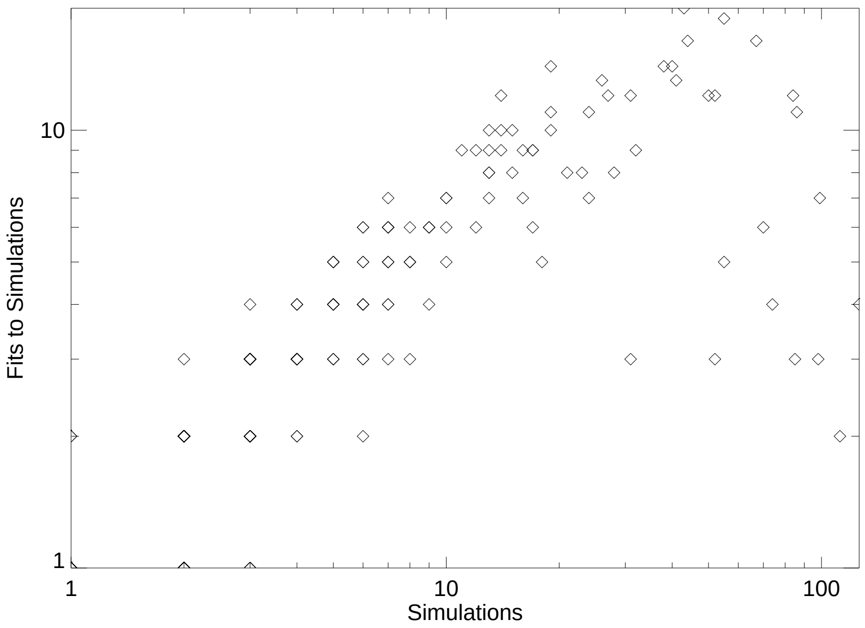

Figure 6.2: Number of pulses in fits versus simulations.

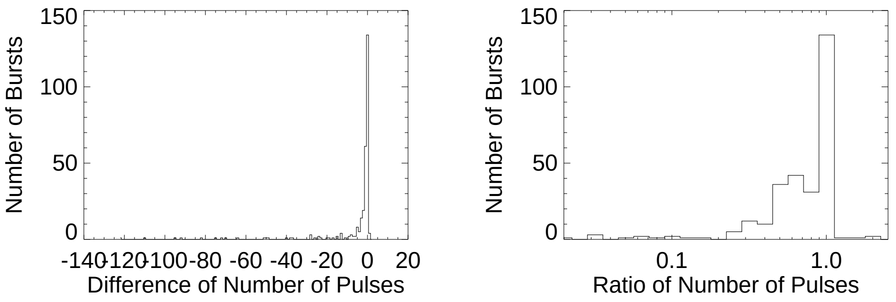

Figure 6.3: Differences and ratios of number of pulses between simulations and fits.

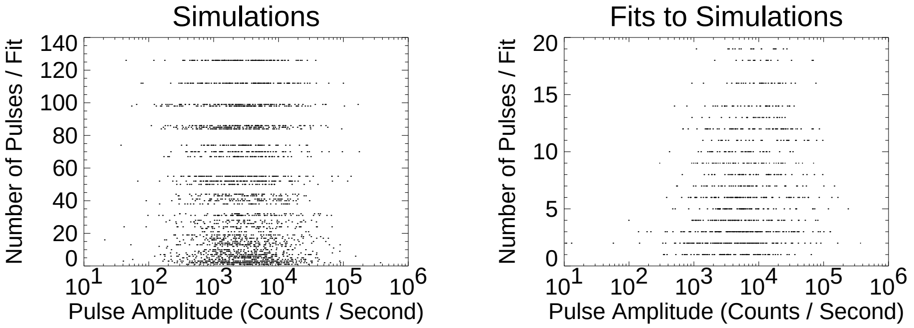

Figure 6.4: Number of pulses per fit versus pulse amplitudes of all pulses.

6.2 Pulse Amplitudes

Figure 6.4 shows the number of pulses in each burst plotted against the amplitudes of all of the pulses comprising each fit. In the simulations, there are no correlations between pulse amplitudes and the number of pulses in the time profile, because the pulse amplitudes were generated independently of the number of pulses in each burst. In the fits to the simulations, pulse amplitudes tend to be higher in bursts containing more pulses. This must result from the selection effect discussed in Section 4.4; it is easier to identify more pulses when they are stronger. Table 6.4 shows no correlation between pulse amplitudes and the number of pulses for the simulations, and strong positive correlations for the fits to simulations.

Figure 6.5 and Table 6.5 compare the number of pulses in each time profile with the amplitude of the highest amplitude pulse in each burst. They show that for both the simulations and the fits to the simulations, more complex bursts tend to have higher peak count rates, as measured by the amplitude of the highest pulse. This occurs because of

Table 6.4: Correlation Between Number of Pulses per Fit and Pulse Amplitudes for All Pulses.

	r_s	Prob.
Simulation	-0.04	0.042
Fit to Sims.	0.22	7.1×10^{-13}

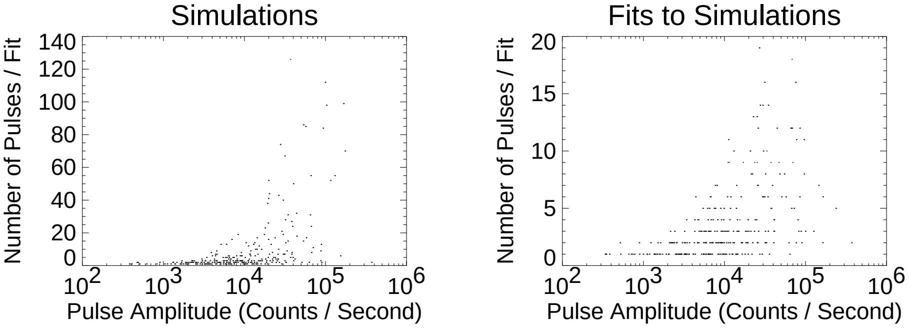

Figure 6.5: Number of pulses per fit versus pulse amplitude, highest amplitude pulse in each fit.

the selection effect described above, and because more complex bursts have more pulses to select from in finding the highest amplitude pulse.

6.3 Pulse Widths

Figure 6.6 and Table 6.6 compare the number of pulses in each time profile with the widths of the individual pulses. They show no tendency for pulses to be wider or narrower in bursts with more pulses, in either the simulations or the fits to the simulations. This suggests that the negative correlation between the number of pulses in each fit and the pulse widths seen

Table 6.5: Correlation Between Number of Pulses per Fit and Pulse Amplitudes, Highest Amplitude Pulse in Each Fit.

	r_s	Prob.
Simulation	0.62	2.5×10^{-32}
Fit to Sims.	0.60	3.2×10^{-29}

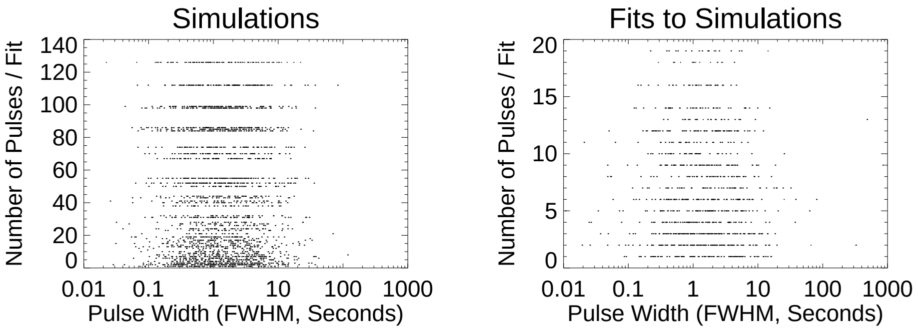

Figure 6.6: Number of pulses per fit versus widths of all pulses.

Table 6.6: Correlation Between Number of Pulses per Fit and Widths of All Pulses.

	r_s	Prob.
Simulation	0.01	0.76
Fit to Sims.	-0.03	0.36

in the fits to actual bursts (Figure 4.16 and Table 4.21) do not result from selection effects in the pulse-fitting procedure, but are intrinsic to the burst production mechanism, or may arise from other effects.

6.4 Time Intervals Between Pulses

Figure 6.7 shows the distributions of the intervals between the peak times of adjacent pulses for both the simulations and the fits to simulations. It shows that the separations between pulses are greater in the fits to the simulations, indicating that the fitting procedure selects for pulses with greater separations. However, if we compare this with Figure 4.17, we see that the fits to actual BATSE bursts found pulses that are much more closely spaced than the fits to simulated bursts found. We also see that the original simulated bursts contain pulses that are far more closely spaced than even that. It may be that the simulation generated pulses that are much closer together than occurs in actual BATSE bursts, and therefore have far more overlap, so that the fits to the simulations may have missed more pulses than the fits to actual BATSE bursts missed. This is an unfortunate limitation of the fact that the simulation makes no attempt to model the spacing of the pulses within bursts.

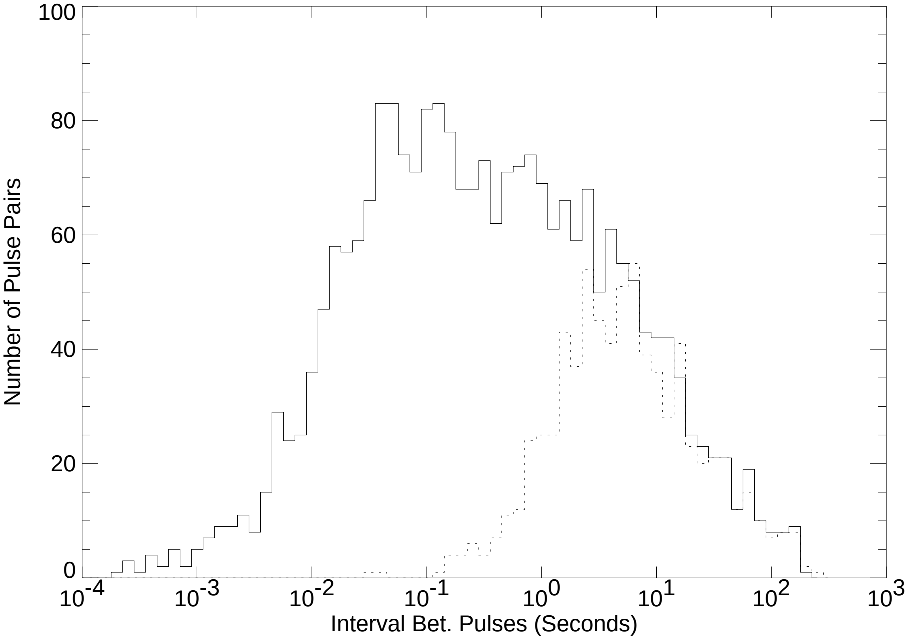

Figure 6.7: Intervals between peak times of adjacent pulses. Solid line is simulations, dashed line is fits.

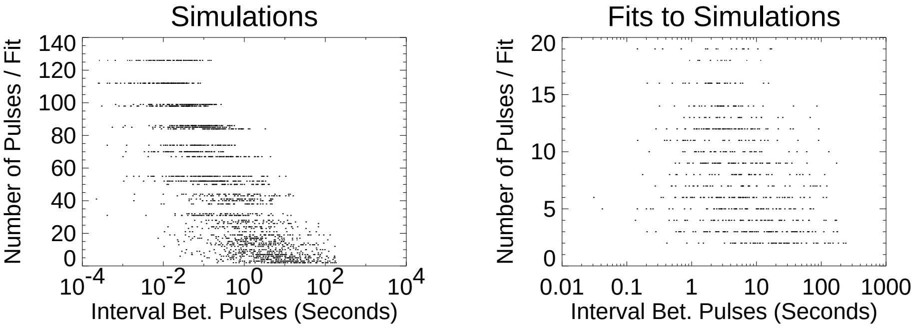

Figure 6.8: Number of pulses per fit versus intervals between adjacent pulses.

Table 6.7: Correlation Between Number of Pulses per Fit and Intervals Between Adjacent Pulses.

	r_s	Prob.
Simulation	-0.80	0
Fits to Sim.	-0.35	6.5×10^{-23}

Figure 6.8 shows the intervals between peak times of adjacent pulses in the simulations and fits to simulations. It shows that in both the simulations and the fits to simulations, pulses are closer together in bursts with more pulses. This is as expected, since pulse peak times were generated independently of each other and of the number of pulses per burst, so more complex bursts will tend to have more pulses in any given time interval. Table 6.7 shows that this correlation is weaker for the fits to simulations than for the original simulations. This probably results from the fitting procedure selecting for pulses with greater separations.

Figure 6.9 and Table 6.8 compare the number of pulses in each time profile with the time intervals between the first and last pulses in each burst, *for the simulated bursts where no pulses were truncated by the* 2^{20} *count limit.* They show that in both the simulations and the fits to simulations, the time intervals between the first and last pulse are greater in bursts with more pulses. This is also as expected since the peak times of pulses were generated independently of the number of pulses in each burst.

Figure 6.10 and Table 6.9 compare the number of pulses in each time profile with the time intervals between the peak times of the two highest amplitude pulses in each burst, *for the simulated bursts where no pulses were truncated by the* 2^{20} *count limit.* They show

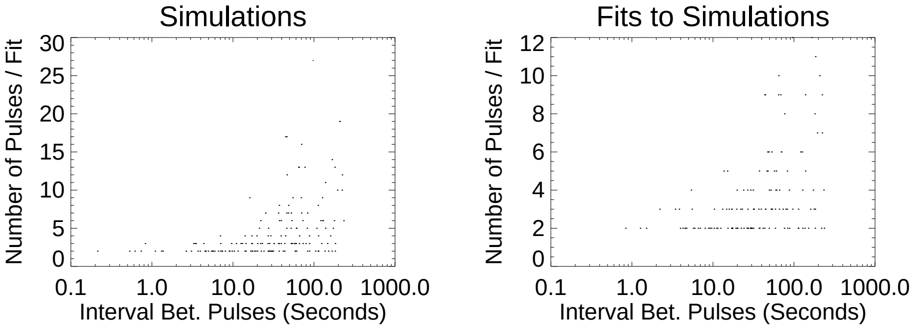

Figure 6.9: Number of pulses per fit versus interval between first and last pulse in each fit.

Table 6.8: Correlation Between Number of Pulses per Fit and Intervals Between First and Last Pulse.

	r_s	Prob.
Simulation	0.55	1.1×10^{-14}
Fits to Sim.	0.49	6.2×10^{-10}

no tendency for these intervals to be shorter or longer in bursts with more pulses.

6.5 Count Fluences

Figure 6.11 and Table 6.10 compare the number of pulses in each time profile with the count fluences of the individual pulses. They show no tendency for pulses to contain fewer or more counts in bursts with more pulses. This differs from the results seen in the fits to actual bursts, where there was a negative correlation between pulse count fluences and burst complexity. (See Figure 4.29 and Table 4.36.) This may explain why the 2^{20} count limit for the TTS data was frequently reached before the 240 second time limit in the simulated

Table 6.9: Correlation Between Number of Pulses per Fit and Intervals Between Two Highest Amplitude Pulses in Each Fit.

	r_s	Prob.
Simulation	0.01	0.86
Fit to Sims.	-0.10	0.22

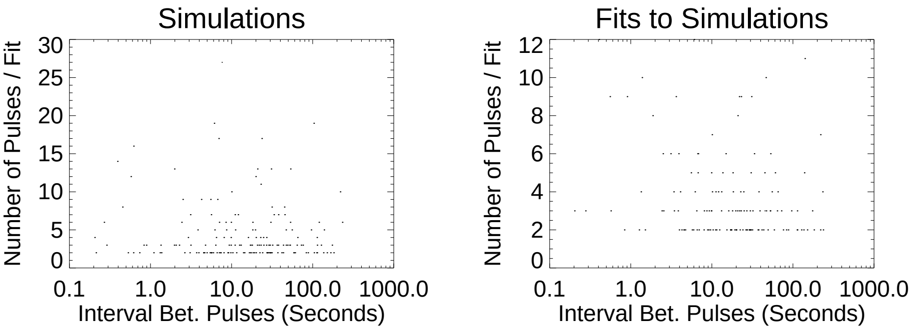

Figure 6.10: Number of pulses per fit versus intervals between two highest amplitude pulses in each fit.

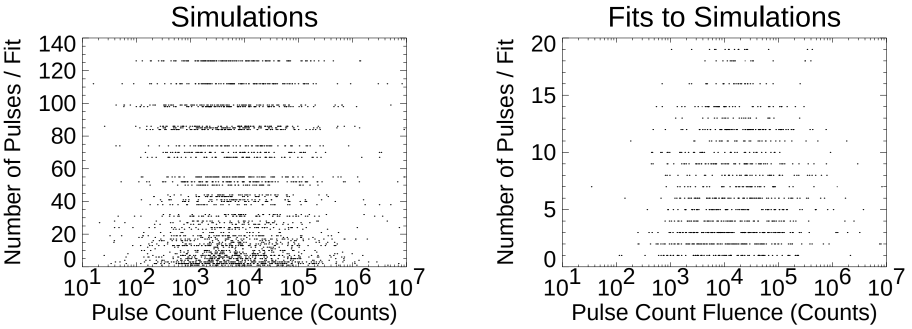

Figure 6.11: Number of pulses per fit versus count fluences of all pulses.

bursts, but rarely in the actual bursts.

Table 6.11 gives the minimum, median, and mean percentages of the total burst count fluences that are contained in the single pulse with highest count fluence in each fit, and the percentage of bursts where a single pulse contains more than 50% of the total count fluence.

Figure 6.13 and Table 6.12 compare the number of pulses in each time profile with the total count fluences of the bursts. They show that bursts with more pulses tend to contain

Table 6.10: Correlation Between Number of Pulses per Fit and Count Fluences of All Pulses.

	r_s	Prob.
Simulation	-0.02	0.31
Fit to Sims.	0.11	0.00068

Table 6.11: Fraction of Total Burst Count Fluences Contained in a Single Pulse.

	Min. % in 1 Pulse	Median % in 1 Pulse	Mean % in 1 Pulse	% $> \frac{1}{2}$ Fluence in 1 Pulse
Simulation	21%	87%	79%	87%
Fit to Sim.	27%	92%	82%	86%

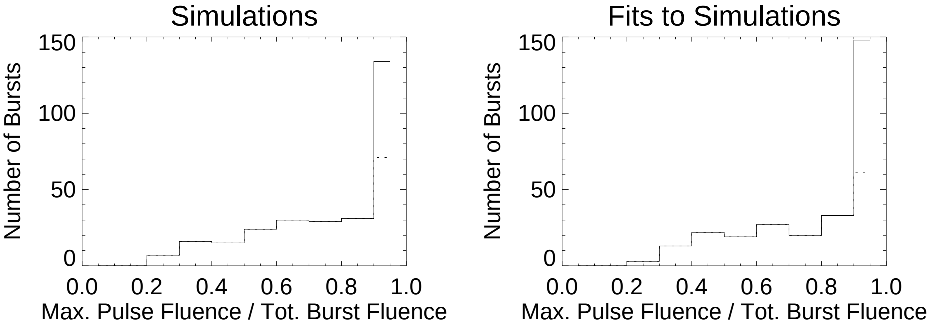

Figure 6.12: Fraction of burst count fluence contained in a single pulse. Dashed lines are multiple-pulse fits (only affects the last bin).

more total counts in both the simulations and the fits to simulations.

6.6 Time Evolution of Pulse Asymmetries Within Bursts

In the fits to actual BATSE data, it was found that pulse asymmetry ratios tended to decrease over the course of a burst. (See Table 4.45.) Table 6.13 shows the correlations between pulse asymmetry ratio and peak times within bursts for the simulations and the fits to simulations. It shows no tendency for positive or negative correlations in either the simulations or the fits to simulations. This indicates that the tendency for pulse asymmetry

Table 6.12: Correlation Between Number of Pulses per Fit and Total Burst Count Fluences.

	r_s	Prob.
Simulation	0.72	0
Fit to Sims.	0.64	2.0×10^{-34}

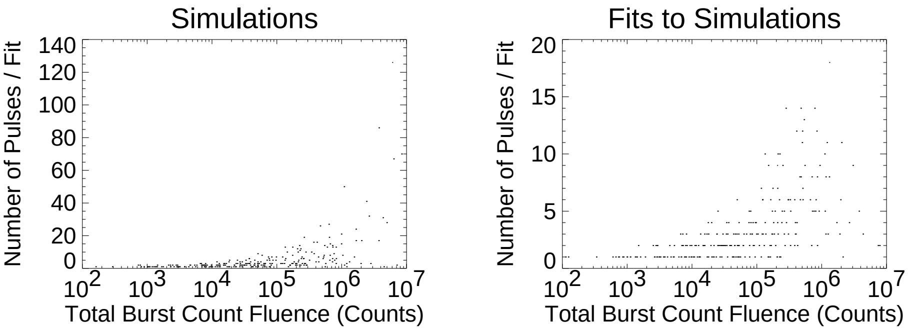

Figure 6.13: Number of pulses per fit versus total burst count fluences.

Table 6.13: Correlations Between Pulse Asymmetry Ratio and Pulse Peak Time Within Bursts.

	% Decreasing	Binom. Prob.
Simulation	92.5/223 = 41%	0.016
Fit to Sim.	103/198 = 52%	0.57

ratios to decrease with time within bursts does not arise from selection effects in the pulse-fitting procedure, so the tendency appears to be intrinsic to gamma-ray bursts.

6.7 Correlations Between Pulse Amplitudes and Timescales

Figure 6.14 shows the pulse amplitudes versus pulse width for all pulses in all fits combined, as generated by the simulation and as fitted. It shows that the fitting procedure tends to select for higher amplitude pulses, but doesn't appear to have strong selection effects for pulse width, though there may be some selection for longer duration pulses. Table 6.14 show the correlations between pulse amplitude and pulse width for all pulses in all fits combined. It shows that for the simulated pulse parameters, there is no correlation between pulse width and pulse amplitude, as expected because the simulation was designed with no correlation. It shows a negative correlation between pulse width and pulse amplitude in the fits to the simulations, which appears to be weaker and far less statistically significant than in the fits to actual BATSE data.

Figure 6.15 shows the pulse amplitudes versus pulse widths for the highest amplitude pulse in each burst. It shows that these distributions are very similar for the simulated

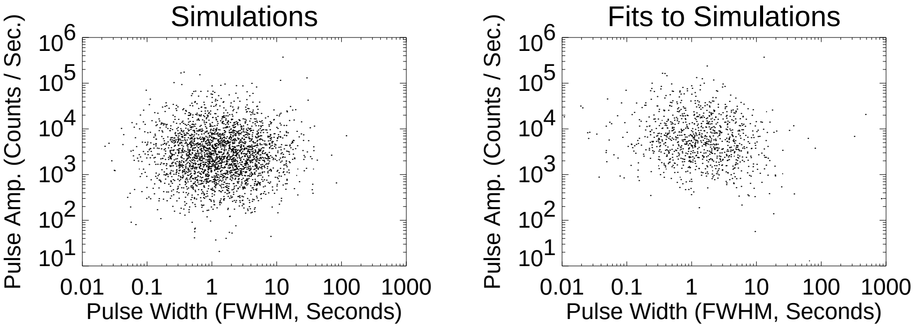

Figure 6.14: Pulse amplitude versus pulse width (FWHM), all pulses in all fits combined.

Table 6.14: Correlation Between Pulse Amplitude and Pulse Width (FWHM), All Pulses in All Fits Combined.

	r_s	Prob.
Simulation	0.0068	0.73
Fit to Sim.	-0.14	2.1×10^{-6}

bursts and for the fits to the simulations. Table 6.15 shows the correlations between pulse amplitude and pulse width for the highest amplitude pulse in each burst. It shows no correlation for either the simulations or the fits to the simulations. This suggests that the correlations observed in the fits to actual bursts observed by BATSE are not caused by selection effects in the fitting procedure, so they may arise from cosmological time dilation, intrinsic properties of the bursters, or selection effects arising from the BATSE triggering criteria.

Table 6.16 shows the correlations between pulse width and pulse amplitude within individual bursts. It shows that there are no correlations in the simulated bursts. In the fits to the simulations, however, more bursts show a negative correlation between pulse

Table 6.15: Correlation Between Pulse Amplitude and Pulse Width (FWHM), Highest Amplitude Pulse in Each Fit.

	r_s	Prob.
Simulation	0.0059	0.92
Fit to Sim.	-0.075	0.20

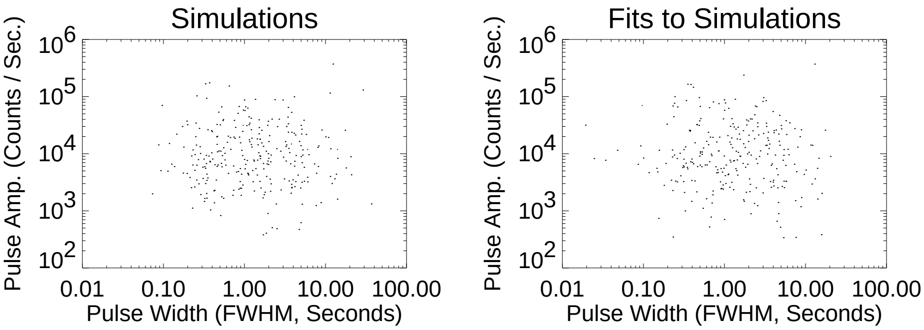

Figure 6.15: Pulse amplitude versus pulse width (FWHM), highest amplitude pulse in each fit.

Table 6.16: Correlations Between Pulse Amplitude and Pulse Width Within Bursts.

	% Neg. Corr.	Binom. Prob.	$\alpha < -1$	$-1 < \alpha < 0$	$0 < \alpha < 1$	$\alpha > 1$	Med. α
Sim.	104.5/223 = 47%	0.35	39	55	65	64	0.55
Fit to Sim.	126.5/198 = 64%	9.3×10^{-5}	32	86	53	24	-0.39

amplitude and pulse width than show a positive correlation. This asymmetry appears to be as large as it is for the fits to actual BATSE data, which would suggest that the observed tendency for higher amplitude pulses within bursts to be narrower arises largely from a selection effect in the pulse-fitting procedure. However, when we examine the fits to simulated bursts for which the rank correlations have the greatest statistical significance, we find that the same fraction have positive correlations between pulse widths and pulse amplitudes as for fits where the rank correlations have weaker statistical significance; the asymmetry doesn't depend on the statistical significance of the correlations, unlike the fits to actual bursts.[84, 95] Therefore, the observed inverse correlations between pulse widths and pulse amplitudes within actual bursts appear to arise in part from intrinsic properties of the bursters.

We can find correlations between the errors in the fitted pulse parameters by comparing the parameters used in the simulations with those in the fits. For simulated bursts consisting of a single pulse in both the original simulation and in the fit, the identification of pulses between the simulation and the fit is unambiguous and unaffected by the effects of missing

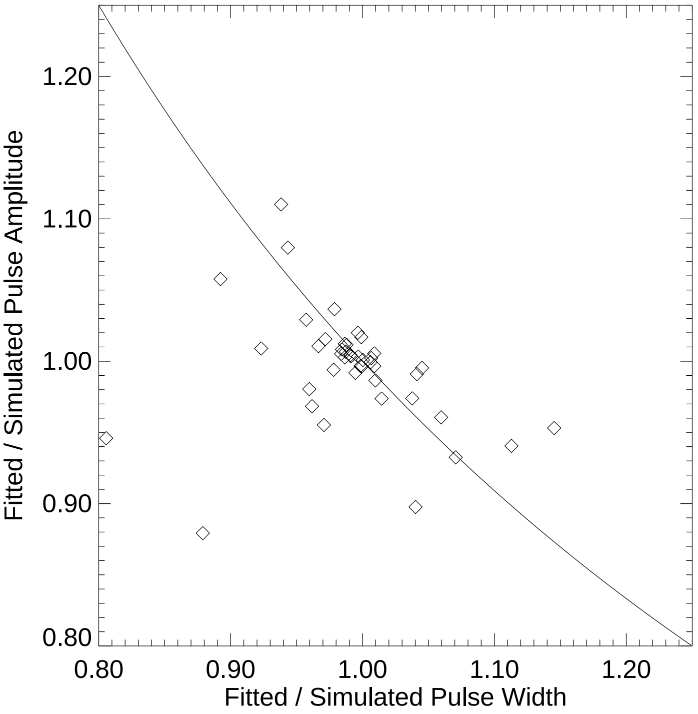

Figure 6.16: Ratios of fitted to simulated pulse amplitudes versus ratios of fitted to simulated pulse widths, with line of constant count fluence, for single-pulse simulated bursts.

pulses. Figure 6.16 shows that the errors in the fitted pulse amplitudes and the fitted pulse widths tend to have an inverse correlation; when the fitted amplitude is larger than the original amplitude, the fitted width tends to be smaller than the original width, and vice versa. The same effect also appears when we compare the highest amplitude pulses from all bursts, or all pulses matched between the simulations and the fits to the simulations. This selection effect may cause weak inverse correlations between pulse amplitude and pulse width within fits to actual or simulated bursts, so it may be another reason why a large majority of both actual BATSE bursts and fits to simulated bursts show an inverse correlation between pulse amplitude and pulse width within the bursts.

Figure 6.17 shows the pulse amplitudes versus the intervals between the peak times of the two highest amplitude pulses in each burst, *for the simulated bursts with multiple pulses and where no pulses in the simulation were truncated by the* 2^{20} *count limit.* It shows that these distributions are also very similar for the simulated bursts and for the fits to the simulations,

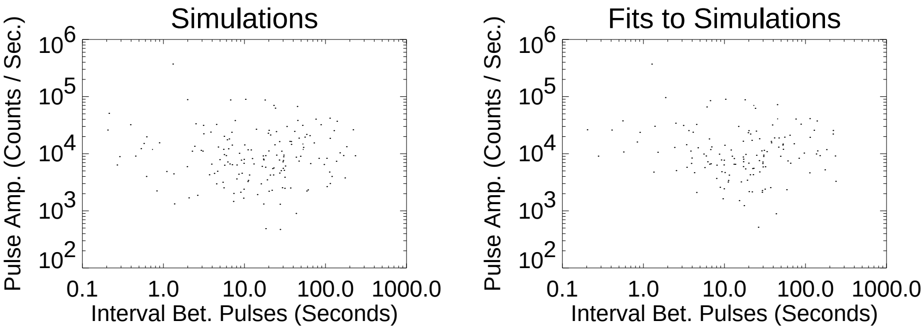

Figure 6.17: Highest pulse amplitude versus interval between two highest pulses in each fit.

Table 6.17: Correlation Between Highest Pulse Amplitude and Interval Between Two Highest Pulses in Each Fit.

	r_s	Prob.
Simulation	0.03	0.74
Fit to Sim.	-0.01	0.93

although the fits to simulations tend to miss points when both the peak amplitudes and the intervals between the two highest amplitude pulses are small. Table 6.17 shows the correlations between pulse amplitude and the intervals between the two highest amplitude pulses, for the same set of simulated bursts. It also shows no significant correlation for either the simulations or the fits to the simulations. This suggests that the correlations observed in the fits to actual bursts observed by BATSE are not caused by selection effects in the fitting procedure, so they may arise from cosmological time dilation or from intrinsic properties of the bursts.

Table 6.18 shows the correlations between intervals between pulses and pulse amplitude within individual bursts. It shows that there are no correlations in the simulated bursts. In the fits to the simulations, more bursts show a negative correlation between pulse amplitude and intervals between pulses than show a positive correlation, but the effect is statistically insignificant.

Table 6.18: Correlations Between Pulse Amplitude and Intervals Between Pulses Within Bursts.

	% Neg. Corr.	Binom. Prob.	$\alpha < -1$	$-1 < \alpha < 0$	$0 < \alpha < 1$	$\alpha > 1$	Med. α
Sim.	$44/156 = 51\%$	0.11	23	43	52	38	0.67
Fit to Sim.	$74/132 = 56\%$	0.16	17	60	34	21	-0.29

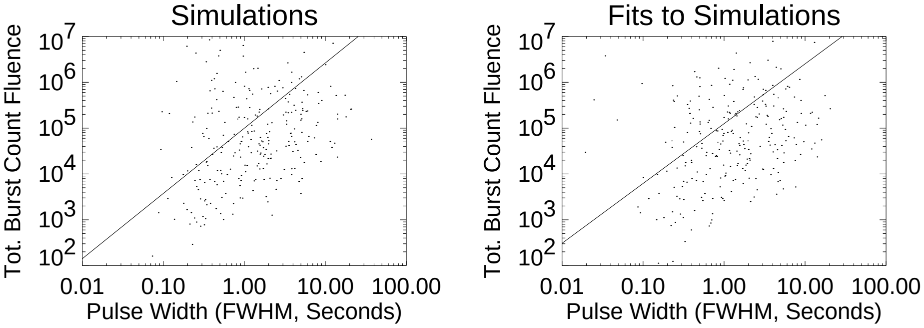

Figure 6.18: Total count fluence versus pulse width (FWHM) of highest amplitude pulse in each fit.

6.8 Correlations Between Count Fluences and Timescales

Since the simulated bursts were generated with no correlations between pulse width and pulse amplitude, they have a positive correlation between pulse width and pulse count fluence.

When we compare the pulse width of the highest amplitude pulse in each burst with total burst count fluence (Figure 6.18 and Table 6.19), we see that the positive correlation appears somewhat stronger in the fits to simulations than in the simulations.

Table 6.19: Correlation Between Total Count Fluence and Pulse Width (FWHM) of Highest Amplitude Pulse in Each Fit.

	r_s	Prob.	β
Simulation	0.23	8.9×10^{-5}	1.42 ± 0.18
Fit to Sim.	0.33	1.3×10^{-8}	1.30 ± 0.17

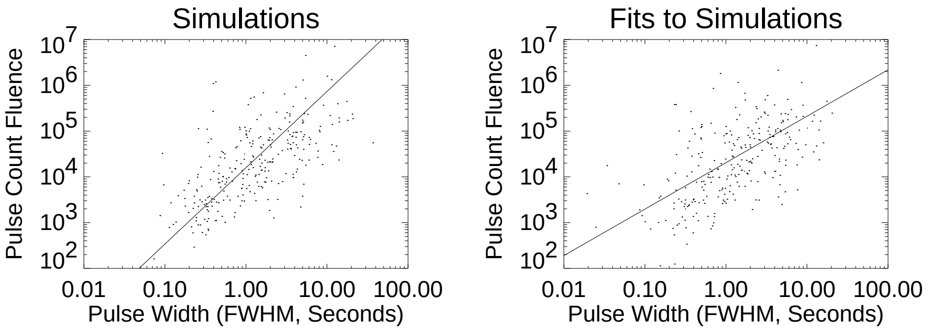

Figure 6.19: Pulse count fluence versus pulse width (FWHM) of highest amplitude pulse in each fit.

Table 6.20: Correlation Between Pulse Count Fluence and Pulse Width (FWHM) of Highest Amplitude Pulse in Each Fit.

	r_s	Prob.	β
Simulation	0.63	2.6×10^{-33}	1.67 ± 0.10
Fit to Sim.	0.61	5.8×10^{-30}	1.01 ± 0.02

On the other hand, when we compare the pulse width with the pulse count fluence of the highest amplitude pulse in each burst (Figure 6.19 and Table 6.20), we see that the positive correlation appears slightly weaker in the fits to simulations than in the simulations.

We see a similar result when we compare the pulse width with the pulse count fluence of all pulses in all bursts combined (Figure 6.20 and Table 6.21); the positive correlation is slightly weaker in the fits to simulations than in the simulations.

Table 6.22 shows the correlations between pulse width and pulse count fluence within individual bursts. It shows that the vast majority of simulated bursts show a positive correlation, as expected. In the fits to the simulations, somewhat fewer bursts show a

Table 6.21: Correlation Between Count Fluence and Pulse Width (FWHM), All Pulses in All Fits Combined.

	r_s	Prob.	β
Simulation	0.60	0	1.75 ± 0.04
Fit to Sim.	0.53	0	1.07 ± 0.03

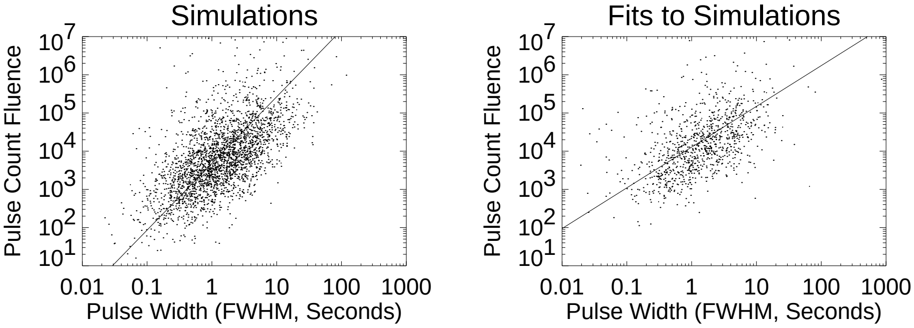

Figure 6.20: Pulse count fluence versus pulse width (FWHM), all pulses in all fits combined.

Table 6.22: Correlations Between Pulse Count Fluence and Pulse Width Within Bursts.

	% Pos. Corr.	Binom. Prob.	$\beta < -1$	$-1 < \beta < 0$	$0 < \beta < 1$	$\beta > 1$	$\frac{1}{\text{Med.}(1/\beta)}$
Sim.	$198/223 = 89\%$	$< 10^{-16}$	14	7	37	165	1.59
Fit to Sim.	$167/198 = 84\%$	$< 10^{-16}$	25	12	54	103	1.41

positive correlation between pulse count fluence and pulse width than in the simulations. In the fits to actual BATSE data, the majority of bursts showed positive correlations between pulse width and pulse count fluence within bursts. It appears that the observed result has probably been weakened by selection effects in the pulse-fitting procedure.

Figure 6.21 shows that there are no significant correlations between the errors in the fitted count fluences and the fitted pulse widths for simulated bursts consisting of a single pulse in both the simulation and the fit. Therefore, the uncorrelated errors in the pulse count fluences and pulse widths would tend to smear out any existing correlations rather than to create correlations, which is what we have seen above.

Figure 6.22 shows the total burst count fluence versus the intervals between the peak times of the two highest amplitude pulses in each burst, *for the simulated bursts with multiple pulses and where no pulses in the simulation were truncated by the* 2^{20}. It shows that these distributions are also very similar for the simulated bursts and for the fits to the simulations, although the fits to simulations tend to miss points when the intervals between the two highest amplitude pulses are small. Table 6.23 shows the correlations between the total burst count fluence and the intervals between the two highest amplitude pulses, for

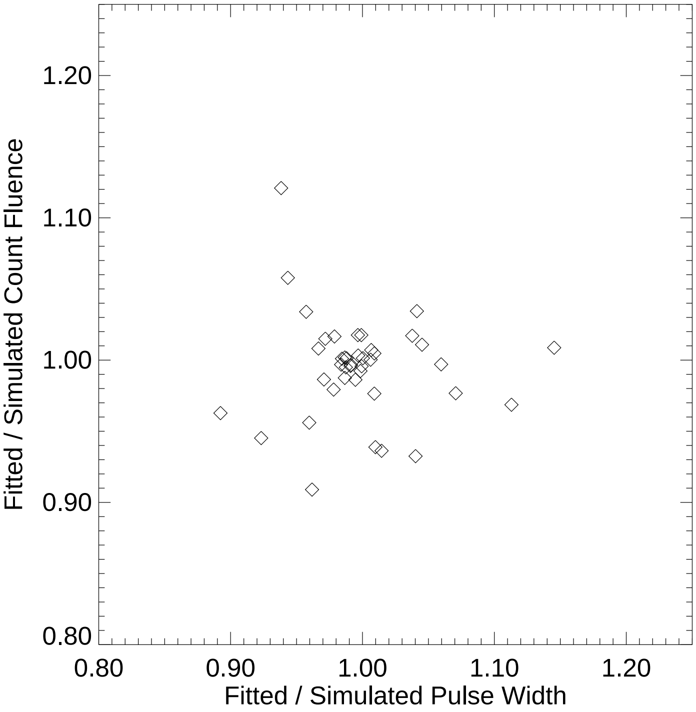

Figure 6.21: Ratios of fitted to simulated pulse count fluences versus ratios of fitted to simulated pulse widths for single-pulse simulated bursts.

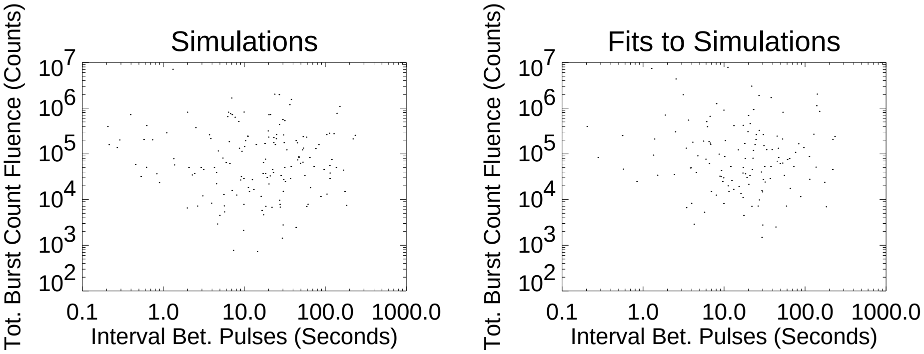

Figure 6.22: Total count fluence versus interval between two highest pulses in each fit.

Table 6.23: Correlation Between Total Count Fluence and Interval Between Two Highest Pulses in Each Fit.

	r_s	Prob.
Simulation	-0.04	0.59
Fit to Sim.	-0.06	0.51

the same simulated bursts. It also shows no significant correlation for either the simulations or the fits to the simulations.

6.9 Correlations Between Pulse Amplitudes and Count Fluences

The simulated bursts were also generated with a positive correlation between pulse amplitude and pulse count fluence. It appears that selection effects in the pulse-fitting procedure

Table 6.24: Correlations Between Pulse Count Fluence and Intervals Between Pulses Within Bursts.

	% Pos. Corr.	Binom. Prob.	$\beta < -1$	$-1 < \beta < 0$	$0 < \beta < 1$	$\beta > 1$	$\frac{1}{\text{Med.}(1/\beta)}$
Sim.	$71.5/156 = 46\%$	0.30	57	13	18	68	4.1
Fit to Sim.	$63/132 = 48\%$	0.60	45	18	17	52	34

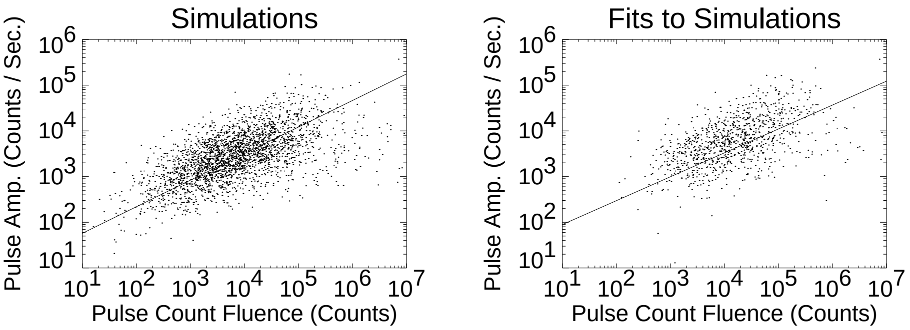

Figure 6.23: Pulse amplitude versus pulse count fluence, all pulses in all fits combined.

Table 6.25: Correlation Between Pulse Amplitude and Pulse Count Fluence, All Pulses in All Fits Combined.

	r_s	Prob.	γ
Simulation	0.59	0	0.58 ± 0.01
Fit to Sim.	0.51	0	0.52 ± 0.06

tend to weaken these positive correlations when we compare the simulations with the fits to the simulations.

Table 6.22 shows the correlations between pulse amplitude and pulse count fluence within individual bursts. It shows that a large majority of simulated bursts show a positive correlation, as expected. In the fits to the simulations, fewer bursts show a positive correlation between pulse amplitude and pulse count fluence than in the simulations. In the fits to actual BATSE data, the majority of bursts showed positive correlations between pulse amplitude and pulse count fluence within bursts. It appears that the observed result has probably been weakened by selection effects in the pulse-fitting procedure.

Figure 6.26 shows an apparent positive correlation between the errors in the fitted pulse

Table 6.26: Correlation Between Pulse Amplitude and Pulse Count Fluence, Highest Amplitude Pulse in Each Fit.

	r_s	Prob.	γ
Simulation	0.57	3.0×10^{-26}	0.60 ± 0.04
Fit to Sim.	0.58	7.5×10^{-27}	0.57 ± 0.15

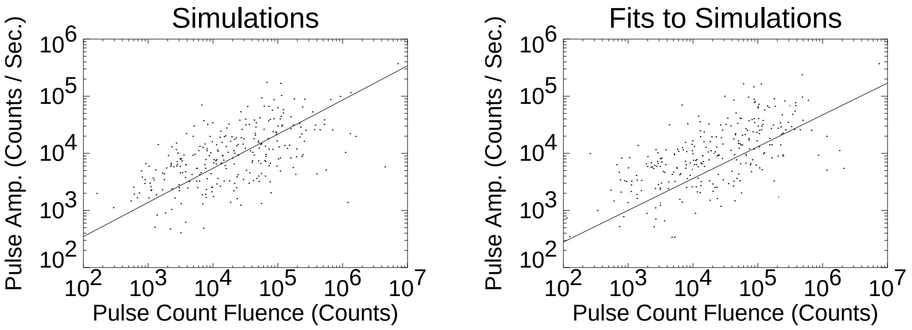

Figure 6.24: Pulse amplitude versus pulse count fluence, highest amplitude pulse in each fit.

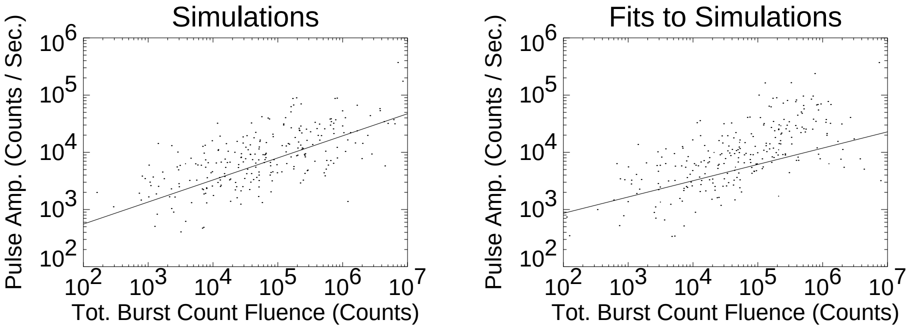

Figure 6.25: Amplitude of highest amplitude pulse versus total count fluence in each fit.

Table 6.27: Correlation Between Amplitude of Highest Amplitude Pulse and Total Count Fluence in Each Fit.

	r_s	Prob.	γ
Simulation	0.65	4.4×10^{-36}	0.39 ± 0.03
Fit to Sim.	0.61	8.9×10^{-31}	0.28 ± 0.06

Table 6.28: Correlations Between Pulse Amplitude and Pulse Count Fluence Within Bursts.

	% Pos. Corr.	Binom. Prob.	$\gamma < -1$	$-1 < \gamma < 0$	$0 < \gamma < 1$	$\gamma > 1$	Med. γ
Sim.	$185/223 = 83\%$	$< 10^{-16}$	11	24	172	16	0.34
Fit to Sim.	$142.5/198 = 72\%$	$< 10^{-16}$	15	40	121	18	0.20

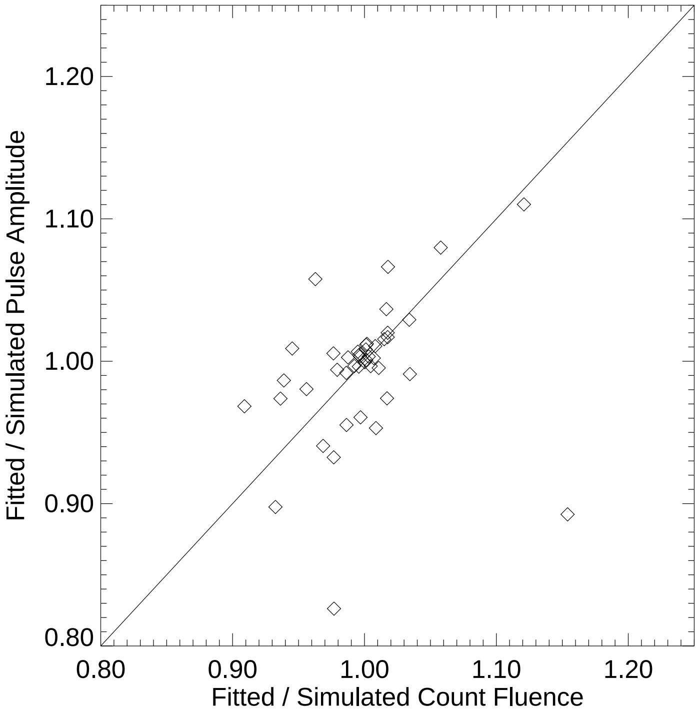

Figure 6.26: Ratios of fitted to simulated pulse amplitudes versus ratios of fitted to simulated pulse count fluences, with line of constant pulse width, for single-pulse simulated bursts.

amplitudes and fitted count fluences for simulated bursts consisting of a single pulse in both the simulation and the fit. However, the Spearman rank-order correlation coefficient shows no significant correlation between the two sets of errors. Therefore, the uncorrelated errors in the pulse amplitudes and pulse count fluences would tend to smear out any existing correlations rather than to create correlations, which is what we have seen above.

Chapter 7

Discussion

Decomposing burst time profiles into a superposition of discrete pulses gives a compact representation that appears to contain their important features, so this seems to be a useful approach for analyzing their characteristics. The pulse decomposition analysis confirms a number of previously reported properties of gamma-ray burst time profiles, for a larger sample of bursts and using data that generally has finer time resolution than in prior studies. These properties include tendencies for the individual pulses comprising bursts to have shorter rise times than decay times, for the pulses to have shorter durations at higher energies, and for the pulses to peak earlier at higher energies, which is sometimes described as a hard-to-soft spectral evolution of individual pulses.

The BATSE TTS data, although more difficult to use with many common mathematical and statistical methods, usually has finer time resolution in the peaks of bursts than the binned BATSE data with the finest time resolution, the MER data. It usually has finer time resolution at background rates than the finest time resolution binned BATSE data that can cover the entire durations of long bursts, the combined PREB and DISCSC data. This makes the TTS data valuable for studies that are interested in short timescale features of burst time profiles.

Pulse rise times tend to decrease during the course of a burst, while pulse decay times tend to increase. When examining pulse widths, or durations, these two effects nearly balance each other; pulse widths have a slight tendency to decrease during the course of a burst which appears to be statistically insignificant. The ratios of pulse rise times to decay times tend to decrease during the course of a burst. The evolution of pulse asymmetry ratios does not arise from selection effects in the pulse-fitting procedure, so it is most likely intrinsic to the bursters.

No other pulse characteristics show any time evolution within bursts, although it is possible that there is non-monotonic evolution; for example, a pulse characteristic may tend to be greater at the beginning and end of a burst and smaller in the middle, and the tests used here wouldn't be sensitive to this. In particular, it doesn't appear that either pulse amplitudes or pulse count fluences have any tendency to increase or decrease during the course of a burst. Also, later pulses in a burst don't tend to be spectrally harder or softer than earlier pulses, although there is spectral softening *within* most pulses.

The spectra of pulses within a burst also don't appear to be harder or softer for stronger or weaker pulses, or for longer or shorter duration pulses.

If we take the peak luminosities of bursts to be a standard candle, then the peak fluxes will be good distance measures. We then find that the highest pulse amplitude within a burst has inverse correlations with two different timescales, the width of the highest amplitude pulse and the time interval between the two highest amplitude pulses. The former correlation, between pulse amplitude and pulse width, is not consistent with purely cosmological effects, but must be at least partially influenced by non-cosmological effects. These non-cosmological effects may include intrinsic properties of the bursters, or selection effects of the BATSE trigger criteria, but do not include selection effects of the pulse-fitting procedure. The latter correlation, between pulse amplitude and time intervals between pulses, may be less influenced by non-cosmological effects. The inverse correlation observed between pulse amplitude and pulse width within bursts result in part from selection effects in the pulse-fitting procedure, but also appear to result in part from intrinsic properties of the bursters.

If we take the integrated luminosity of bursts to be a standard candle, then the fluences will be good distance measures. We then find a positive correlation between the total burst count fluence and the width of the highest amplitude pulse, and no correlation with the time interval between the two highest amplitude pulses. The former correlation requires that non-cosmological effects are stronger than any cosmological effects. This is supported by the positive correlation between pulse amplitude and pulse count fluence within bursts. It is not clear why the burst count fluence and time intervals between pulses are uncorrelated.

It is natural to expect that the peak flux of bursts and the total count fluence of bursts should both decrease as the distance to the bursters increase, for any measure of distance, which would also suggest that the peak flux of bursts and the total count fluence of bursts should have positive correlations with each other. Strangely, the highest pulse amplitude and the total count fluence of bursts appear to have no statistically significant correlation with each other, implying that the two measures of brightness cannot both be good standard candles, though it is possible that one is a good measure of distance, or that both are poor measures of distance.

There don't appear to be any statistically significant correlations between pulse amplitude and pulse asymmetry, whether the comparison is of all pulses in all fits combined, of only the highest pulse in each fit, of only the single-pulse fits, or of different pulses within multiple-pulse fits. This implies that the differences between the variations of pulse rise time with pulse amplitude, and the variations of pulse decay time with pulse amplitude are statistically insignificant, and both rise times and decay times tend to decrease as pulse amplitude increases.

In future studies using the BATSE Time-to-Spill data, it may be useful to concatenate the pre-trigger portion of the BATSE time-tagged event (TTE) data to the TTS data. This is most useful for short bursts, where the "pre-burst" portion of the burst can be a significant fraction of the total duration. The TTE data is easily used for this because one can use the arrival times of every 64^{th} count to create data with characteristics identical to those of the TTS data. The spill number domain wavelet denoising procedure described in Chapter 3.1 would require modification because the number of spills would no longer be a power of 2 after the pre-burst TTE data is prepended to the TTS data, but in most cases it should be sufficient to simply truncate the combined data at 16,384 spills because the original 242 second accumulation period for transient events used by BATSE nearly always ends before this many spills are accumulated, and nearly all gamma-ray bursts end long before this 242 second accumulation period ends. (The accumulation period was later increased to 573 seconds primarily for observing solar flares.)

The wavelet denoising procedure used here to smooth burst time profiles is based on the procedure of Donoho [55] for denoising binned Poisson events. Kolaczyk [96] has found a better wavelet denoising procedure for binned Poisson data which uses scale-dependent thresholds. It may be possible to adapt this procedure to the TTS data, which obeys the gamma distribution rather than the Poisson distribution. Another possible method for smoothing burst time profiles is Scargle's Bayesian block method, which has been developed for spill data such as the BATSE TTS data as well as for time-tagged events such as the BATSE TTE data or data binned in equal time intervals.[24, 97]

For comparing pulse characteristics between energy channels, it would be useful to manually match individual pulses between energy channels, rather than to use the simple automatic procedure used here. Manually matching pulses will be far more time-consuming than the automatic matching procedure, but should still be far less time-consuming than the pulse-fitting procedure, assuming a suitable user interface. A greater challenge is designing the user interface for displaying burst time profiles in different energy channels and controlling the portions of the time profiles to be displayed, and for selecting the pulses to be matched between energy channels, as well as designing data structures for storing the pulse correspondences in a useful and efficient manner.

Appendix A

BATSE Data Types for Triggered Events

A.1 BATSE IBDB Data

BATSE collects several *Individual Burst Database* (IBDB) data types for all triggered events, including but not limited to gamma-ray bursts. The general properties of these data types are summarized in Tables A.1, A.2, and A.3. All of the data types, except for the time-tagged event (TTE) and time-to-spill (TTS) data types, contain binned counts from the burst-selected detectors, also called the on-burst detectors. Data with four energy channels use discriminator counts, while those with 16, 128 (LAD), or 256 (SD) energy channels use counts from the pulse-height analyzers. Due to the limited on-board memory, 128 channel LAD spectra and 256 channel SD spectra are accumulated over long time intervals, and shorter accumulations with correspondingly finer time resolution are taken with 16 and four channel data.[45]

A.2 FITS Files

The BATSE IBDB data for all events, GRB and non-GRB, that triggered through the end of the 4B burst catalog have been made publicly available on the Internet via anonymous FTP, and new bursts are now added to the FTP site periodically. The data are contained in FITS (Flexible Image Transport System) files, a standard for exchanging astronomical and

Table A.1: BATSE IBDB Spacecraft and Instrument Information Data Types

IBDB Data Type	Description
INFO_BDAS	Threshold and background rates.
INFO_CAL	Gain / resolution information.
INFO_CAL2	Calibration information.
INFO_GRO	Spacecraft position data.

astrophysical data between computer systems that can differ widely in their internal data formats.[98] Every FITS file begins with a *primary header*, consisting of 80-byte records of ASCII text describing the format and contents of the file, its origin, and optionally other information. This may be followed by a primary data area that can contain a two-dimensional image, which is the original reason for the *Image* in the name. FITS files may also contain one or more extensions, each beginning with an *extension header*, also consisting of 80-byte records of ASCII text describing the extension type, the format and contents of the extension, and other information, with a data area following the header. One commonly used FITS extension is the *binary table extension*, which is a two-dimensional array of binary data. The data area consists of fixed format records, where each field may contain logical values, bit arrays, binary integers, real or complex IEEE floating-point numbers, ASCII character strings, or arrays of any of the previous objects. The type and length of each field, and a name, is given in the extension header. There are publicly available routines for reading various kinds of data in FITS files, including the binary table extensions, in FORTRAN, C, IDL, and other computer programming languages.

The IBDB data for a burst or other transient event consist of up to 29 files, and includes both the transient event data types and the continuously collected data types collected during the burst accumulation period. The data are stored in packets in a single binary table extension, in largely the same format that the CGRO spacecraft originally transmitted it in, but divided into the separate FITS files according to the different data types, with the FITS primary and binary table extension headers attached to each file partially describing the data format. The BATSE IBDB FITS files have no primary images. The various data types have formats that bear little resemblance to each other, and after using standard FITS file reading routines, additional processing is required to convert the data into a useful

Table A.2: BATSE IBDB Science Data Types for Large-Area Detectors

IBDB Data Type	LADs	Energy Channels	Time Resolution	Description
CONT	All 8	16	2 sec.	Continuous data. Taken at all times, not only during the burst. Not FITS compliant.
DISCLA	All 8	6: 4 + NaI, CPD	1 sec.	Discriminator counts. Also taken at all times. Not FITS compliant.
DISCSC	On-burst	4	64 ms	Discriminator counts, Summed over on-burst LADs.
HER	4, 1 per file	128	5 min.	High Energy Resolution. Also taken at all times. Spectra accumulated in 16-bit words, which may overflow.
HER_COR	4	128	5 min.	HER data, with (imperfect) corrections on ground for overflows. One file per LAD.
HERB	4	128	Multiples of 64 ms	High Energy Resolution during Burst, at higher time resolution. 128 spectra.
MER	4	16	16 ms / 64 ms	Medium Energy Resolution. 16 ms resolution for first 32.768 seconds after trigger (2048 accumulations), 64 ms resolution for next 131.072 seconds (2048 accumulations).
PREB	All 8	4	64 ms	Preburst discriminator rates for 2.048 seconds before burst trigger (32 accumulations).
TTE	All 8 / On-burst	4	2 μs	Time-Tagged Event. Arrival times of last 8192 counts (all detectors) before and first 24,576 counts (on-burst detectors) after burst trigger.
TTS	On-burst	4	1–128 μs	Time-To-Spill. Times to accumulate 16, 64, or 256 counts in a LAD discriminator channel, with 1 μs time resolution for 1–127 μs accumulation times, increasing to a maximum of 128 μs time resolution for 9600–140,672 μs accumulation times. 16,384 accumulations per channel.

Table A.3: BATSE IBDB Science Data Types for Spectroscopy Detectors

IBDB Data Type	SDs	Energy Channels	Time Resolution	Description
DISCSP	All 8	4	1 sec.	Spectral version of DISCLA. Taken at all times. Not FITS compliant.
SHER	4, 1 per file	256	5 min.	Spectral version of HER. Also taken at all times.
SHER_COR	4	256	5 min.	Spectral version of SHER_COR. One file per SD.
SHERB	4	256	Multiples of 64 ms	Spectral version of HERB. 64 spectra.
STTE	Pulsar-Selected / On-burst	256	128 μs	Spectral Time-Tagged Event. Arrival times of last 16,384 counts (pulsar-selected detectors) before, and first 49,152 counts (on-burst detectors) after burst trigger.

form, *e.g.*, extracting bit fields representing times in some data types. More importantly, the BATSE IBDB FITS files often have missing packets due to telemetry gaps, or packets that are out of order, both of which must be determined by checking the packet sequence numbers. The *BATSE Flight Software User's Manual* [45] is an essential reference when using the BATSE IBDB data.

The TTE, STTE, and TTS formats offer the highest time resolution, but many data analysis techniques are designed for binned data and cannot be directly used for these data types, and the TTE and STTE formats will often cover only the first part of a moderately bright or long burst. The CONT, DISCLA, and DISCSP data types do not comply with the FITS binary table extension standard because they have non-standard headers, so they cannot be read by many standard FITS reading routines, including the IDL Astronomical User Library routines that I have been using. I have written routines in IDL to read all of the FITS-compliant IBDB file formats and extract the data into a useful form.

The binned data types store counts binned in equal time intervals, usually in 16-bit unsigned integers. For strong bursts, these numbers can overflow. The HER_COR and SHER_COR data types are created on the ground from the HER and SHER data types, respectively, to attempt to correct for these overflows. These corrections are described as being imperfect. The DISCSC data type also overflows, with the 16-bit numbers sometimes wrapping around more than once. No "corrected" data types have been released for the DISCSC data, or for any of the other binned data types.

The DISCLA data type contains LAD discriminator counts for the four energy channels, as well as a channel containing LAD discriminator counts summed over all four energy channels, and counts for the charged particle detector, binned in 1.024 second intervals separately for each LAD.

The preburst (PREB) data type is continuously accumulated in a ring buffer that stores 32 bins of 2.048 seconds each, separately for each of the 8 LADs. It stops accumulating when an event is triggered, so it contains the last 65.536 seconds before the trigger. It can be easily combined with the DISCSC data by summing over the burst-selected detectors to give 64 ms discriminator data that begins before the trigger and covers the entire event.

The time-tagged event (TTE) data contain the arrival times of the first 32,768 individual counts from the LADs, with a 2 μs time resolution, and the detector number and discriminator energy channel number for each count. The first quarter of the data, containing 8192 counts, comes from counts that are continuously accumulated in a ring buffer until an event is triggered, so it contains counts from all eight LADs before the trigger. The remaining 24,576 counts are accumulated after the trigger only from the burst-selected detectors.

The STTE data contain up to 65,536 arrival times of individual counts from the SDs, with a 128 μs time resolution, and the detector number and the energy channel number from the 256-channel pulse-height analyzer. The STTE counts are grouped into four blocks of 16,384 counts, corresponding to the physical memory boards used to store them. The data for each board also includes the start times for accumulating counts in that board. The first board contains counts from before the burst trigger, for the detectors selected for spectroscopy pulsar data. The other three boards contain counts collected after the trigger from the burst-selected detectors. Since the time is store as a 5-bit number and rolls over every 4.096 ms, a coarse time word is inserted into the data if 4.096 seconds passes without a count, so that the arrival time of the next count can be calculated. The total number of counts and coarse time words is 65,536, since 128 KB is allocated to STTE data on BATSE.

The Time-to-Spill (TTS) data contain up to 16,384 spill times for counts from the burst-selected LADs in each of the four discriminator energy channels. The spill times are the times needed to accumulate a fixed number of counts, which can be set in software to 16, 64, or 256 counts, though all TTS data appears to have been collected using 64-count spills. (Spills of one count would be individual time-tagged events.) The spill times are measured since the last spill, and can range from 1 to 140,672 μs, but are encoded in 11 bits using a discretization that ranges from 1 μs for the shortest spill times to 128μs for the longest spill times, shown in Table A.4. For spill times greater than 50 microseconds, the discretization error is always less than 2% of the spill time, which is less than the statistical error associated with individual spill events. The TTS data also contains a synchronization bit that changes state every 1.048576 seconds ($2^{20}\mu$s), which is can be used to maintain synchronization with Universal Time. When transient event data accumulation ends, the remainder of the TTS memory buffers for each channel are unchanged, so they will contain spill events from previous transient events.

The IBDB data types may contain gaps. Many of these occurred after the CGRO tape records began developing problems, and before they were abandoned, because some of the data was unrecoverably lost. These can be identified from the packet sequence numbers that are stored in the data. For most data types, these numbers normally increment from

Table A.4: Time-to-Spill (TTS) Time Encoding

Spill Times	Time Spanned	Discretization	Encoded As	No. of Values
1–127 μs	127 μs	1 μs	1–127	127
128–383 μs	256 μs	2 μs	128–255	128
384–1407 μs	1024 μs	4 μs	256–511	256
1408–9599 μs	8192 μs	16 μs	512–1023	512
9600–140671 μs	131072 μs	128 μs	1024–2047	1024
>140671 μs	N/A	N/A	0	1

1 to 128, then wrap around again, but the range is 1 to 32 for the MER data type, and all packet sequence numbers are 1 for the DISCSC data type. When data are missing, entire packets are dropped, and the packet sequence numbers will not be consecutive. With binned data types, the absolute times of bins after data gaps can be determined from the packet sequence numbers and the known accumulation intervals. With the TTE, STTE, and TTS data types, there is no way to directly determine the time spanned by a data gap directly from the data, since the packets span variable time intervals. For the TTE data, if a data gap occurs before the trigger, then event times before the gap are uncalculable, and if a data gap occurs after the trigger, then event times after the gap are uncalculable. If a data gap includes the trigger time, then it is impossible to determine the absolute time for any of the TTE data for that event. For the STTE data, when there is a data gap, all event times from that particular memory board after the gap are uncalculable. For the TTS data, the times of all spills after a data gap are uncalculable.

A.3 BATSE BFITS Data

Some of the BATSE burst data has been distributed on two sets of CD-ROMs, using different file formats from the IBDB data. The first set, consisting of two CD-ROMs, contains data for the GRBs in the 2B catalog in *BFITS* format.[99] The second set, consisting of three CD-ROMs, contains data for the GRB's in the 4B catalog that occurred after the end of the 2B catalog in BFITS format, as well as another format described below.[100] The *BFITS* files contain data that have been converted into a more convenient and uniform format

Table A.5: BATSE BFITS Data Types

BFITS Data Type	2B CD-ROM Filename Prefix	Input IBDB Data Types
DISCSC	SC	DISCLA, DISCSC, PREB
HER	Hd (d is detector number)	HER (and HER_COR), HERB
MER	MR	CONT, MER
SHER	Sd (d is detector number)	SHER (and SHER_COR), SHERB
TTE	TT	DISCLA, DISCSC, PREB, TTE (binned to 5 ms)

than in the original IBDB FITS files. The BFITS data for a burst consists of up to 11 files. Each BFITS file is a FITS file with no primary image, and *two* binary table extensions. The first binary table extension contains energy channel calibration information, *i.e.*, the energy edges of each energy channel for each detector. The second contains count rates for variable width bins, with errors calculated from Poisson statistics, and the time edges of each bin. The BFITS files are in a format that require very little additional processing after being read using standard FITS binary table extension reading routines. The BFITS format can only accomodate binned data, so the TTE data are binned in 5 ms bins, and the STTE and TTS data aren't included at all. Additional BFITS files contain the detector response matrices (DRMs), which describe the energy response of the detectors. The energy recorded by the detectors may differ from the actual gamma-ray energy due to scattering from the spacecraft or the earth's atmosphere. Since the release of the 2B Catalog CD-ROMs, the BFITS files have also been available on the FTP site `cossc.gsfc.nasa.gov`, where the IBDB FITS data is also available, and they are now available for all transient events for which IBDB FITS data is available. The details of the various BFITS data types are summarized in Table A.5.

A.4 Other BATSE Data Formats

The BATSE 4B Catalog CD-ROMs also contain the TTE and STTE data in another format for the bursts in the 4B catalog that occurred after the end of the 2B catalog. This format is a FITS file with two binary table extensions. The first binary table extension contains energy channel calibration information, in the same format as in the BFITS files. The second binary table extension contains lists of arrival times and energy channel numbers for individual counts, separated into rows by detector number. This data is also available on the FTP site.

The FTP site also has data in three ASCII text formats. One data format contains binned discriminator data with 64 ms time resolution, derived from the DISCLA, PREB, and DISCSC IBDB data types. The PREB and DISCSC data for the trigger are concatenated, and to ensure coverage of the entire burst as well as sufficient background before and after the burst, portions of the DISCLA data are added. Since the DISCLA data have 1.024 second time resolution, the binned counts are distributed uniformly among 16 bins of 64 ms each to match the binning of the PREB and DISCSC data. Another data format contains background-subtracted data and fitted backgrounds with 2.048 second time resolution, derived from CONT IBDB data, for bursts up through trigger number 3193 without "serious data gaps near trigger time". The third ASCII data format contains lists of arrival times of individual counts from the TTE IBDB data for short bursts up through trigger number 3774. The TTE data for the same short bursts are also available on the FTP site in the original IBDB format, without the FITS header attached.

Appendix B

Wavelets

A function $f(t)$ defined on an interval of the real numbers can be considered to be the sum of Dirac delta functions at every point t with amplitude $f(t)$. This trivial decomposition exists and is unique for every function because the Dirac delta functions form a complete and orthogonal basis for functions on the real numbers. There are infinitely many other families of functions that also form complete and orthogonal bases for real functions.

The most familiar such basis to scientists is the Fourier basis, which is composed of trigonometric functions that have frequencies that are integer multiples of a fundamental frequency, and have two phases, differing by 90°, at each frequency. It is useful for several reasons. One is that the frequencies frequently have a clear physical interpretation; for example, when the function being analyzed is the wave function of a particle, the frequencies correspond to momenta. The Fourier decomposition of a function is frequently known as its *frequency domain* or *momentum space* representation, while the usual representation in terms of Dirac delta functions at every point is known as its *time domain* or *position space* representation. Another reason why the Fourier basis is often useful is that when the function being analyzed is periodic, its Fourier representation is often much more compact that its position space representation.

For functions that are non-periodic, Fourier analysis is often not so useful. Since the trigonometric functions are non-zero almost everywhere, Fourier analysis may be even less useful for functions that are localized in position space. An alternative method for representing functions that may be non-periodic or localized *wavelet analysis.*[101, 102, 103] The history of wavelet analysis dates back to the development of the Haar system in 1909,

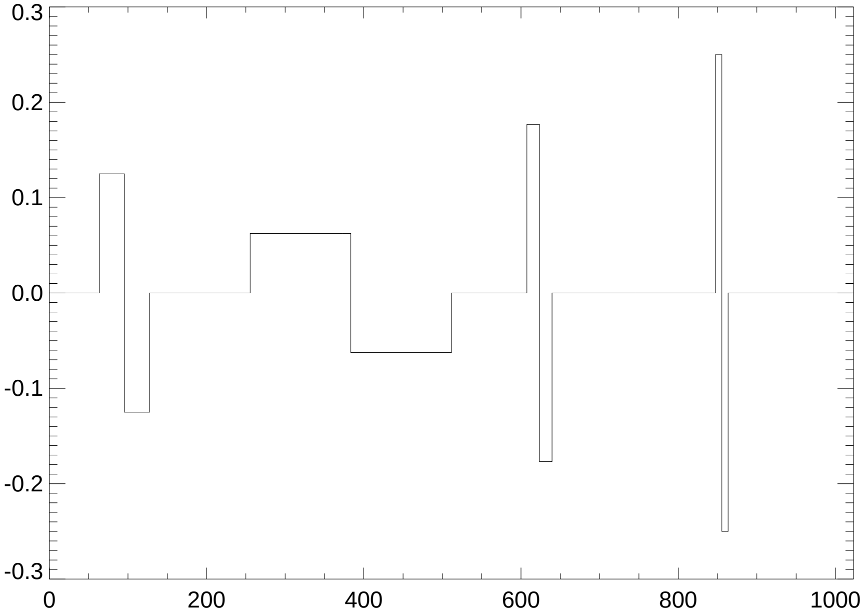

Figure B.1: Sample Haar basis wavelets.

but most work in this area began in 1985.[104] There are infinitely many different wavelet families, but they all share the characteristic that the individual wavelets in any wavelet basis are localized in both position space and frequency space. Since wavelets are localized in position space, they cannot be *perfectly* localized in frequency space, by a general result of Fourier analysis which has as another consequence the Heisenberg uncertainty principle.

A complete basis of wavelets is constructed from a *mother wavelet* by taking dilations and translations of the mother wavelet by integer powers of 2. The simplest is the *Haar* wavelet, which represents a simple differencing operator. Its mother wavelet is given by

$$\psi(x) = \begin{cases} 1, & 0 \leq x < \frac{1}{2}, \\ -1, & \frac{1}{2} \leq x < 1, \\ 0, & x < 0 \text{ or } x \geq 1. \end{cases} \tag{B.1}$$

Figure B.1 shows some basis wavelets that have been constructed from this mother wavelet. These are given by

$$\psi_{jk}(x) = 2^{j/2}\psi(2^j x - k) \tag{B.2}$$

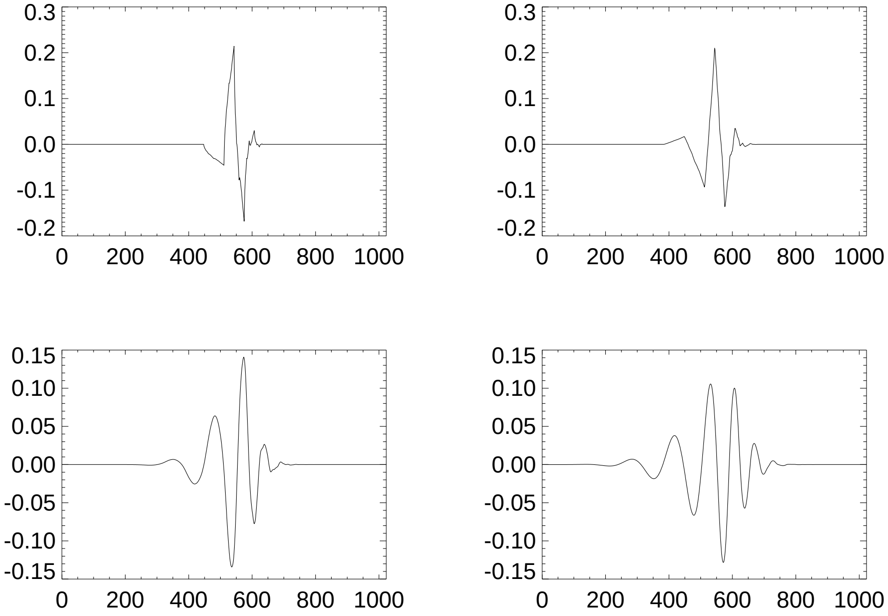

Figure B.2: Sample Daubechies 4, 6, 12, and 20 coefficient basis wavelets.

where j is non-negative integer and k is an integer with $0 \leq k < 2^j$, and they are orthonormal on the unit interval $[0, 1]$. Haar wavelets are discontinuous, which may be a drawback when analyzing continuous functions. More complicated wavelets have been constructed which are continuous, and can have any desired number of continuous derivatives. A commonly used family of wavelets is the *Daubechies* family of wavelets. The simplest of these is defined by four coefficients, and is continuous, but not differentiable, everywhere. (The Haar wavelet is the only wavelet defined by two coefficients.) Daubechies wavelets constructed using more coefficients are smoother and have more oscillations. Figure B.2 shows Daubechies basis wavelets with varying numbers of coefficients.

One of the drawbacks of wavelets are that they generally do not have a simple functional form. For example, the Daubechies 4-coefficient wavelet has discontinuous derivatives at infinitely many discrete points. The lack of a simple functional form is not a problem when analyzing discrete data, because wavelet transforms can still be calculated quickly and efficiently. Wavelets also aren't solutions to any classes of differential equations, but the fact that trigonometric functions are solutions to the wave equation is of little or no importance in many Fourier analysis applications.

Physical observables are never measured at every point on an interval, since that would require an uncountably infinite number of individual measurements. In practice, physical observables are measured at a number of discretely spaced points, and their behavior between the measurement points is assumed to be continuous, smooth, or piecewise continuous or smooth. Therefore, it is useful to discuss Fourier and wavelet analysis for functions defined on discrete points on a real interval. The mathematics is far simpler when the points are uniformly spaced, yielding the familiar discrete Fourier transform and the less familiar discrete wavelet transform.

The discrete wavelet transform of a set of $N = 2^n$ data points x_i is a set of N wavelet coefficients. The original data points can be recovered by multiplying the N wavelet coefficients by the corresponding basis wavelets ψ_{jk}, and summing these products. Each coefficient represents activity at a particular position, on a particular scale. These scales increase by powers of two, and the number of positions vary inversely with the scale. For example, the discrete Haar wavelet transform of a set of 1024 data points is a set of 1024 wavelet coefficients. There are 512 coefficients giving activity on scales of two data points, at 512 different positions, 256 coefficients giving activity on scales of four data points at 256 positions, etc., until we get to a single coefficient giving the average of all 1024 data points.

One tool of Fourier analysis is the *power spectrum*, where the (absolute squared) amplitude information in a Fourier transform is used to measure the frequencies at which the signal being analyzed varies, and all phase information is discarded. In wavelet analysis, the analog of the power spectrum is called the *scalegram*, which is calculated by averaging the squared amplitudes of the wavelet coefficients over all positions for each of the discrete scales. For example, for the Haar wavelet transform of a 1024-point data set, the scalegram will have ten elements, representing the activity on scales of 2, 4, 8, 16, 32, 64, 128, 256, and 1024 points. All positional information has been discarded.

B.1 Wavelet De-Noising

When data represents a signal with noise, it is often useful to remove the noise while preserving as much of the signal as possible. The simplest way to smooth data is to apply a "boxcar" average, where each data point is replaced with the average of a fixed number of data points surrounding it. Figure B.3 shows the unsmoothed data for the first 8 and the first 32 seconds of the MER data for BATSE trigger number 105, summed over all 16 energy

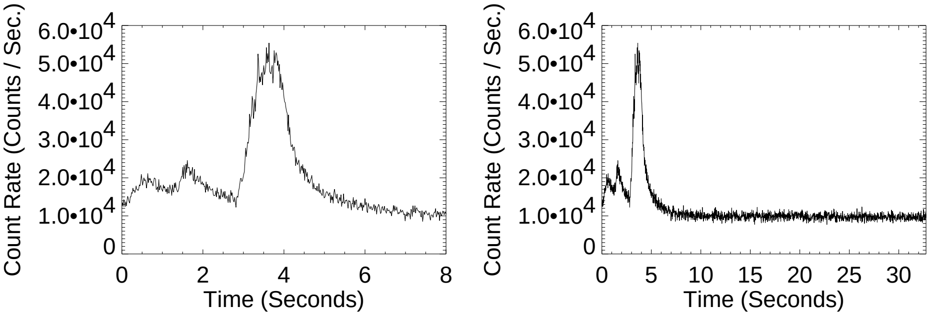

Figure B.3: BATSE Trigger Number 105, unsmoothed MER data, summed over all 16 energy channels.

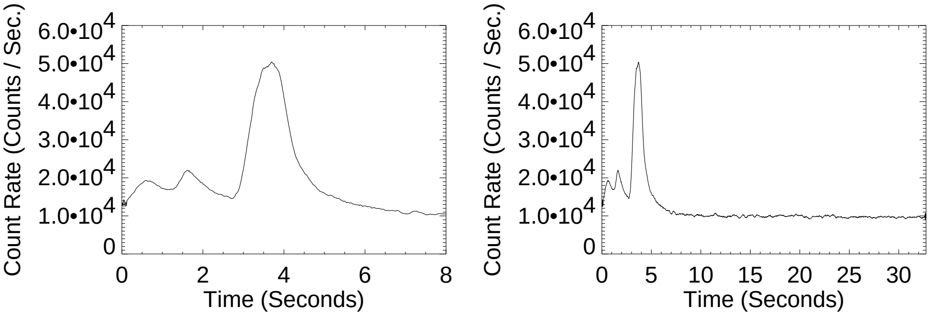

Figure B.4: BATSE Trigger Number 105, boxcar averaged MER data, summed over all 16 energy channels.

channels. The first 33 seconds of BATSE MER data is binned with 16 ms bins, for a total of 2048 data points. Figure B.4 shows the same data after applying a boxcar, average with each data point replaced by the average of the 17 data points around it. This approach has the drawback of greatly reducing all short-timescale features in the signal, such as a very short but intense spike in a burst time profile. In the example shown, the boxcar averaged data shows none of the structure that appears to be in the third pulse in the unsmoothed data.

Another method of de-noising data is to low-pass filter it, *i.e.*, take the Fourier transform of the data, remove the high frequency coefficients, and take the inverse Fourier transform of the result. This approach tends to completely remove all short-timescale features of the signal. Filtering can also introduce artifacts such as Gibbs phenomenon. This problem can be reduced by using more complex filters that are smoother in frequency space. Figure B.5

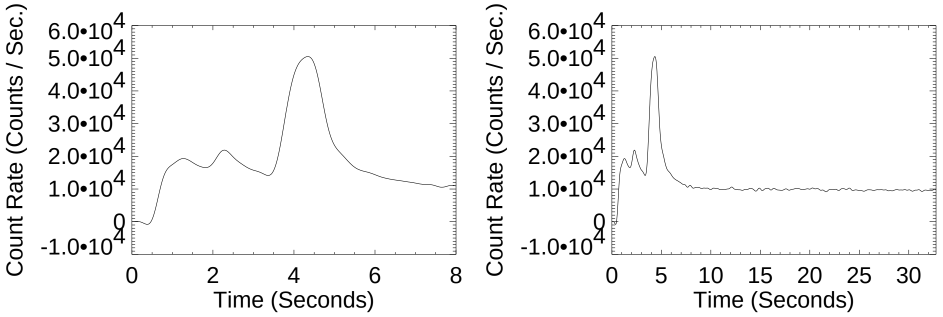

Figure B.5: BATSE Trigger Number 105, low-pass filtered MER data, summed over all 16 energy channels.

shows the same MER data for BATSE trigger number 105 after it has been low-pass filtered with an upper frequency of 1/16 of the Nyquist frequency. It is fairly similar to the boxcar averaged data, though all features are delayed in time, probably due to a phase shift at low frequencies.

Wavelet transforms can also be used to de-noise data as follows [55]: First, the data is wavelet transformed; it is decomposed into a linear combination of basis wavelets, and the coefficients for these basis wavelets comprise the wavelet transform, just as the Fourier coefficients in the Fourier transform of a signal tell how to construct the signal from trigonometric functions. Then, the wavelet transform is thresholded, *i.e.*, all coefficients smaller than a cutoff, which may be vary with scale, are set to zero. (This is *hard* thresholding. There is another form of thresholding, *soft* thresholding, where the coefficients larger than the threshold are reduced in magnitude as well.) The optimal cutoff that is independent of scale is determined by the magnitude of the noise:

$$t = \sigma\sqrt{2\log n} \tag{B.3}$$

where t is the threshold, or cutoff, σ is the magnitude of the noise, and n is the number of data points. Finally, the thresholded wavelet transform is inverse wavelet-transformed to give the de-noised signal. This method is more likely to preserve short-timescale structure than low-pass filtering, since it tends to preserve the features with the greatest area, rather than depending on the noise to have higher frequencies than the signal.

For data containing photon counts recorded in various time intervals, such as binned gamma-ray burst data, the noise is Poisson, and its magnitude varies as the square root of the number of counts. In this case, we perform the following transformation on the data *before* applying the de-noising procedure:

$$y_i = 2\sqrt{N_i + \frac{3}{8}} \tag{B.4}$$

where the N_i are the original photon counts, and the y_i are the transformed data. The Poisson noise in the N_i has now been transformed into approximately Gaussian white noise with $\sigma = 1$ in the y_i, to which the de-noising algorithm can be applied, and the transformation can then be easily inverted to yield de-noised photon count rates.

For the BATSE TTS data, the noise is a *constant fraction* $1/\sqrt{N}$, of the signal, where N is the number of individual photons per spill. The analogous transformation for this data is

$$y_i = \log T_i \tag{B.5}$$

where the T_i are the original spill times, and the y_i are the transformed data. The noise now has $\sigma \approx 1/\sqrt{N}$.

Figure B.6 shows the same MER data BATSE trigger number 105 after it has been de-noised using the Haar wavelet. The automatic thresholding procedure for binned data with Poisson noise has zeroed all but the largest 38 of the 2048 wavelet coefficients. In effect, the shape of the time profile is represented much more compactly in terms of wavelets than in the original time-domain representation or in terms of the trignometric functions used in Fourier analysis. Wavelet de-noising has also preserved more of the shape of the initial pulses than either boxcar averaging or low-pass filtering has, and it has also completely smoothed the background following the pulses. This makes it easier for an automatic pulse-finding program, for example, to find structure in the signal while ignoring the fluctuations that are apparently due to noise.

As with low-pass filtering, wavelet de-noising will introduce artifacts whose shape comes from the wavelet used. In low-pass filtering, the artifacts have the shape of trigonometric functions, and cover the entire interval. For the Haar wavelet, these artifacts are square steps, which are clearly visible in figure B.6. Depending on the nature of the data being de-noised, certain wavelets may produce better de-noised results than others. Those that produce better de-noised signals may have characteristics similar to those of the underlying signal, *e.g.*, Haar wavelets should work better than any others for data that is composed of

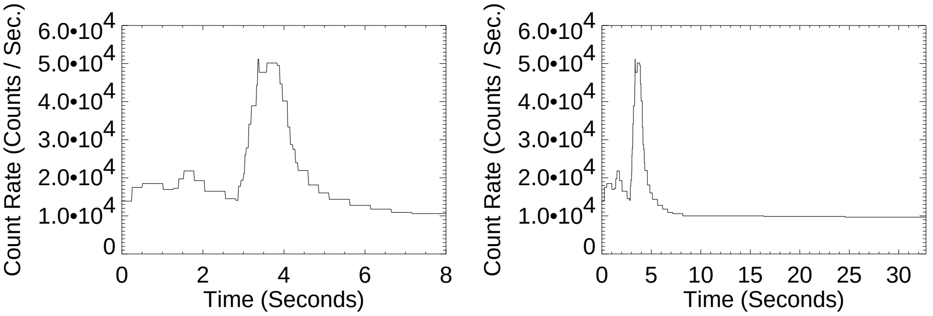

Figure B.6: BATSE Trigger Number 105, Haar wavelet de-noised MER data, summed over all 16 energy channels.

square steps. The best choice of wavelet should represent the signal as compactly as possible, while remaining as close as possible to the original data. The former can be measured by the number of non-zero coefficients remaining in the thresholded wavelet transform, and the latter could possibly be measured by the RMS deviation of the de-noised signal from the original data. On the other hand, if different wavelet types result in radically different de-noised burst profiles, then too much information is probably being lost in the de-noising process.

The pulse-fitting program uses wavelet de-noising to smooth burst time profiles to make it easier to automatically or manually identify pulses, which are then used as an initial guess for the fitting routine. For these purposes, the simplest wavelet, the Haar wavelet, was used because a single Haar basis wavelet has only one local maximum and one local minimum, making it easier for an automatic pulse-finding routine to find pulses. Since the wavelet de-noising is not used to represent the burst time profile, but only for finding an initial guess for the fitting routine, which fits to the actual data, the compactness of the wavelet representation is relatively unimportant.

Appendix C

Curve Fitting

Fitting a curve to a collection of data points is one of the most commonly performed tasks in data analysis. For simplicity, we'll discuss the situation that we have with GRB time profiles, where the data points lie in two dimensions, with the first being the independent variable, the times t_i in our case, and the second being the dependent variable, the count rates y_i in our case, and there is a statistical uncertainty associated with the dependent variable at each data point. The curve is a function of the independent variable that yields the dependent variable, $y = f(t, a_n)$, and has a finite number of parameters a_n, fewer than the number of data points. The fitting is done by finding the choice of parameters for which the curve passes as close as possible to the data points, with the degree of closeness measured in terms of the statistical uncertainties of the data points.

The statistical uncertainties can be characterized by a probability distribution, $P_i = P(y, y_i)$, which gives the probability that y is the "true" value of the measured value y_i taken at t_i. The probability of a particular fit is $P = \prod_i P_i$, and we wish to find the choice of parameters that maximizes this probability. It is usually more convenient, and mathematically equivalent, to minimize the *merit function* $-2 \log P = \sum_i (-2 \log P_i)$, which generally requires that $\frac{\partial P}{\partial a_n} = 0$. Note that the normalization of the probability is transformed to an additive constant in the merit function, and this can be ignored. This method is the *maximum likelihood* fit. If the data is generated by a process that is accurately characterized by the best fit function, *i.e.*, the best fit function is a good model for the data, then the expected value of the merit function is $N - M$, where N is the number of data points and M is the number of parameters.

Frequently, the statistical errors are Gaussian, or are assumed to be Gaussian, with standard deviation σ_i, so the probability distribution at each point is

$$P_i = \exp\left[-\frac{(y(t_i,a_n)-y_i))^2}{2\sigma_i^2}\right]. \tag{C.1}$$

Maximizing the probability of the fit is then equivalent to minimizing the merit function

$$\chi^2 = -2\log P = \sum_i \frac{(y(t_i,a_n)-y_i)^2}{\sigma_i^2}. \tag{C.2}$$

This case is the *least squares* or *chi-square* fit. Most literature on curve fitting discuss only the least squares fit, though the generalization to other probability distributions is straightforward.

It is also common for the data to follow a Poisson distribution,

$$P_i = \frac{R_i^{n_i} e^{-R_i}}{n_i!}, \tag{C.3}$$

where n_i are the observed counts and $R_i = R(t_i)$ are the fitted count rates. When we take the logarithm of the probability to obtain the merit function, the term $\log n_i!$ is independent of the fit parameters, so we can apply Stirling's asymptotic approximation to this term, $\log n! \approx n\log n - n$ without affecting the fit.[105] The merit function, which we will also denote as χ^2, then becomes

$$\chi^2 = 2\sum_i \left[(R_i - n_i) + n_i \log\frac{n_i}{R_i}\right]. \tag{C.4}$$

We could also completely drop the term $\log n!$ because n depends only on the data and not on the parameters being fitted, but using Stirling's approximation is more convenient because the merit function has a minimum value of 0 when $R_i = n_i$. This merit function approximates the least-squares merit function when the $R_i - n_i$ are small, and constrains the R_i to be nonnegative.

For the BATSE TTS data, which follows the gamma distribution, we have

$$P_i = \frac{y_i^{N-1} R_i^N e^{-R_i y_i}}{\Gamma(N)}, \tag{C.5}$$

where y_i are the observed spill times, $R_i = R(t_i)$ are the fitted event rates, and N is the number of events per spill. Again, we can apply Stirling's approximation without affecting the fit, and we find that the merit function becomes

$$\chi^2 = 2\sum_i \left[(R_i y_i - N) - N\log\frac{R_i y_i}{N}\right]. \tag{C.6}$$

This merit function also has a minimum value of 0 when $\frac{N}{y_i} = R_i$, approximates the least-squares merit function when the $\frac{N}{y_i} - R_i$ are small, and also constrains the y_i to be nonnegative.

The problem of curve fitting has become the problem of minimizing the merit function, which we'll denote as χ^2 even for non-Gaussian statistics, by varying the parameters a_n. In the case of the least squares fit where the function being fit depends linearly on the a_n, the equations $\frac{\partial \chi^2}{\partial a_n} = 0$ can be transformed into a matrix equation that expresses the vector $\mathbf{y}$ of dependent variables y_i in terms of the vector $\mathbf{a}$ of best fit parameters a_n. This equation can be solved by standard methods to directly yield the best fit parameters $\mathbf{a}$ in terms of $\mathbf{y}$. This case is sometimes known as *linear regression.*

In the general case, where the function being fit does not depend linearly on the a_n, or the statistics are non-Gaussian, we cannot solve directly for the a_n, but must instead minimize the merit function iteratively. For example, we could search on a grid in a region of parameter space where we believe the minimum lies, and then successively bracket the minimum using a binary search. Unfortunately, when the number of parameters becomes large, the number of grid points where the merit function must be evaluated at can become prohibitively large.

More sophisticated methods of minimizing the merit function use information about its shape, given by the lower order terms of a Taylor series expansion of the merit function. These begin at a point in parameter space, attempt to estimate where the minimum lies in parameter space, step to that point, and repeat until the merit function stops decreasing significantly, or fails to approach the expected value and cannot be considered a good fit. The latter could happen, for example, if the fitting routine finds a local minimum in parameter space that isn't the true minimum (best fit.)

One such method is the method of *steepest descent*, where the gradient $\nabla\chi^2(\mathbf{a})$ of χ^2 with respect to vector of parameters $\mathbf{a}$ is calculated at the present location in parameter space to estimate the direction to the minimum. The routine then takes a step in that direction to a new point in parameter space, where it repeats this process. The method works best far from the minimum, where the linear approximation to the merit function provided by the gradient is good.

Near the minimum of the merit function, the gradient becomes small, so the shape of the merit function is dominated by terms containing higher order partial derivatives than the first. The merit function is better approximated by a quadratic form, given in terms of the vector of first partial derivatives (the gradient) of the merit function and the matrix of second partial derivatives $\frac{\partial^2\chi^2}{\partial a_n \partial a_m}$ (the Hessian matrix.) The minimum of the quadratic approximation can be directly calculated, so the routine can directly step to that location in parameter space. This method works best near the minimum where the distances between the trial points and the true minimum are small, so the quadratic approximation gives the shape of the merit function accurately.

The *Levenberg-Marquardt method* uses a linear combination of these two methods, weighted towards steepest descent far from the minimum, and towards the quadratic approximation near the minimum, with the distance estimated by comparing the gradient and the Hessian matrix.[106] The standard IDL routine `CURVEFIT` implements this curve-fitting algorithm.

The pulse-fitting program uses a version of `CURVEFIT` that I have modified to use the merit function for a gamma distribution instead of the least-squares merit function used for a normal distribution. This modified curve-fitting routine is named `GAMMAFIT`.

Appendix D

Correlations and Linear Regression

D.1 The Linear Correlation Coefficient

The best known statistic for measuring correlations between two sets of variables x_i and y_i is the *linear correlation coefficient*, also known as the linear Pearson correlation coefficient, and denoted r.[107] This is given by

$$r = \frac{\sum_i (x_i - \bar{x})(y_i - \bar{y})}{\sqrt{\sum_i (x_i - \bar{x})^2}\sqrt{\sum_i (y_i - \bar{y})^2}} \tag{D.1}$$

where $\bar{x}$ and $\bar{y}$ are the mean values of the x_i and the y_i, respectively. The maximal correlation occurs when the data points (x_i, y_i) all lie on a straight line with positive or negative slope, for which $r = 1$ or $r = -1$, respectively, and for weaker correlations r takes intermediate values. For the extreme cases where all of the points lie on either the x or y axis, so that all y or x values are identical, $r = 0$. One limitation of the linear correlation coefficient is that without some knowledge of the distributions of x and y, it isn't possible to determine the statistical significance of r.

D.2 Rank Correlations

Another statistic for measuring correlations is the *Spearman rank-order correlation coefficient*, commonly denoted as r_s. This statistic is calculated in the same way that the linear correlation coefficient is calculated, except that for each data point, the numerical rank of each variable in the set of data points is used, rather than the variables themselves. Denoting the ranks of the x_i and the y_i as R_i and S_i, respectively, the smallest x_i has rank

$R_i = 1$, the next smallest has a rank of 2, and the same is done for the y_i, so that

$$r_s = \frac{\sum_i (R_i - \bar{R})(S_i - \bar{S})}{\sqrt{\sum_i (R_i - \bar{R})^2}\sqrt{\sum_i (S_i - \bar{S})^2}} \tag{D.2}$$

This statistic can have two significant advantages over the linear correlation coefficient. The first is that it is *robust*; it is less sensitive to a small number of outliers in the data set, in the same way that the median is less sensitive to outliers than the arithmetic mean. This is useful if the outliers are likely to come from bad data. The second advantage is that it is possible to calculate the statistical significance of r_s, *i.e.* the probability that a random data set of the same size with no correlation between the variables would produce the observed value of r_s. The reason why this is possible is that we know that the R_i and the S_i are distributed uniformly from 1 to N where N is the total number of data points. However, r_s is *nonparametric*; it is invariant under reparametrization of x or y, such as replacing x_i and y_i by $\log x_i$ and $\log y_i$ (because taking the ranks is a itself reparametrization that replaces other reparametrizations), and it discards all information about the distributions of x and y except for the ranks of the x_i and y_i.

Another rank correlation statistic is *Kendall's* τ, which is more nonparametric than r_s in that it uses only the *relative* ordering of the ranks of pairs of data points (x_i, y_i) and (x_j, y_j), and not the numerical values of the ranks as the r_s uses. Efron and Petrosian [108] have developed a statistic, denoted t_w, that measures correlations of truncated data sets when the truncation is known and is monotonic. This statistic is also calculated from the relative ordering of ranks, and for the untruncated case (or equivalently, when the truncation in x is independent y or vice versa) is a generalization of τ. Both Kendall's τ and t_w have the benefits that r_s has, robustness and the ability to calculated the statistical significance. I will not describe either τ or t_w further here, because I don't use them, τ because it isn't clearly any better or worse than r_s, and t_w because I don't know what truncations may exist in the fitted pulse parameters.

D.3 Linear Regression

The various correlation coefficients r, r_s, τ and t_w only indicate whether the x_i and y_i have a positive or negative correlation, and how much correlation there is. In the extreme case of total correlation, where the (x_i, y_i) all lie on a straight line (that doesn't lie along the x

or y axis), all of these coefficients will take on the values 1 or -1, but give no information on the slope of the line. In many cases, we are also interested in finding the actual trends in the data, not just whether trends exist. For total correlation, any line-fitting routine can find the parameters of the trend. When the correlation isn't total, ordinary least squares routines often produce unsatisfactory results for two reasons. One is that they only account for deviations in the dependent variable y; they are designed to fit a line $y(x) = a + bx$ to data points (x_i, y_i) by minimizing the sum of the squares of the deviations in y, $\chi^2 = \sum_i [y_i - (a + bx_i)]^2$. Another is that they implicitly assume that the data points only deviate from a straight line due to measurement errors, while in many cases, there is *intrinsic dispersion.* We can see the resulting problems by applying ordinary least squares to (x_i, y_i), and again to (y_i, x_i), where the independent and dependent variables have been interchanged. When there is no reason to consider one variable "dependent" and the other "independent", we want the same line to be fitted either way, so the two slopes should be reciprocals of each other, but they aren't. Figure D.1 shows an example of random points generated following a two-dimensional Gaussian distribution that is twice as wide along the direction $y = x$ as along the direction $y = -x$. The trend has a slope of 1, but ordinary least squares finds a shallower slope when x is the independent variable, and a steeper slope when y is the independent variable.

There are other linear regression methods that don't assume that the data points deviate from a straight line only because of measurement errors and that treat the two variables x and y symmetrically. For example, consider the formula for the linear correlation coefficient r. It is a function of only the various second moments of the distribution of (x_i, y_i) about its centroid. The matrix of the second moments of (x_i, y_i) about their centroid is commonly known as the *covariance matrix* about the mean and denoted by S, and is given by

$$S = \begin{bmatrix} \sum_i (x_i - \bar{x})^2 & \sum_i (x_i - \bar{x})(y_i - \bar{y}) \\ \sum_i (x_i - \bar{x})(y_i - \bar{y}) & \sum_i (y_i - \bar{y})^2 \end{bmatrix}. \tag{D.3}$$

The covariance matrix obviously contains more information about their distribution than the single number r does. It is symmetric, and has two principle axes, whose directions are given by the eigenvectors of S. The distribution of (x_i, y_i) clusters around the principal axis corresponding to the larger eigenvalue, and the other principal axis, corresponding to the smaller eigenvalue, is perpendicular to the first. If all points lie on a straight line, the smaller eigenvalue will be 0. When the eigenvalues are degenerate, then the distribution of

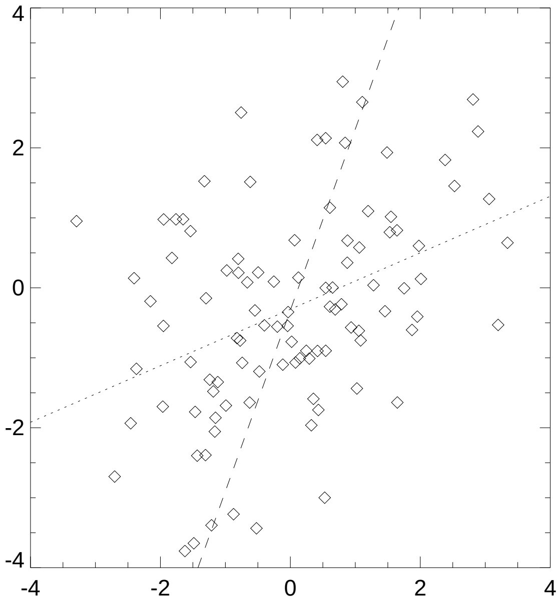

Figure D.1: Linear regression fits to a two-dimensional distribution of points. For the dotted line, x is the independent variable, and for the dashed line, y is the independent variable.

(x_i, y_i) does not cluster along any line, so there is no linear correlation. It can be verified that this case gives $S_{xy} = S_{yx} = 0$ and hence $r = 0$. It can be shown that the principal axis of S corresponding to the larger eigenvalue is also the line that minimizes the sum of the squares of the Euclidean distances to the data points (x_i, y_i), which can be shown to be

$$\chi^2 = \sum_i \frac{[y_i - (a + bx_i)]^2}{1 + b^2}, \tag{D.4}$$

This method is also known as *orthogonal regression* or *major-axis regression.*[109] We can see that ordinary least squares will always fit a line with a shallower slope than orthogonal regression, which explains the resulting fits in Figure D.1. Orthogonal regression fits are invariant under rotations. However, they are not invariant under rescalings of either x or y, as ordinary least squares fits are. This suggests that orthogonal regression is only a sensible method to use when the two variables x and y have naturally related scales, or when they have no scale, for example, when they are logarithms other quantities.

Isobe *et al.* [109] discusses and compares six different linear regression methods that have been used in astronomy, as well as other fields. Two of these are ordinary least squares (OLS), one with x as the independent variable, OLS($Y|X$), and the other with y as the independent variable, OLS($X|Y$). Another method is orthogonal regression. In addition, they discuss *OLS bisector*, where the fitted line is the angle bisector of the two OLS lines, *reduced major-axis*, where the slope of the fitted line is the geometric mean of the two OLS lines, and *OLS mean*, where the slope of the fitted line is the arithmetic mean of the two OLS lines. The three methods orthogonal regression, OLS bisector and reduced major-axis are all symmetric in x and y; the other three methods OLS($Y|X$), OLS($X|Y$) and OLS mean are not. All methods except OLS bisector and orthogonal regression are scale invariant. Only orthogonal regression is rotation invariant.

The ordinary least squares methods, OLS($Y|X$) and OLS($X|Y$), always fit lines whose slopes have the same sign, and the other four methods always fit lines whose slopes lie between those of the OLS($Y|X$) and OLS($X|Y$) lines, so that the angles corresponding to the slopes from all six methods always lie in the same quadrant of the plane. In addition, the lines fitted by all three symmetric methods OLS bisector, orthogonal regression, and reduced major-axis have slopes that are all simultaneously greater than or less than +1 (for positive slopes, -1 for negative slopes), so that the correspnding angles always lie in the same octant of the plane for these three methods. When any one of these three slopes is equal to +1 or -1, then all three slopes are equal; when any one of them is greater than +1, then all three slopes are greater than +1, etc.

When the two variables x and y have little correlation, the OLS($Y|X$) line will have a very shallow slope, and the OLS($X|Y$) line will have a very steep slope (shallow with respect to the y-axis), and the resulting OLS bisector line will have a slope near +1 or -1.

The six linear regression methods are fundamentally different and don't measure the same quantity. Any mathematical reasons for preferring one method over another must come from knowledge of the characteristics of the data being fitted, or from the questions that the fit is to answer. Isobe *et al.* recommend fitting lines using all of these methods when the nature of the scatter of the data from a straight line is not understood, and comparing the different results. They recommend the three symmetric methods when trying to determine the functional relationship between the variables. They found that when sampling points from a larger population, the deviations of the OLS bisector slopes for the samples from that for the entire population are smaller than for all other methods. Although orthogonal regression often seems more natural than the other methods because of the properties described above, it has the disadvantage that the deviations of the orthogonal regression slopes for the samples from that for the entire population are greater than for the other methods. They have implemented all of these methods in a FORTRAN procedure, `SIXLIN`, which has been ported to IDL by Wayne Landsman and is available in the IDL Astronomical Users' Library under the same procedure name.

All of these methods are sensitive to outliers in the distribution of (x_i, y_i), just as ordinary least squares algorithms are, because they are all based on least-squares merit functions. There is a *robust* alternative to ordinary least squares [63] that minimizes the sum of the absolute deviations in the dependent variable y, $M = \sum_i |y_i - (a + bx_i)|$, rather than the sum of their squares, making it less sensitive to outliers. This is implemented as in IDL as the standard routine `LADFIT`. It is straightforward to create similar robust alternatives to any of the least-squares linear regression methods. For example, a robust alternative to orthogonal regression finds the line that minimizes the sum of the Euclidean distances to the data points,

$$M = \sum_i \frac{|y_i - (a + bx_i)|}{\sqrt{1 + b^2}}, \tag{D.5}$$

rather than the sum of the squares of the distances, and it is not difficult to modify `LADFIT` to implement this. However, all of the least-squares fits can be directly calculated, while the robust absolute deviation fits must all be calculated iteratively. This occurs because the derivatives of the least-squares merit functions are continuous, while the derivatives of the absolute deviation merit functions are not. The iterative procedures for the absolute deviation fits will also sometimes find a local minimum of the merit function, rather than the global minimum, and this problem seems especially common when the total number of (x, y) points being fitted is small.

For investigating the presence of cosmological time dilation, it is desirable to use the same linear regression methods for comparing the characteristics of the highest amplitude pulses in different bursts as for comparing the characteristics of different pulses within individual bursts. When comparing pulses within bursts, the number of data points (pulses) is relatively small, so it is better to use linear regression algorithms based on least-squares merit functions. Since the fundamental relationship between the different pulse characteristics is unknown and there is no natural choice of independent and dependent variables, it is best to use one of the symmetric algorithms. In order to simplify the discussion, I have chosen a single linear regression method to use. I have used the OLS bisector method because the deviations of OLS bisector slopes for samples of a population compared to the slopes for the entire population are smaller than for other methods.

Bibliography

[1] J. T. Bonnell and R. Klebesadel, A brief history of the discovery of cosmic gamma-ray bursts, In Kouveliotou et al. [110], pages 977–980.

[2] R. J. Nemiroff, A century of gamma-ray burst models, In Fishman et al. [111], pages 730–734.

[3] K. C. Hurley, A gamma-ray burst bibliography, 1973 – 1993, In Fishman et al. [111], pages 726–729.

[4] K. C. Hurley, A gamma-ray burst bibliography, 1973-1995, In Kouveliotou et al. [110], pages 985–989.

[5] K. C. Hurley, A gamma-ray burst bibliography, 1973-1997, In Meegan et al. [112], pages 87–91.

[6] M. S. Briggs et al., Testing the dipole and quadrupole moments of galactic models, In Kouveliotou et al. [110], pages 335–339.

[7] G. J. Fishman and C. A. Meegan, ARA&A **33**, 415 (1995).

[8] C. A. Meegan et al., The BATSE 3B catalog, In Kouveliotou et al. [110], pages 291–300.

[9] D. Q. Lamb, Implications of the observed angular distribution of gamma-ray bursts for galactic and cosmological models, In Kouveliotou et al. [110], pages 281–290.

[10] R. Narayan and T. Piran, MNRAS **265**, L65 (1993).

[11] R. Narayan and T. Piran, Do gamma-ray burst sources repeat?, In Fishman et al. [111], pages 132–135.

[12] J. J. and R. Kippen, Upper limits on gamma-ray burst repetition, In Meegan et al. [112], pages 226–230.

[13] J. Hakkila et al., GRB repetition limits from current BATSE observations, In Meegan et al. [112], pages 236–240.

[14] V. Connaughton et al., An unusual cluster of BATSE gamma-ray bursts, in *Eighteenth Texas Symposium on Relativistic Astrophysics and Cosmology*, edited by A. V. Olinto, J. A. Frieman, and D. N. Schramm, pages 514–516, Singapore, 1998, World Scientific.

[15] C. Graziani, D. Q. Lamb, and J. M. Quashock, Are the four gamma-ray bursts of 1996 october 27–29 due to repetition of a single source?, In Meegan et al. [112], pages 161–165.

[16] M. Schmidt, J. Higdon, and G. Heuter, ApJ **329**, L85 (1988).

[17] C. Kouveliotou et al., ApJ **413**, L101 (1993).

[18] C. Kouveliotou et al., Two classes of gamma-ray bursts, In Fishman et al. [111], pages 167–171.

[19] J. P. Norris, R. J. Nemiroff, and S. P. Davis, Exploration of bi-modality in gamma-ray burst duration and hardness distributions, In Fishman et al. [111], pages 172–176.

[20] V. Wang, Origins of the gamma-ray burst duration bimodality, In Kouveliotou et al. [110], pages 106–110.

[21] C. A. Meegan et al., ApJS **106**, 65 (1996).

[22] J. P. Norris et al., ApJ **459**, 393 (1996).

[23] K. C. Walker and B. E. Schaefer, The shortest time scale: A 200 microsecond rise time, In Meegan et al. [112], pages 266–270.

[24] J. D. Scargle, J. P. Norris, and J. T. Bonnell, Attributes of GRB pulses: Bayesian blocks analysis of TTE data; a microburst in GRB920229, In Meegan et al. [112], pages 181–185.

[25] D. B. Cline, C. Matthey, and S. Otwinowski, A detailed study of very short gamma-ray bursts, In Meegan et al. [112], pages 221–225.

[26] K. C. Walker, B. E. Schaefer, and E. Fenimore, ApJ , submitted (1998), (astro-ph/9810271).

[27] D. L. Band et al., ApJ **413**, 281 (1993).

[28] K. C. Hurley et al., Nature **372**, 652 (1994).

[29] S. Barthelmy et al., Progress with the real-time GRB coordinates distribution network (BACODINE), In Kouveliotou et al. [110], pages 580–584.

[30] S. Barthelmy et al., The GRB coordinate network (GCN): A status report, In Meegan et al. [112], pages 99–103.

[31] J. van Paradijs et al., Nature **386**, 686 (1997).

[32] S. Djorgovski et al., Nature **387**, 876 (1997).

[33] D. Frail, S. Kulkarni, L. Nicastro, M. Feroci, and G. Taylor, Nature **389**, 261 (1997).

[34] G. Taylor, D. Frail, A. Beasley, and S. Kulkarni, Nature **389**, 263 (1997).

[35] M. Metzger et al., Nature **387**, 878 (1997).

[36] S. Kulkarni et al., Nature **393**, 35 (1998).

[37] J. Halpern, J. Thorstensen, D. Helfand, and E. Costa, Nature **393**, 41 (1998).

[38] A. Ramaprakash et al., Nature **393**, 43 (1998).

[39] S. Kulkarni et al., Nature **395**, 663 (1998).

[40] T. Galama et al., Nature **395**, 670 (1998).

[41] K. Iwamoto et al., Nature **395**, 672 (1998).

[42] J. Bloom, S. Kulkarni, F. Harrison, T. Prince, and E. Phinney, ApJ **506**, L105 (1998).

[43] J. P. Norris, J. T. Bonnell, and K. Watanabe, ApJ **518**, 901 (1999).

[44] F. J. Vrba, Searches for gamma-ray burst counterparts: Current status and future prospects, In Kouveliotou et al. [110], pages 565–574.

[45] C. A. Meegan, *BATSE Flight Software User's Manual*, NASA/MSFC, Huntsville, AL, 1991.

[46] G. N. Pendleton, M. S. Briggs, and C. A. Meegan, The BATSE burst location algorithm, In Kouveliotou et al. [110], pages 877–885.

[47] G. J. Fishman et al., ApJS **92**, 229 (1994).

[48] C. A. Meegan et al., The second BATSE burst catalog, Technical report, Compton Observatory Science Support Center, 1994.

[49] C. A. Meegan et al., The 4B BATSE gamma-ray burst catalog, In Meegan et al. [112], pages 3–9.

[50] B. E. Schaefer and K. C. Walker, ApJ **511**, L89 (1999).

[51] J. D. Scargle, ApJ **263**, 835 (1982).

[52] N. Lomb, Ap&SS **39**, 447 (1976).

[53] W. H. Press, S. A. Teukolsky, W. T. Vetterling, and B. P. Flannery, *Numerical Recipes in C*, chapter 13, pages 575–584, Cambridge, Cambridge, second edition, 1992.

[54] J. P. Norris et al., ApJ **424**, 540 (1994).

[55] D. L. Donoho, De-noising via soft thresholding, Department of Statistics Technical Report 409, Stanford University, Stanford, CA, 1992.

[56] B. Stern, J. Poutanen, and R. Svensson, ApJ **489**, L41 (1997).

[57] A. Lee, E. D. Bloom, and J. D. Scargle, Time profiles and pulse structure of bright, long gamma-ray bursts using BATSE TTS data, In Kouveliotou et al. [110], pages 47–51.

[58] A. Lee, E. D. Bloom, and J. D. Scargle, Pulse decomposition analysis of BATSE GRB time profiles, In Meegan et al. [112], pages 261–265.

[59] A. Lee, E. D. Bloom, and V. Petrosian, ApJ , submitted (2000), (astro-ph/0002217, SLAC–PUB–8364).

[60] Research Systems, Inc., Boulder, CO, *IDL Reference Guide, Version 4*, 1995.

[61] G. N. Pendleton, ApJ **489**, 175 (1997).

[62] G. N. Pendleton et al., The HE and NHE burst populations in the cosmological scenario, In Meegan et al. [112], pages 25–29.

[63] W. H. Press, S. A. Teukolsky, W. T. Vetterling, and B. P. Flannery, *Numerical Recipes in C*, chapter 15, pages 699–706, Cambridge, Cambridge, second edition, 1992.

[64] W. H. Press, S. A. Teukolsky, W. T. Vetterling, and B. P. Flannery, *Numerical Recipes in C*, chapter 14, pages 620–628, Cambridge, Cambridge, second edition, 1992.

[65] J. P. Norris, Canonical timescales in GRBs – 1995, In Kouveliotou et al. [110], pages 13–22.

[66] T. T. Lee and V. Petrosian, ApJ **474**, L37 (1997).

[67] J. P. Norris et al., ApJ **301**, 213 (1986).

[68] G. Amelino-Camelia, J. Ellis, N. Mavromatos, D. Nanopoulos, and S. Sarkar, Nature **393**, 763 (1998).

[69] J. Higdon and R. Lingenfelter, BATSE detection biases against “slow rising” gamma-ray bursts, In Kouveliotou et al. [110], pages 402–406.

[70] E. Ramirez-Ruiz and E. Fenimore, A&AS **138**, 521 (1999).

[71] E. Ramirez-Ruiz and E. Fenimore, ApJ , submitted (1999), (astro-ph/9910273).

[72] N. J. Shaviv and A. Dar, MNRAS **277**, 287 (1995).

[73] B. Paczyński, Nature **355**, 521 (1992).

[74] T. Piran, ApJ **389**, L45 (1992).

[75] A. Goobar and S. Perlmutter, ApJ **450**, 14 (1995).

[76] C. W. Misner, K. S. Thorne, and J. A. Wheeler, *Gravitation*, chapter 29, pages 782–794, Freeman, New York, 1970.

[77] S. Weinberg, *Gravitation and Cosmology: Principles and Applications of the General Theory of Relativity*, chapter 15, pages 481–491, Wiley, New York, 1972.

[78] E. W. Kolb and M. S. Turner, *The Early Universe*, chapter 2, pages 39–45, Number 69 in Frontiers in Physics, Addison-Wesley, Redwood City, CA, 1990.

[79] S. Perlmutter et al., ApJ **517**, 565 (1999).

[80] A. G. Riess et al., AJ **116**, 1009 (1998).

[81] S. P. Davis et al., Pulse width distributions and total counts as indicators of cosmological time dilation in gamma-ray bursts, In Fishman et al. [111], pages 182–186.

[82] S. P. Davis, *Measurements of Time Dilation in Gamma-Ray Bursts by Analysis of Temporal Structure*, PhD thesis, The Catholic University of America, Washington, D.C., 1995.

[83] J. P. Norris, J. D. Scargle, J. T. Bonnell, and R. J. Nemiroff, GRB time profiles as cosmic probes: Is time dilation extrinsic or intrinsic?, In Meegan et al. [112], pages 171–175.

[84] V. Petrosian, N. M. Lloyd, and A. Lee, Cosmological signatures in temporal and spectral characteristics of gamma-ray bursts, in *Gamma Ray Bursts: The First Three Minutes*, edited by J. Poutanen and R. Svensson, volume 190, San Francisco, 1999, ASP.

[85] J. Neubauer and B. E. Schaefer, Peak-to-peak dilation of gamma-ray bursts, In Kouveliotou et al. [110], pages 67–71.

[86] J. P. Norris, J. T. Bonnell, R. J. Nemiroff, and J. D. Scargle, Test for time dilation of intervals between pulse structures in gamma-ray bursts, In Kouveliotou et al. [110], pages 77–81.

[87] M. Deng and B. E. Schaefer, Time dilation in the peak-to-peak time scale of GRBs, In Meegan et al. [112], pages 251–255.

[88] M. Deng and B. E. Schaefer, ApJ **502**, L109 (1998).

[89] V. Petrosian and T. T. Lee, ApJ **467**, L29 (1996).

[90] N. M. Lloyd and V. Petrosian, ApJ **511**, 550 (1999).

[91] V. Petrosian and T. T. Lee, Flux-duration correlations and cosmological time dilation, In Kouveliotou et al. [110], pages 82–86.

[92] B. Stern, R. Svensson, and J. Poutanen, Average properties of the time behaviour of gamma-ray bursts, in *Proceedings of the 2nd INTEGRAL Workshop; St. Malo, France, September 1996*, 1997.

[93] M. L. Litvak et al., The time stretching of the average rise fronts and back slopes of different intensity groups of BATSE GRBs, In Meegan et al. [112], pages 176–180.

[94] B. Stern, J. Poutanen, and R. Svensson, ApJ **510**, 312 (1999).

[95] A. Lee, E. D. Bloom, and V. Petrosian, ApJ , submitted (2000), (astro-ph/0002218, SLAC–PUB–8365).

[96] E. D. Kolaczyk, ApJ **483**, 340 (1997).

[97] J. D. Scargle, ApJ **504**, 405 (1998).

[98] NASA / Science Office of Standards and Technology, GSFC, Greenbelt, MD, *A User's Guide for the Flexible Image Transport System (FITS), Version 3.1*, 1994.

[99] BATSE second burst catalog, CD-ROM, 1995.

[100] BATSE fourth burst catalog, CD-ROM, 1997.

[101] H. Abarbanel et al., Wavelets, Technical Report JSR–90–150, JASON, McLean, VA, 1991.

[102] W. H. Press, S. A. Teukolsky, W. T. Vetterling, and B. P. Flannery, *Numerical Recipes in C*, chapter 13, pages 591–606, Cambridge, Cambridge, second edition, 1992.

[103] B. Vidaković and P. Müller, Wavelets for kids: A tutorial introduction, 1994.

[104] Y. Meyer, *Wavelets: Algorithms & Applications*, SIAM, Philadelphia, 1993.

[105] W. Cash, ApJ **228**, 939 (1979).

[106] W. H. Press, S. A. Teukolsky, W. T. Vetterling, and B. P. Flannery, *Numerical Recipes in C*, chapter 15, pages 681–688, Cambridge, Cambridge, second edition, 1992.

[107] W. H. Press, S. A. Teukolsky, W. T. Vetterling, and B. P. Flannery, *Numerical Recipes in C*, chapter 14, pages 636–645, Cambridge, Cambridge, second edition, 1992.

[108] B. Efron and V. Petrosian, ApJ **399**, 345 (1992).

[109] T. Isobe, E. D. Feigelson, M. G. Akritas, and G. J. Babu, ApJ **364**, 104 (1990).

[110] C. Kouveliotou, M. F. Briggs, and G. J. Fishman, editors, *Gamma-Ray Bursts: 3rd Huntsville Symposium*, number 384 in AIP Conf. Proc., Woodbury, NY, 1996, AIP.

[111] G. J. Fishman, J. J. Brainerd, and K. C. Hurley, editors, *Gamma-Ray Bursts - Second Workshop*, number 307 in AIP Conf. Proc., New York, 1994, AIP.

[112] C. A. Meegan, R. D. Preece, and T. M. Koshut, editors, *Gamma-Ray Bursts: 4th Huntsville Symposium*, number 428 in AIP Conf. Proc., Woodbury, NY, 1998, AIP.